

Search for compressed mass Higgsino production with soft lepton tracks with the CMS experiment in proton-proton collision data at $\sqrt{s} = 13$ TeV

von der Fakultät für Physik der Universität Hamburg zur
Erlangung des akademischen Grades eines Doktors der
Naturwissenschaften genehmigte Dissertation

Vorgelegt von

YUVAL NISSAN

im August 2022



Abstract This is the abstract

Contents

1	Introduction	1
2	Quantum Field Theory and The Standard Model	3
2.1	Quantum Field Theory	3
2.2	The Standard Model of particle physics	3
2.2.1	The particle content	3
3	Supersymmetry	5
3.0.1	Phenomenology of Higgsino production	5
4	Multivariate Statistics	7
4.1	Decision Trees	7
5	Experimental setup	9
5.1	The Large Hadron Collider	9
5.2	The Compact Muon Solenoid experiment	9
5.3	Simulation of events	9
6	Object reconstruction and identification of particles and jets	11
6.1	Track reconstruction	11
6.2	Electrons	11
6.3	Muons	11
6.4	Jets	11
7	Search for compressed Higgsinos with soft lepton tracks	13
7.1	Motivation	13
7.2	Signal models	13
7.3	Previous searches	13
7.4	Search strategy	14
7.4.1	Exclusive track category	14
7.4.2	Dimuon category	14
7.5	Signal signature and base selection	15
7.5.1	Missing Transverse Energy	15
7.5.2	Jets and hardronic activity	15
7.5.3	Base selection	16
7.5.4	Dilepton kinematics	19
7.5.4.1	Lepton η and transverse momentum p_T	19
7.5.4.2	Invariant mass $m_{\ell\ell}$	22
7.5.4.3	Lepton separation ΔR	23
7.5.5	Main drivers of sensitivity	26
7.6	Simulated samples	27

7.6.1	Standard Model simulated samples	27
7.6.2	Signal simulated samples	27
7.7	Object definition and selection	28
7.7.1	Electrons	28
7.7.2	Muons	33
7.7.3	Scale factors	37
7.7.4	Missing transverse energy	42
7.7.5	Jets	42
7.7.6	Tracks and multivariate selection	43
7.7.7	Isolation	47
7.8	Trigger	51
7.9	Event selection	52
7.9.1	Baseline selection	52
7.9.2	Category selection	53
7.9.2.1	Dilepton selection	53
7.9.2.2	Exclusive track selection	53
7.9.3	Boosted decision trees	54
7.9.3.1	Dimuon category	54
7.9.3.2	Exclusive track category	57
7.10	Characterization and estimation of the Standard Model backgrounds	60
7.10.1	Characterization of the Standard Model backgrounds	60
7.10.1.1	Dimuon category	62
7.10.1.2	Exclusive track category	64
7.10.2	Estimation of the Standard Model backgrounds	66
7.10.2.1	Non-isolated jetty background estimation	67
7.10.2.2	Ditau Drell-Yann background estimation	69
7.10.2.3	Exclusive track background estimation	72
7.11	Data control region plots	74
7.12	Signal regions definition and optimization	77
7.13	Systematic uncertainties	79
7.13.1	Data driven transfer factors	79
7.13.2	Data driven shape uncertainties	79
7.13.3	Simulated background uncertainties	80
7.14	Data quality aspects and background validation	82
7.14.1	L1 prefire issue in 2016 and 2017 data	82
7.14.2	EE noise in 2017 data	82
7.14.3	HEM failure in 2018 data	82
7.14.4	Same sign validation plots	82
7.15	Results and interpretation	84
8	Summary	85
9	Latex stuff	87
9.1	Some examples	87
9.1.1	Multiline comment	87
9.1.2	Fixme note	87
9.1.3	Tables	87
9.1.4	Cross References	87
9.1.5	Particles	87
9.1.6	Citing	87

CONTENTS

9.1.7	Glossary	87
9.1.8	Acronyms	88
9.1.9	fractions	88
	Glossary	91
	Acronyms	93

CONTENTS

Chapter 1

Introduction

This is a line in introduction. This is the introduction to the thesis.

Chapter 2

Quantum Field Theory and The Standard Model

2.1 Quantum Field Theory

2.2 The Standard Model of particle physics

2.2.1 The particle content

Chapter 3

Supersymmetry

3.0.1 Phenomenology of Higgsino production

Chapter 4

Multivariate Statistics

4.1 Decision Trees

Chapter 5

Experimental setup

One of the most useful methods to study the subatomic world of particle physics is by using particle accelerators. In such machines, particles are accelerated to very high speeds and energies, and smashed into each other. The resulted particles are then studied by measuring them in a detector. At the time of writing this thesis, the largest currently active accelerator is the Large Hadron Collider (LHC) near Geneva, Switzerland, operated by the European Organization for Nuclear Research (CERN). For the analysis presented in this thesis, data from the Compact Muon Solenoid (CMS) experiment has been analyzed. In this chapter, the LHC is described in 5.1, while the CMS experiment is described in 5.2.

5.1 The Large Hadron Collider

5.2 The Compact Muon Solenoid experiment

5.3 Simulation of events

Chapter 6

Object reconstruction and identification of particles and jets

6.1 Track reconstruction

This is the track reconstruction page.

6.2 Electrons

6.3 Muons

6.4 Jets

Chapter 7

Search for compressed Higgsinos with soft lepton tracks

7.1 Motivation

7.2 Signal models

The signal models considered in this analysis are based on **Fixme Note:** fill in signal model stuff.

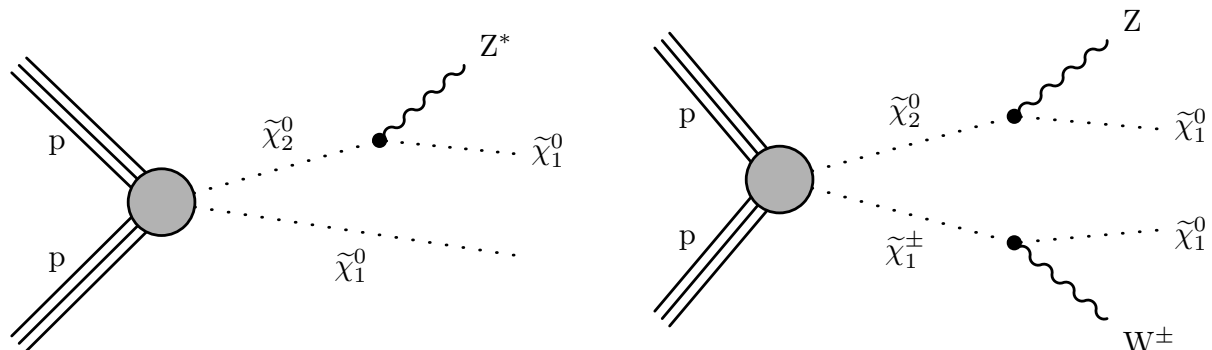


Figure 7.1: Production and decay of electroweakinos in the higgsino simplified model through $\tilde{\chi}_2^0 \tilde{\chi}_1^0$ (left) and $\tilde{\chi}_2^0 \tilde{\chi}_1^\pm$ (right).

Fixme Note: make sure we define the different deltaM somewhere

7.3 Previous searches

7.4 Search strategy

7.4.1 Exclusive track category

7.4.2 Dimuon category

7.5 Signal signature and base selection

To develop an effective analysis strategy, one must study and exploit the signal kinematics. The production of electroweakinos has unique characteristics that can be leveraged to differentiate the signal from the Standard Model (SM) background. It is crucial to examine these signal distributions to define a preselection or base cut that retains the maximum signal while rejecting as much background as possible. All the following distributions were generated by weighting the simulation to the Run II luminosity of $\mathcal{L} = 135 \text{ fb}^{-1}$ and requiring at least one jet in the event with $p_T \geq 30 \text{ GeV}$ and $|\eta| < 2.4$. Any additional selection criteria will be listed in each section, if applicable.

7.5.1 Missing Transverse Energy

A common property shared by essentially all searches for Dark Matter (DM) is the presence of a DM candidate in the production. The identity and properties of the particle (or particles in the case of multiple DM candidates) vary, but they do have much in common. In this Supersymmetry (SUSY) search, the neutralino is the DM candidate, which is a type of Weakly Interacting Massive Particle (WIMP). A WIMP is a new elementary particle that interacts via gravity and potentially other forces, not part of the SM itself, and is as weak as or weaker than the weak nuclear force, but also non-vanishing in strength. This essentially means that such a candidate is neutral and does not interact via the electromagnetic force. A neutral particle that does not interact electromagnetically or via the strong force (i.e., is colorless) will not be detected and will leave traces in the form of a transverse momentum imbalance, which is referred to as E_T^{miss} (Missing Transverse Energy or Missing Transverse Momentum). The signal contains two DM candidates in the production, which are the Lightest SUSY Particles (LSPs), the neutralinos $\tilde{\chi}_1^0$. Therefore, a considerable magnitude of E_T^{miss} is expected in the signal. As described in Section 7.7.4, H_T^{miss} is of greater interest, which is highly correlated with E_T^{miss} , due to the definition of lepton isolation and its use in the background estimation methods. Nonetheless, both E_T^{miss} and H_T^{miss} observables will be examined in Figure 7.2.

As expected, E_T^{miss} and H_T^{miss} are hardly affected by the different choices for Δm , while the higgsino parameter μ affects the distributions mainly through its lower production cross section for higher higgsino parameter μ . The region of interest for triggering purposes is located at $H_T^{\text{miss}} \geq 220$, as discussed in Section 7.8. Although this is a harsh and inefficient cut, it is necessary to consider the SM background in both regions of $H_T^{\text{miss}} < 220$ and $H_T^{\text{miss}} \geq 220$ to conclude that most of the sensitivity comes from the $H_T^{\text{miss}} \geq 220$ region, as the production of real H_T^{miss} (or E_T^{miss}) results from the production of neutrinos in the event, which are much less common than Quantum Chromodynamics (QCD) events that dominate the $H_T^{\text{miss}} < 220$ region. Therefore, a cut at $H_T^{\text{miss}} \geq 220$ might be inefficient, but it results in high sensitivity.

7.5.2 Jets and hardronic activity

To maximize the boost of the neutralinos $\tilde{\chi}_1^0$ that contribute to the H_T^{miss} and drive sensitivity in the high H_T^{miss} region, it is desirable to maximize their transverse momentum p_T . A widely used method is to include an Initial State Radiation (ISR) jet in the event. An ISR jet is created when one of the incoming protons emits radiation (such as a photon or a gluon) before the interaction. If a jet with sufficiently high p_T is emitted, the remainder of the interaction is recoiled against this jet and imparts momentum to it in the opposite direction. As a result, the boosted neutralinos $\tilde{\chi}_1^0$ will have higher H_T^{miss} . As described in Section 7.7.5, the jets are required to have $p_T \geq 30 \text{ GeV}$ and be located within the tracker acceptance ($|\eta| < 2.4$). At

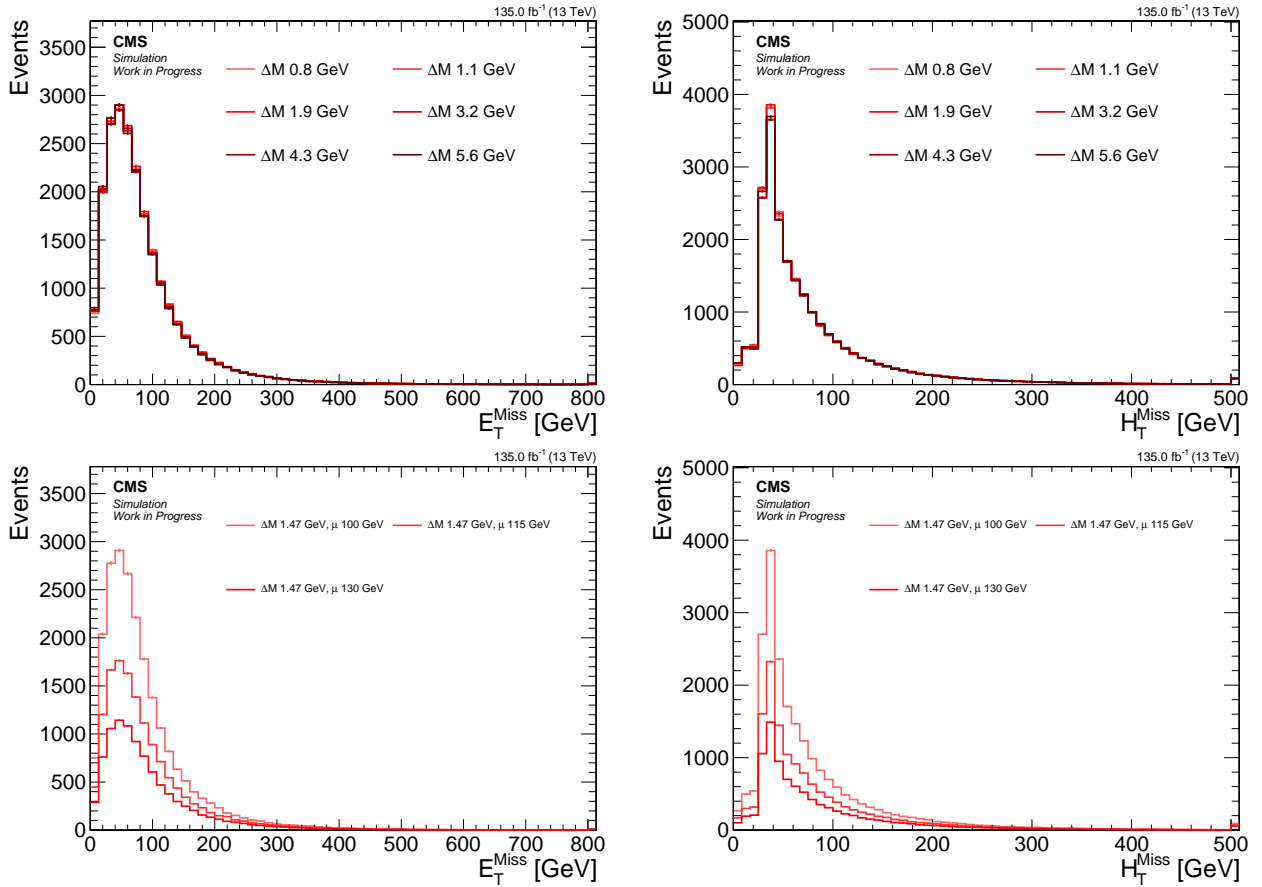


Figure 7.2: Signal distributions for E_T^{miss} (left) and H_T^{miss} (right) comparing various Δm with a fixed higgsino parameter $\mu = 100 \text{ GeV}$ (upper), and comparing various higgsino parameters μ with fixed $\Delta m = 1.47 \text{ GeV}$ (lower).

least one such jet is required in each event. The distributions of the number of jets and the leading jet p_T are displayed in Figure 7.3.

The signal signature does not include a b-jet, that is, a jet resulting from a bottom quark hadronization (either resulting from a top quark or not). This knowledge is exploited by vetoing b-tagged jets in the event. As described in Section 7.7.5, the DEEPCSV bottom flavor tagging discriminant with a medium working point is used. The majority of the signal can be seen in the 0 bin, and thus any b-tagged jet will be vetoed, retaining most of the signal but rejecting a lot of SM background, such as that arising from $t\bar{t}$ events.

As an ISR jet is required in the event, it is expected that the E_T^{miss} and the H_T^{miss} will be directed in the opposite direction of the jet, or at an angle close to π . This feature will not be observed in events with multiple jets in the SM background, such as those arising from QCD. To reduce the QCD background, a requirement of $\min \Delta\phi(H_T^{\text{miss}}, \text{jets}) > 0.4$ is imposed.

7.5.3 Base selection

The section is recapped by summarizing the base selection of the analysis. The base selection, also known interchangeably as the preselection, is applied to all analysis categories. It is listed in Table 7.5.3.

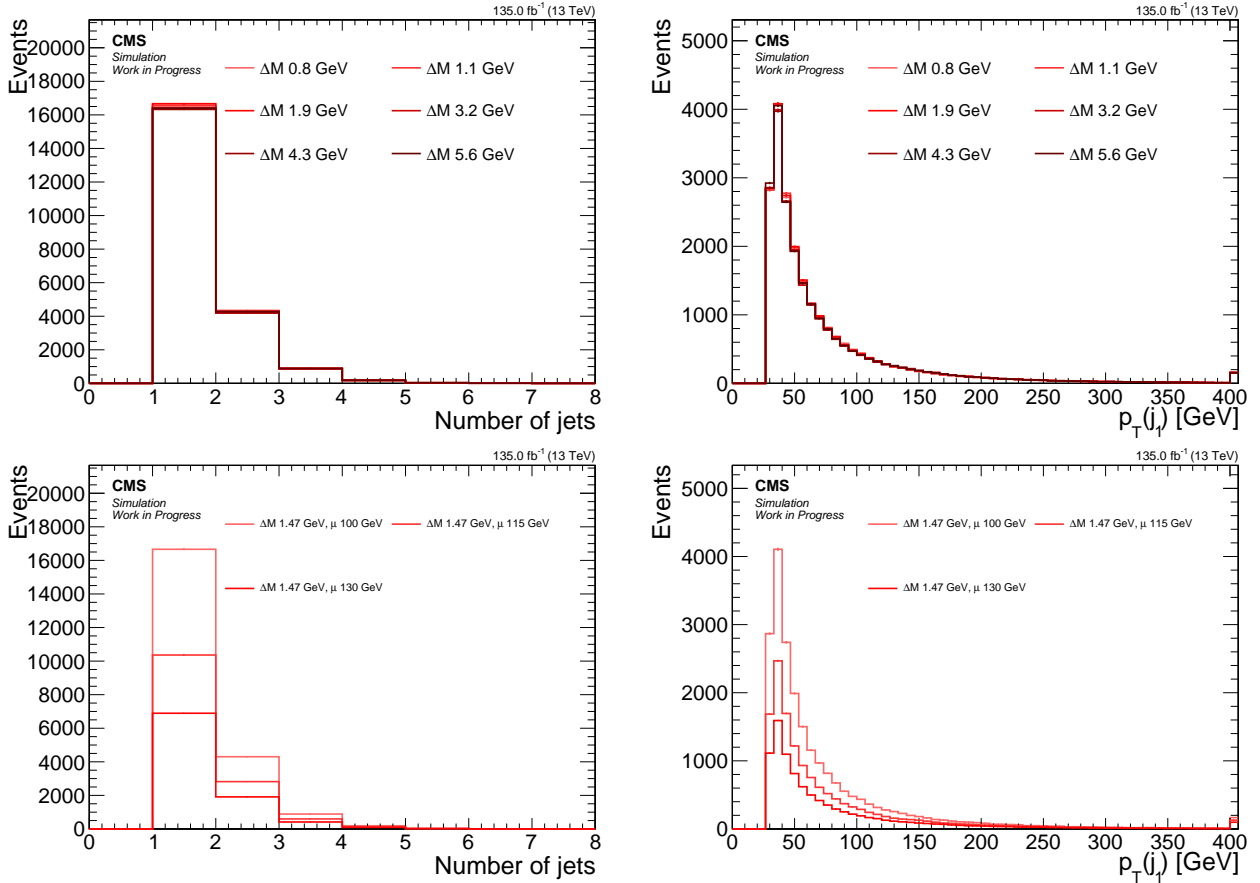


Figure 7.3: Signal distributions for *number of jets* (left) and *leading jet p_T* (right) comparing various Δm with a fixed higgsino parameter $\mu = 100$ GeV (upper), and comparing various higgsino parameters μ with fixed $\Delta m = 1.47$ GeV (lower).

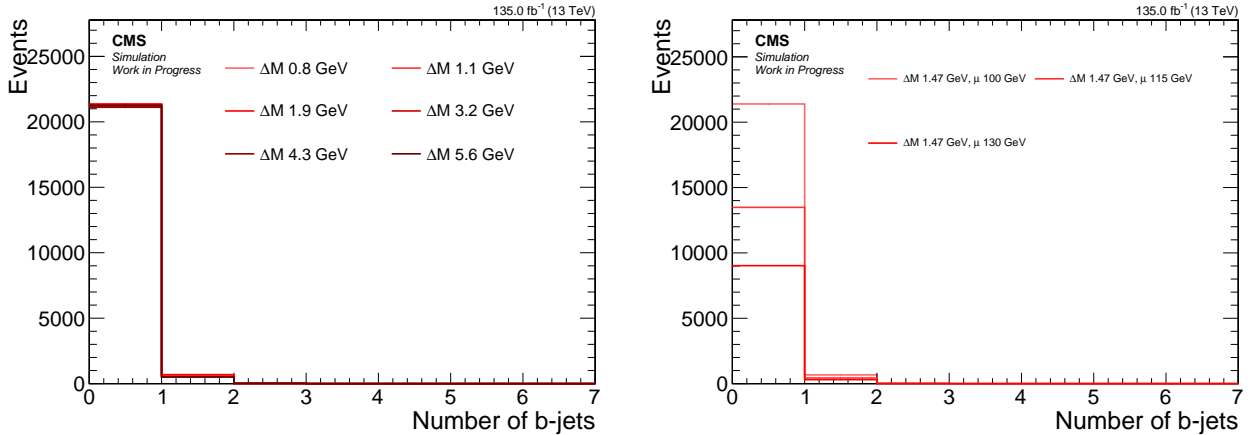


Figure 7.4: Signal distributions for *number of b-tagged jets* comparing various Δm with a fixed higgsino parameter $\mu = 100$ GeV (left), and comparing various higgsino parameters μ with fixed $\Delta m = 1.47$ GeV (right).

Table 7.1: Base selection applied to all analysis categories

Variable	Value
H_T^{miss} [GeV]	≥ 220
N_{jets} ($p_T \geq 30$ GeV and $ \eta < 2.4$)	≥ 1
$N_{\text{b-jets}}$ ($p_T \geq 30$ GeV and $ \eta < 2.4$)	0
$\min \Delta\phi(H_T^{\text{miss}}, \text{jets})$	> 0.4

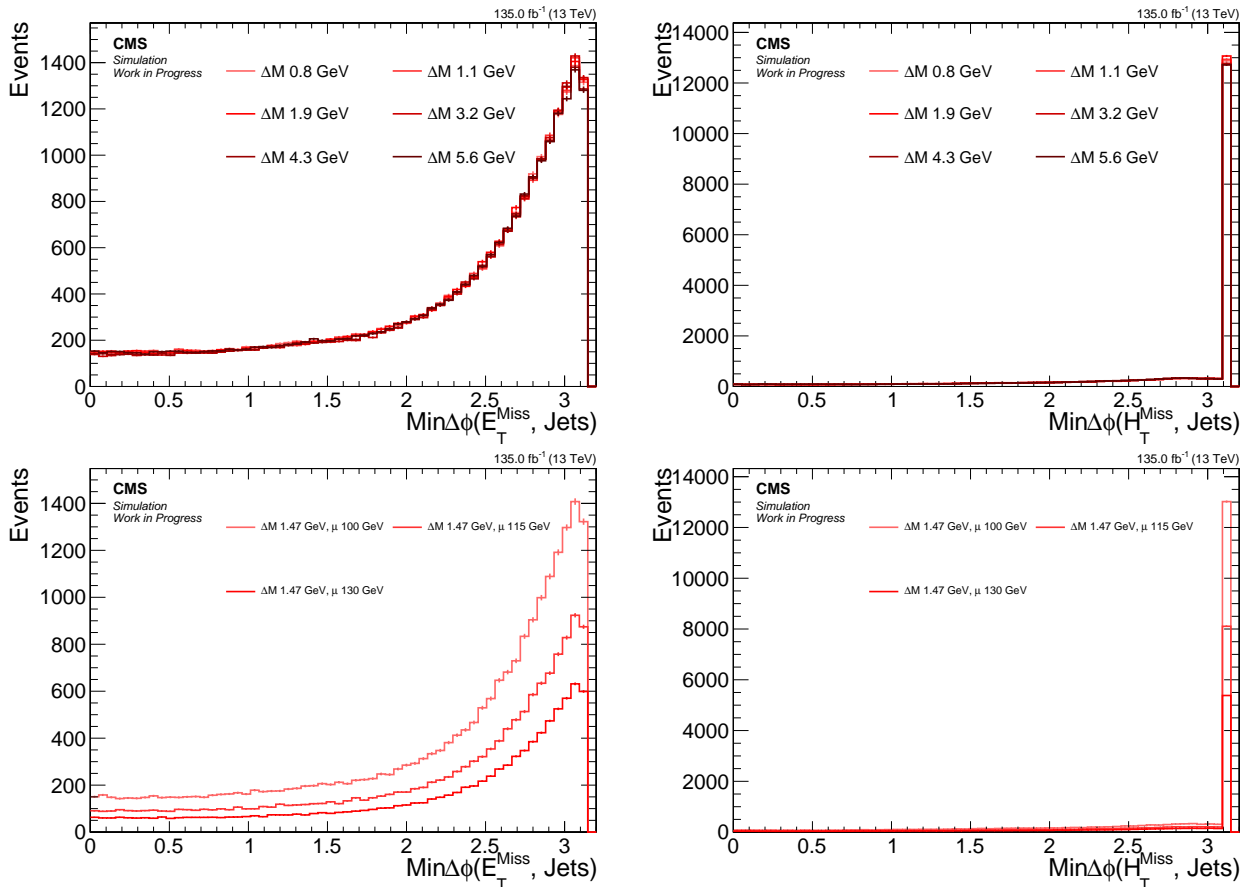


Figure 7.5: Signal distributions for $\text{min } \Delta\phi \left(E_T^{\text{miss}}, \text{jets} \right)$ (left) and $\text{min } \Delta\phi \left(H_T^{\text{miss}}, \text{jets} \right)$ (right) comparing various Δm with a fixed higgsino parameter $\mu = 100 \text{ GeV}$ (upper), and comparing various higgsino parameters μ with fixed $\Delta m = 1.47 \text{ GeV}$.

7.5.4 Dilepton kinematics

Kinematic distributions have been examined so far, with the leptons in the event ignored. However, the dilepton system contains the most distinctive features of the signal. To fully understand the unique phase space of the dilepton system, generator level distributions are examined first, followed by an exploration of the effects of reconstruction on those observables. Since the dimuon category is the most sensitive due to its lower threshold on the leptons' transverse momentum, events with two electrons are excluded from the following sections, focusing on the muons. The kinematics change dramatically as a function of Δm . In contrast, the higgsino parameter μ effects almost only the overall normalization due to the different production cross section. Therefore, the higgsino parameter is set to $\mu = 100$ GeV in the following sections, with the Δm varied.

7.5.4.1 Lepton η and transverse momentum p_T

The signal acceptance and sensitivity are significantly impacted by the accessible thresholds of the transverse momentum p_T distribution of the muons. The muon reconstruction process and details are discussed in Section 6.3. The selection applied to the muons in this analysis is described in Section 7.7.2 and referred to as *analysis selection*. This section aims to examine the importance of the p_T on the signal and its dilepton kinematic distributions.

The generator level distribution of p_T , or the so-called *truth* distributions, which do not exhibit any detector or reconstruction features, are examined first. The reconstructed distribution is then compared with the generator level distribution in Figure 7.6.

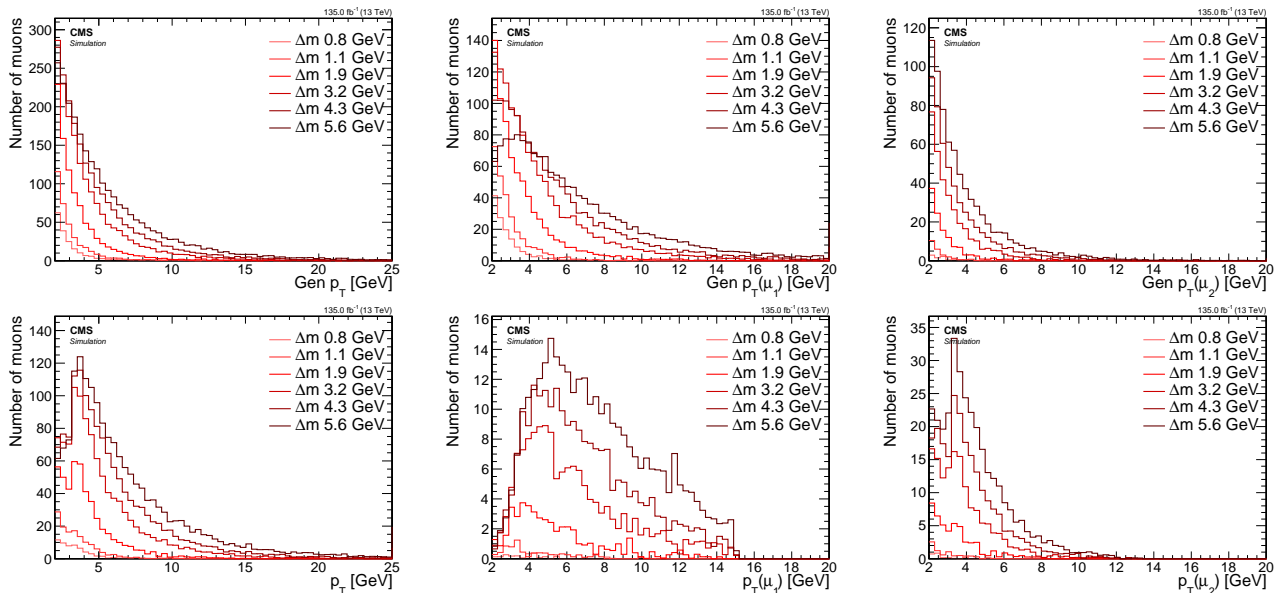


Figure 7.6: Signal p_T distributions for inclusive (left), leading muon μ_1 (middle), subleading muon μ_2 (right) at generator level (top) and reconstruction level passing analysis selection (bottom).

When comparing the generator level to the reconstruction level of the inclusive p_T distribution, it becomes apparent that a reshaping occurs around 3 GeV. A significant proportion of the generated muons with $p_T < 3$ GeV is lost in the reconstruction process. The subleading muon p_T distribution at the reconstruction level has a camel shape, whereby the efficiency drops below a p_T of 3 GeV and is only partially regained at $p_T > 3$ GeV. This effect is due to the detector and is more clearly visible when splitting the p_T distribution into a barrel ($|\eta| < 1.2$) and encaps ($|\eta| \geq 1.2$) portions, as shown in Figure 7.7.

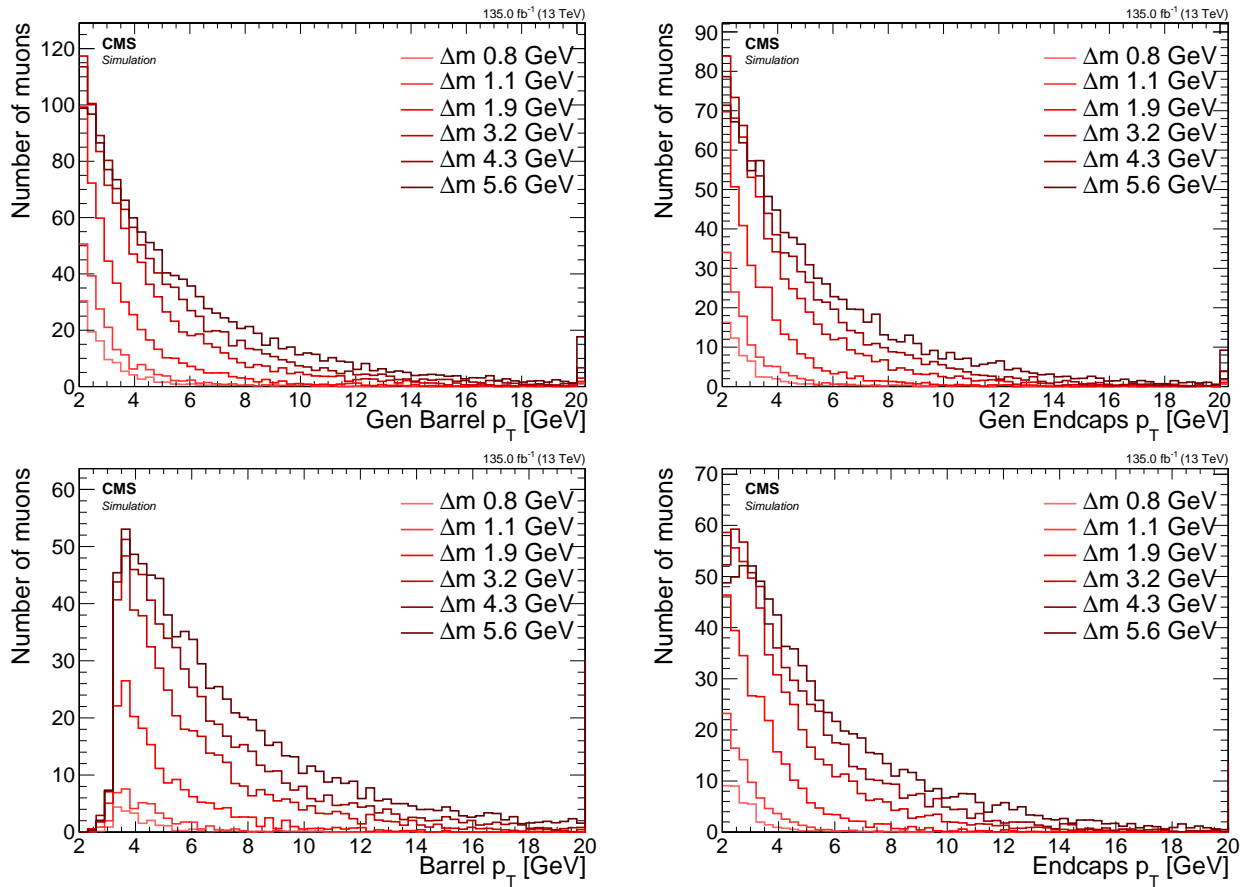


Figure 7.7: Signal inclusive p_T distributions for barrel $|\eta| < 1.2$ (left) and endcaps $|\eta| \geq 1.2$ (right) at generator level (top) and reconstruction level passing analysis selection (bottom).

The picture becomes much clearer when the reconstruction efficiency as a function of p_T is examined. When comparing the generator level distribution of the barrel muons on the top left with its reconstructed counterpart on the bottom left, it can be seen that the barrel is almost completely unable to reconstruct muons with $p_T < 3 \text{ GeV}$, while the endcaps, shown on the left, are able to do so. As demonstrated in the upcoming sections on $m_{\ell\ell}$ and ΔR (see 7.5.4.2 and 7.5.4.3), the relationship between these distributions has consequences for the reshaping of kinematic distributions, as well as signal acceptance in general. Access to low Δm signal points is crucially dependent on the low p_T region of $2 \leq p_T \leq 3.5 \text{ GeV}$, which is mainly achieved with the help of the muon chamber endcaps, as can be seen here.

Since the barrel and endcaps are separated by different regions of η , $|\eta| < 1.2$ for barrel and $|\eta| \geq 1.2$ for endcaps, it is worthwhile taking a look at the η distributions of the muons as well. Those can be seen at Figure 7.8.

The muons analysis selection only selects muons within the tracker range of $|\eta| < 2.4$. This is why the muons with $|\eta| > 2.4$ are not present in the reconstruction plots on the bottom. It can be seen that the main effect of going from the inclusive $|\eta|$ at the generator level to the reconstructed counterpart is the flattening of the distribution due to the loss of muons with $|\eta| < 1.2$ in the barrel for muons with $p_T < 3 \text{ GeV}$.

With the understanding of the reconstruction effects on the p_T and η distributions of the muons, an examination of other kinematic variables of the dilepton system is now possible.

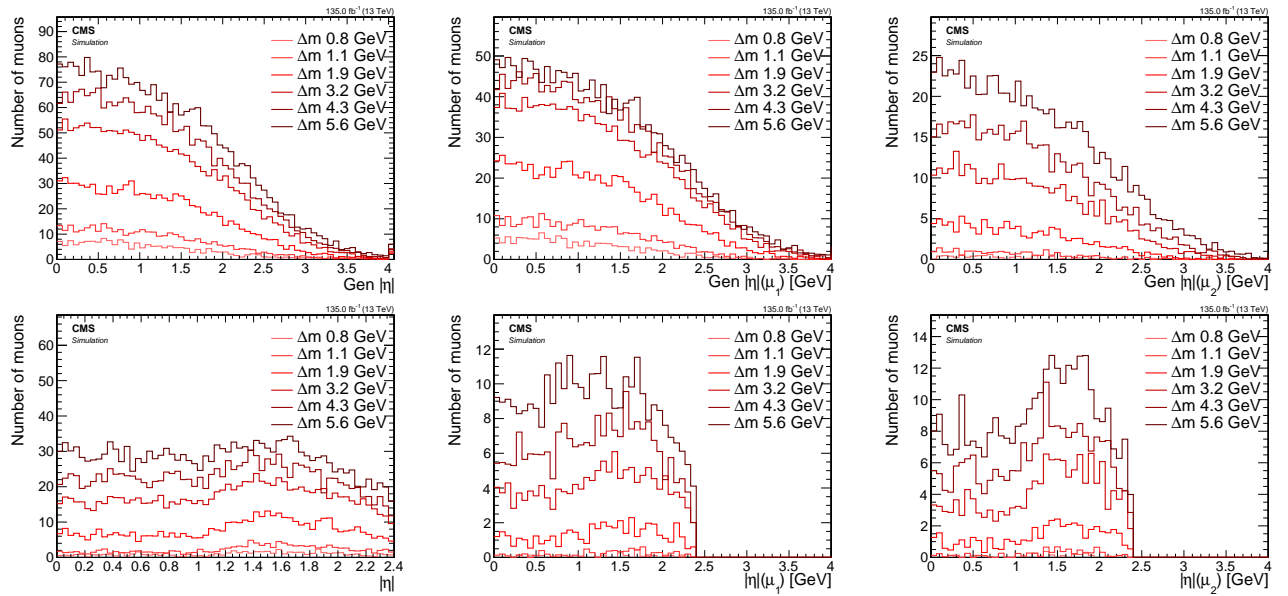


Figure 7.8: Signal $|\eta|$ distributions for inclusive (left), leading muon μ_1 (middle), subleading muon μ_2 (right) at generator level (top) and reconstruction level passing analysis selection (bottom).

7.5.4.2 Invariant mass $m_{\ell\ell}$

The invariant mass of the two leptons resulting from the decay of the $\tilde{\chi}_2^0$ has a unique shape due to the limited allowed phase space of the leptons as part of the 3-body decay. As the $\tilde{\chi}_2^0$ decays into $\tilde{\chi}_1^0$ and $\ell^+\ell^-$ through a Z^* , the allowed phase space of the dilepton pair is restricted to the mass difference between $\tilde{\chi}_2^0$ and $\tilde{\chi}_1^0$, that is, Δm . Therefore, the $m_{\ell\ell}$ distribution is expected to have an edge at Δm . Distributions of the generator level invariant mass can be seen in Figure 7.9.

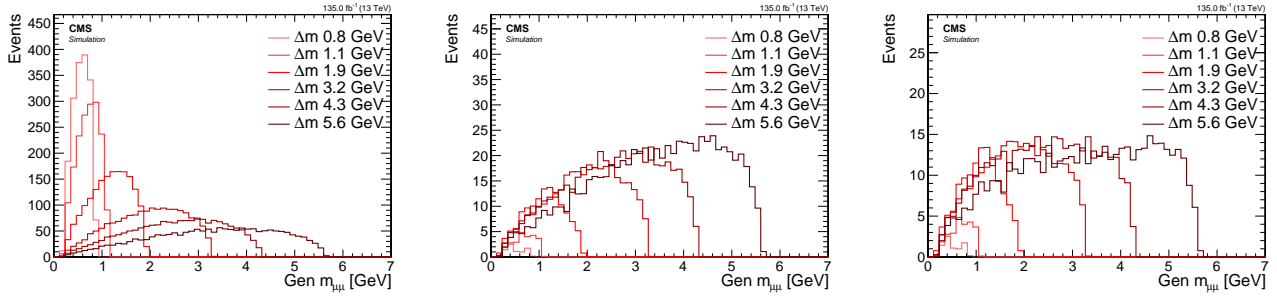


Figure 7.9: Signal generator level $m_{\ell\ell}$ distributions with no cuts (left), with $p_T(\mu_i) > 2 \text{ GeV}$, $i = 1, 2$ (middle) and with SOS orthogonality condition $p_T(\mu_i) > 2 \text{ GeV}$, $p_T(\mu_2) \leq 3.5 \text{ GeV}$ or $\Delta R \leq 0.3$ (right).

The inclusive distribution of the invariant mass of the muons $m_{\mu\mu}$ is shown on the left. The edge of the $m_{\mu\mu}$ distribution for each signal point is located right at the corresponding Δm . However, when the muons p_T are cut and required to be $p_T \geq 2 \text{ GeV}$, the shape of the distribution shifts, and the efficiency in the lower Δm range drops significantly, as depicted in the middle plot. Lastly, the effect of orthogonalizing phase space to the SOS analysis is demonstrated in the rightmost plot. The effect is strongest in high Δm and quite subtle in low Δm .

To comprehend the reshaping that occurs to the $m_{\mu\mu}$ shape, the relationship between the p_T of the muons (leading muon denoted μ_1 while subleading muon is denoted μ_2) and the invariant mass is examined. One signal with low Δm of 1.13 GeV and one with high Δm of 5.63 GeV are selected for this analysis. The distributions are shown in Figure 7.10.

Earlier, it was established that the invariant mass distribution has an edge at Δm , and the value of Δm can be read from these plots. Another interesting feature to notice in these plots is that there is also a lower edge in the Δm distribution at around $\sim 0.2 \text{ GeV}$, which is due to each muon having a mass of around $\sim 0.1 \text{ GeV}$. It is now clear that by cutting on both muons at $p_T \geq 2 \text{ GeV}$, a significant portion of the signal is lost. This effect becomes particularly substantial for the low $\Delta m = 1.13 \text{ GeV}$ (top row). The magnitude of this effect is quantified by a cutflow table, where each row represents a cut, and its efficiency is calculated by dividing the number of events passing the cut by the number of events in the previous line. The first line is the baseline of all dimuon events with at least one jet with $p_T \geq 30 \text{ GeV}$ and $|\eta| < 2.4$, and it has an efficiency of 1 by definition. The event number is weighted to Run II luminosity of $\mathcal{L} = 135 \text{ fb}^{-1}$. The table is shown in 7.5.4.2.

It is observed that for the low Δm of 1.13 GeV, the acceptance of the signal is significantly reduced by the $p_T \geq 2 \text{ GeV}$ cut, with only 1.5% of the signal remaining. In contrast, the orthogonality condition of requiring $p_T(\mu_2) \leq 3.5 \text{ GeV}$ or $\Delta R(\ell\ell) \leq 0.3$ does not affect it any further. The situation is different for the high Δm of 5.63 GeV, where the p_T cut is cutting away more than half of the signal and the SOS orthogonality is cutting an additional two thirds.

It has been established that the p_T distribution directly affects the $m_{\ell\ell}$ distribution due to the relationship between the two variables. Thus, it is necessary to investigate how the

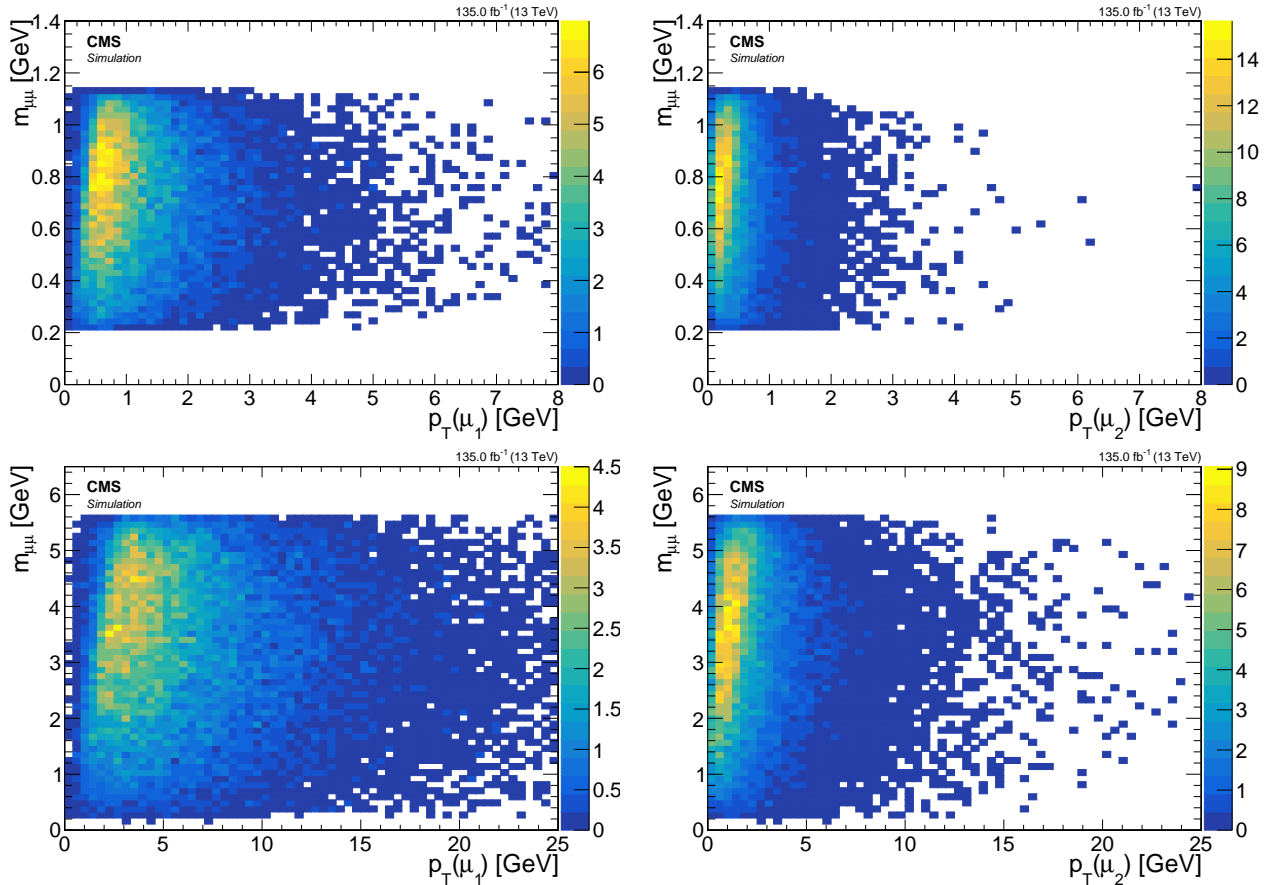


Figure 7.10: Signal $m_{\mu\mu}$ vs. p_T for leading lepton μ_1 (left) and subleading lepton μ_2 (right) for $\Delta m = 1.13 \text{ GeV}$ (top) and $\Delta m = 5.63 \text{ GeV}$ (bottom).

Table 7.2: Generator level efficiency on muons selections

Cut	Number of events		Efficiency	
	$\Delta m = 1.13 \text{ GeV}$	$\Delta m = 5.63 \text{ GeV}$	$\Delta m = 1.13 \text{ GeV}$	$\Delta m = 5.63 \text{ GeV}$
Baseline	1710.7	1743.9	1	1
$p_T \geq 2 \text{ GeV}$	24.7	724.9	0.015	0.41
SOS orthogonality	24.7	490.6	1	0.68

reconstruction discussed in Section 7.5.4.1 might impact the $m_{\mu\mu}$ distribution. The distributions of the reconstructed $m_{\mu\mu}$ can be seen in Figure 7.11.

It is interesting to compare these distributions to the two right ones in the generator level version at Figure 7.9. It can be seen that not only are fewer events surviving the reconstruction, but also some Δm model points are peaking between 1 GeV to 2 GeV with the SOS orthogonality condition applied.

7.5.4.3 Lepton separation ΔR

The lepton separation is defined by the equation $\Delta R = \sqrt{(\Delta\eta)^2 + (\Delta\phi)^2}$, where η represents the pseudorapidity and ϕ is the azimuthal angle measured in radians. The value of ΔR is significant in this analysis because the produced leptons tend to be located in proximity to each other and therefore are not easily isolated according to standard definitions. Special attention is given to ensuring that the collimated nature of the leptons can be used to differentiate the isolated leptons in the signal from the non-isolated leptons in the SM background. It is worth noting that, for the purposes of orthogonality, we attempt to revert the requirement of $\Delta R(\ell\ell) > 0.3$

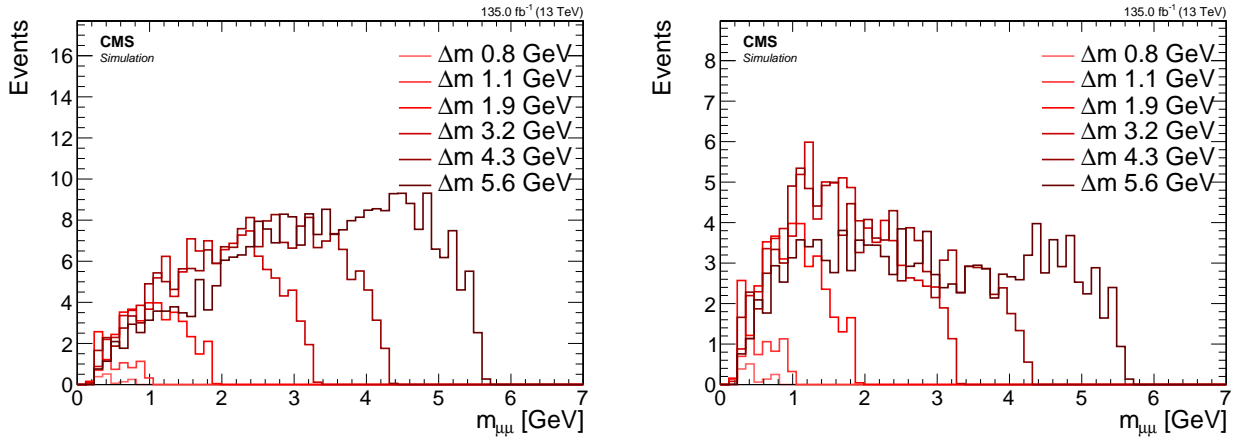


Figure 7.11: Signal reconstructed $m_{\mu\mu}$ with basic analysis selection (left) and additional SOS orthogonality condition (right).

utilized in previous SOS analyses [1].

Similar to the invariant mass discussed in Section 7.5.4.2, we examine the distributions of ΔR for various Δm options with different cuts applied to observe their effect.

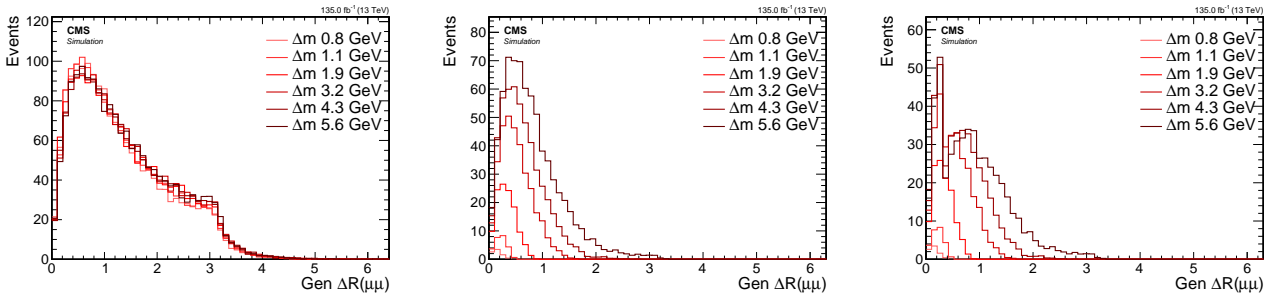


Figure 7.12: Signal generator level ΔR distributions with no cuts (left), with $p_T(\mu_i) > 2 \text{ GeV}$, $i = 1, 2$ (middle) and with SOS orthogonality condition $p_T(\mu_i) > 2 \text{ GeV}$, $p_T(\mu_2) \leq 3.5 \text{ GeV}$ or $\Delta R \leq 0.3$ (right).

The left plot of Figure 7.12 shows that roughly the same number of events are produced for all Δm model points. However, when applying a cut of $p_T(\mu) > 2 \text{ GeV}$, a hierarchy of Δm points emerges, with fewer events as Δm becomes smaller (middle plot). The spike on the right plot is due to the SOS orthogonality condition, which requires $\Delta R(\ell\ell) \leq 0.3$ as one of two conditions in an or statement.

To understand the shaping and hierarchy formation due to the p_T cut, the p_T of the muons is plotted vs. $\Delta R(\ell\ell)$, as shown in Figure 7.13.

The hierarchy can be understood by observing that cutting on $p_T(\mu_2) \geq 2 \text{ GeV}$ for $\Delta m = 1.13 \text{ GeV}$ will limit the range of $\Delta R(\mu\mu)$ to less than 0.4, while leaving a large range exceeding 3 for the $\Delta m = 5.63 \text{ GeV}$ model point. It can be concluded that in order to gain access and sensitivity to the low Δm model points, probing low $\Delta R(\ell\ell)$ values, potentially with values less than 0.3, is necessary, even before considering the reconstruction efficiency of the leptons. In the next sections, the study of reconstructed leptons and the definition of isolation criteria will enable the retention of signal points with close lepton pairs, as further explored in Section 7.7.7.

As seen in Section 7.5.4.2 for $m_{\mu\mu}$, reconstruction has an effect on both the shape and overall count of events. The effects on the $\Delta R(\mu\mu)$ distributions are investigated in Figure 7.14.

When the reconstructed $\Delta R(\mu\mu)$ distributions in Figure 7.14 are compared to the generator level ones in Figure 7.12, it can be observed that the main effect of the reconstruction on the $\Delta R(\mu\mu)$ is the overall normalization, which is due to reconstruction efficiency.

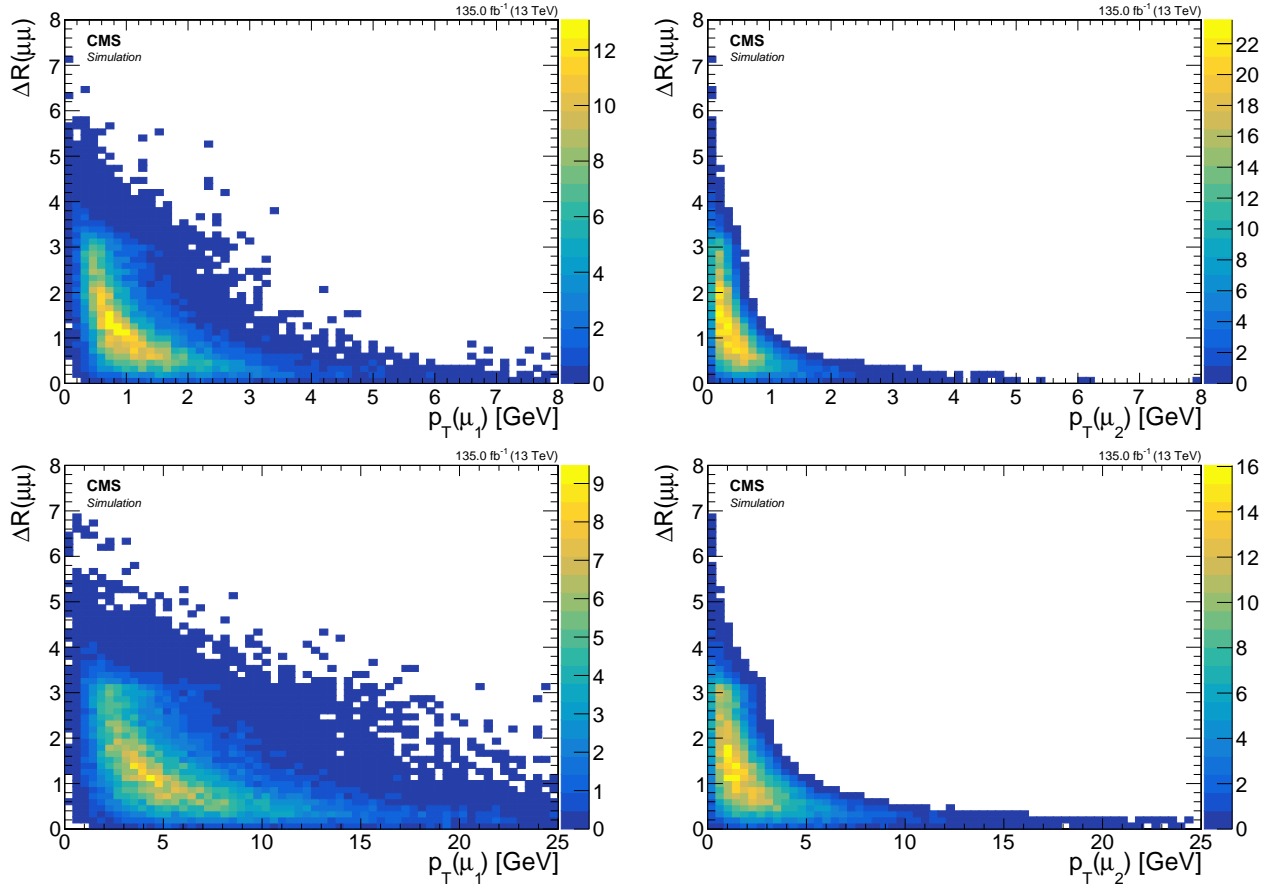


Figure 7.13: Signal $\Delta R(\mu\mu)$ vs. p_T for leading lepton μ_1 (left) and subleading lepton μ_2 (right) for $\Delta m = 1.13 \text{ GeV}$ (top) and $\Delta m = 5.63 \text{ GeV}$ (bottom).

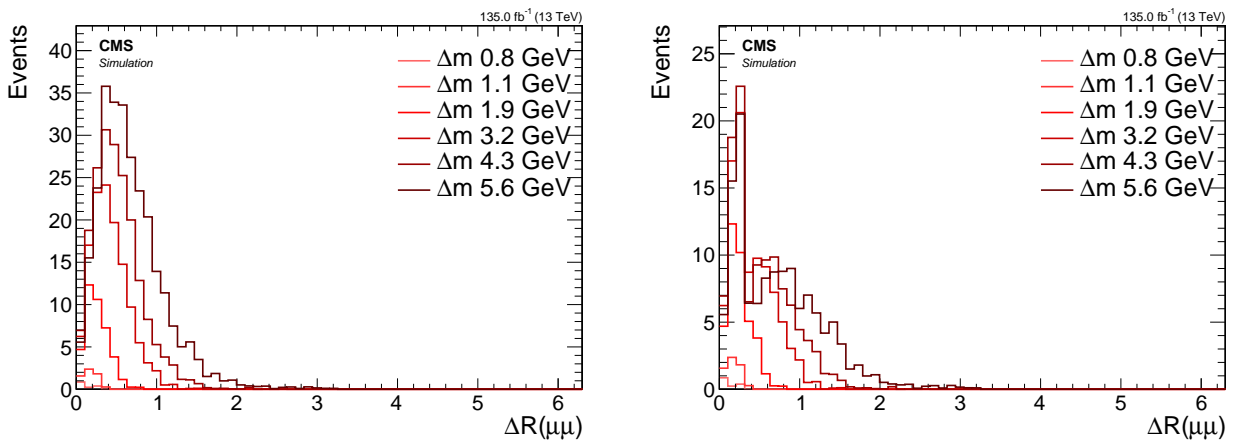


Figure 7.14: Signal reconstructed $\Delta R(\mu\mu)$ with basic analysis selection (left) and additional SOS orthogonality condition (right).

7.5.5 Main drivers of sensitivity

Conclusions can be drawn from this signal distribution studies in regards to the main drivers to the sensitivity of different model points of this analysis, as well as of future analysis that might try to expand on this one. This section does not consider SM background at all, making it hard to conclude what effects changing the cuts to E_T^{miss} or other event level observables might have. However, one thing is very clear from examining the dilepton kinematics, and that is to gain access to low Δm model points, the threshold on the p_T of the decay leptons must be lowered and low ΔR must be probed. Another driver of the sensitivity at all Δm model points is the luminosity, since the production cross section drops as a function of the higgsino mass parameter μ .

The next sections will explore how to lower the threshold on the muons transverse momentum and deal with collimated leptons that might pose a challenge in regards to the isolation criterion.

7.6 Simulated samples

7.6.1 Standard Model simulated samples

7.6.2 Signal simulated samples

7.7 Object definition and selection

In Section 6, the reconstruction and identification of objects in the detector were presented. Additionally, the signal signature was studied in Section 7.5. In this section, an object selection is devised to obtain a sample of objects that is as pure as possible with respect to the target leptons, while still retaining as much signal as possible. As discussed in Section 7.4, the focus is on selecting opposite-charged, same-flavor leptons $\ell^+ \ell^-$ resulting from the $\tilde{\chi}_2^0$ that decays into a $\tilde{\chi}_1^0$ via a Z^* , i.e., $\tilde{\chi}_2^0 \rightarrow \tilde{\chi}_1^0 \ell^+ \ell^-$. Two choices of Δm^0 are presented in the following section: a relatively high Δm^0 of $\Delta m^0 = 5.63 \text{ GeV}$ and a low Δm^0 of $\Delta m^0 = 1.92 \text{ GeV}$, but not so low as to prevent enough electrons from surviving the initial reconstruction p_T threshold of 5 GeV. The higgsino parameter is fixed at $\mu = 100 \text{ GeV}$.

In Section 7.5, the base selection required at least one jet in the event with $p_T \geq 30 \text{ GeV}$ and $|\eta| < 2.4$, without any other selections. However, unlike in that section, objects are not weighted to any luminosity in this section, as the focus is on the proportion between object types. Two types of leptons are differentiated: those originating from the targeted decay $\tilde{\chi}_2^0 \rightarrow \tilde{\chi}_1^0 \ell^+ \ell^-$, shown in blue, and those that do not, referred to as *other*, shown in yellow. Signal leptons are marked as such by matching a reconstructed lepton to a generator level lepton, which has been confirmed to have the $\tilde{\chi}_2^0$ as its parent. Leptons marked as *other* may have been misreconstructed, misidentified, or may be a result of the hadronisation process in a jet (such as the ISR jet). The goal is to select as many blue leptons as possible while rejecting as many yellow ones as possible. In the following sections, the term *efficiency* refers to the proportion of signal leptons passing a selection, divided by the initial number of signal leptons, and the term *purity* refers to the proportion of signal leptons (blue) to the sum of the signal leptons and *other* leptons (yellow). In other words, the goal is to find a selection with high efficiency and high purity. However, these two quantities can sometimes compete with each other, requiring compromises.

7.7.1 Electrons

The electrons are subject to an initial reconstruction p_T threshold of 5 GeV, and are reconstructed using a loose working point, as described in Section 6. The first distribution of interest regarding the electrons is their spatial separation from the leading jet in the event, denoted as $\Delta R(j_1, e)$. The distributions can be seen in Figure 7.15.

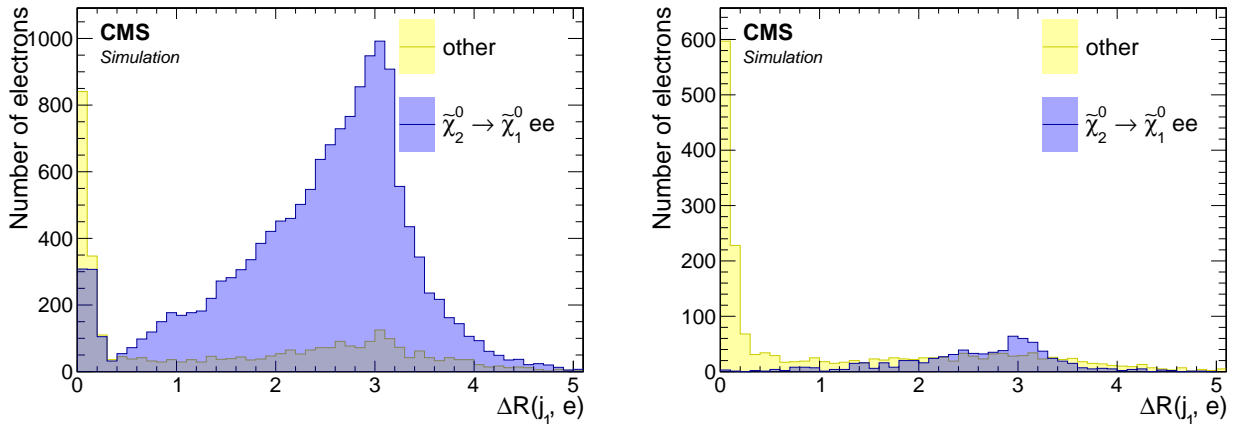


Figure 7.15: Spatial separation between reconstructed electrons with loose ID and the leading jet $\Delta R(j_1, e)$ for $\Delta m = 5.63 \text{ GeV}$ (left) and $\Delta m = 1.92 \text{ GeV}$ (right).

The plots in Figure 7.15 reveal two key features. The first one has already been discussed in Section 7.5, which is that probing lower Δm necessitates access to low p_T leptons. Therefore,

the threshold of $p_T \geq 5$ GeV on the electrons leads to reduced signal acceptance. This is evident from the difference between the high and low Δm cases. The second interesting feature is that the signal electrons are predominantly located outside the leading jet. This is because the leading jet is typically an ISR jet, which boosts the $\tilde{\chi}_2^0 \tilde{\chi}_1^0$ system away from it, causing them to be back-to-back. Thus, a cut of $\Delta R(j_1, e) > 0.4$ is made to account for this.

In this step, the p_T distributions of electrons are examined by applying the $\Delta R(j_1, e) > 0.4$ cut. It is observed that the p_T distribution depends heavily on the Δm , which has been previously demonstrated for muons in Section 7.5.4.1. While the distributions in that section were plotted using generator level muons, the p_T distributions for electrons follow the same trend. Thus, a choice must be made regarding which Δm to prioritize, and the lower Δm case is chosen for increased sensitivity. However, the two choices are compared in Figure 7.16.

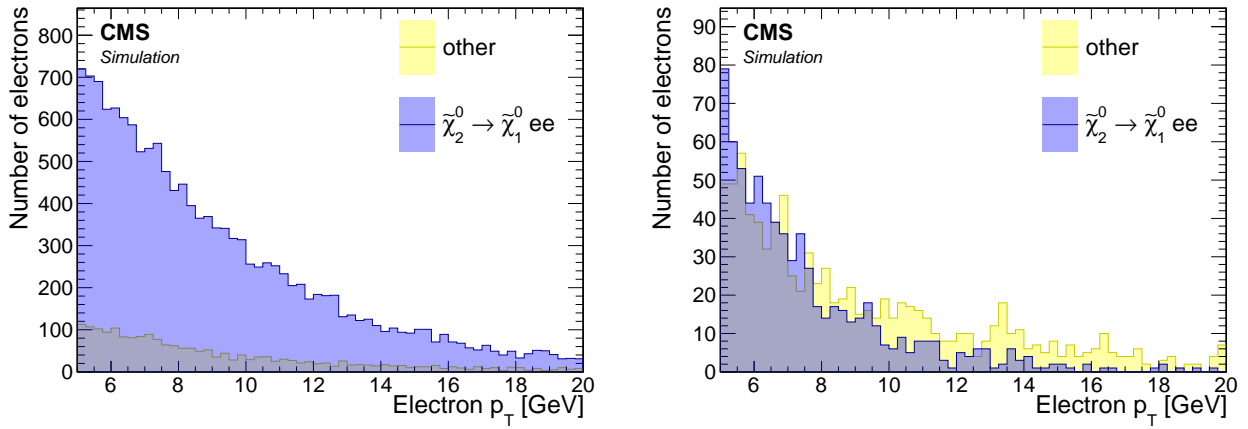


Figure 7.16: p_T distribution of reconstructed electrons with loose ID for $\Delta m = 5.63$ GeV (left) and $\Delta m = 1.92$ GeV (right). Cut of $\Delta R(j_1, e) > 0.4$ applied.

As expected, the p_T distribution of the electrons falls more rapidly for the low Δm case. It is observed that there are hardly any electrons surviving above 15 GeV. Therefore, a cut of $p_T < 15$ GeV is chosen.

The η distribution is interesting to look at, as seen in Figure 7.17, after the previous cuts to gain a better understanding of where most of the non-signal electrons originate from.

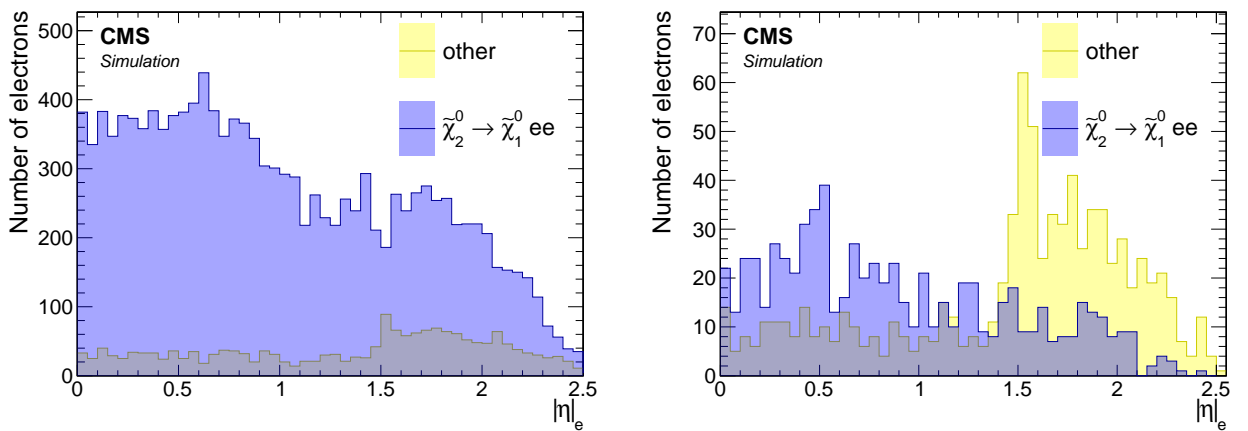


Figure 7.17: $|\eta|$ distribution of reconstructed electrons with loose ID for $\Delta m = 5.63$ GeV (left) and $\Delta m = 1.92$ GeV (right). Cuts of $\Delta R(j_1, e) > 0.4$ and $p_T < 15$ GeV are applied.

For the $\Delta m = 1.92$ GeV case, it can be clearly seen that the endcaps of the Electromagnetic Calorimeter (ECAL) are performing worse compared to the barrel ($|\eta| < 1.48$). The transition

is easily noticeable through a sharp drop in purity at the transition. It is even worse for low- p_T electrons than for higher- p_T ones.

To determine whether a tighter working point for the electron-identification is beneficial, the effects of requiring either a medium or a tight working point are investigated. The working point previously used in the distributions is the loose working point. Two bins labeled *fail* and *pass* are plotted to correspond to whether the electron fails or passes the identification criteria of medium or tight working points. These bins are shown in Figure 7.18.

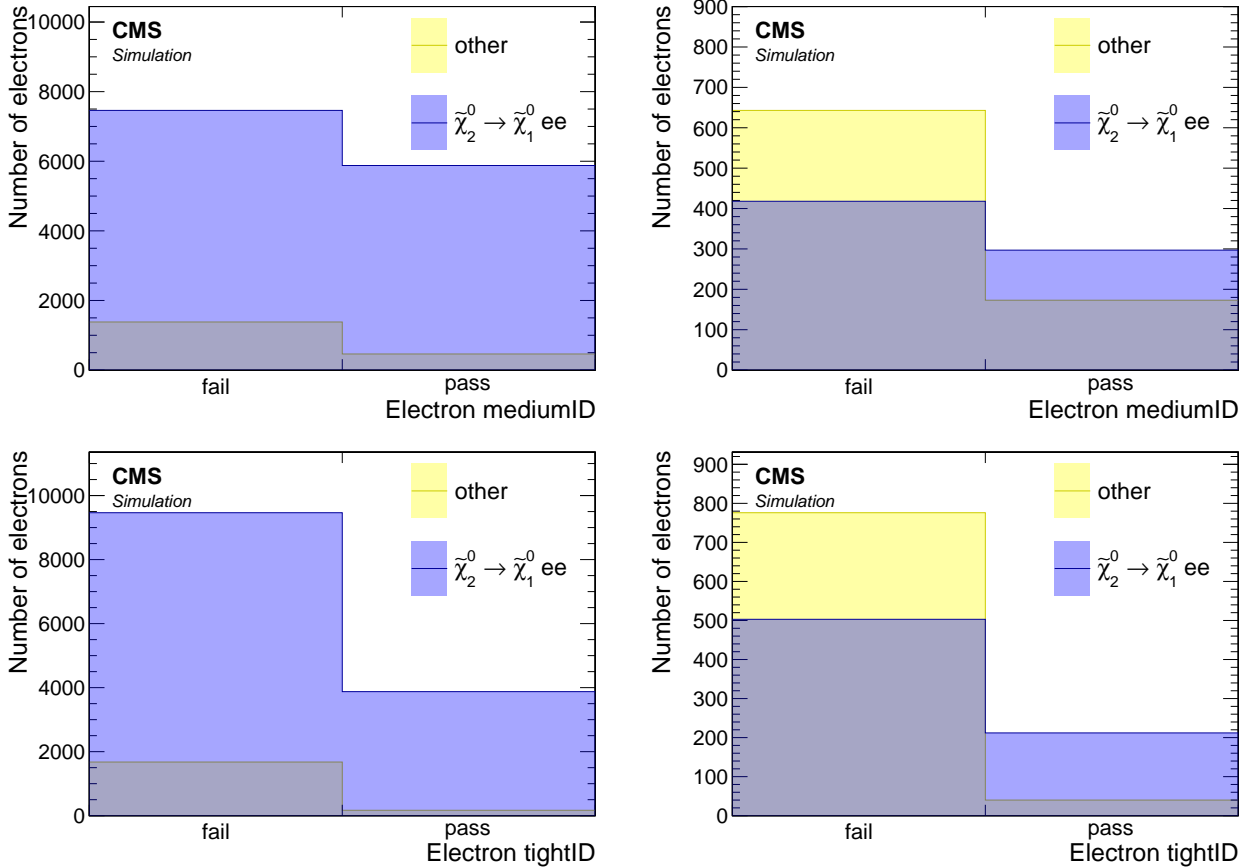


Figure 7.18: Medium (top) and tight (bottom) ID working points distributions of reconstructed electrons for $\Delta m = 5.63 \text{ GeV}$ (left) and $\Delta m = 1.92 \text{ GeV}$ (right). Cuts of $\Delta R(j_1, e) > 0.4$ and $p_T < 15 \text{ GeV}$ are applied.

Selecting a medium or a tight working point is equivalent to choosing the relevant right *pass* bin (top for medium, bottom for tight), and rejecting the electrons on the left *fail* bin. We see that although we reject considerable amount of non-signal electrons in the low Δm case by picking either a medium or tight working points, we also loose quite a lot of signal electrons as well. In other words, these selections are very not efficient and will result in low signal acceptance. We therefore decide to use a loose working point for the electrons. We will see that we can still purify the electron selection by relying on isolation instead. We fully discuss and describe our jet-isolation in Section 7.7.7, but here for the sake of completeness we look at its effect on the purity of the electrons. We compare our custom jet-isolation to the standard definition of lepton isolation, which does not take into account the possibility that two electrons can be produced close to each other (small ΔR), as is the case in our signal. Comparison of the isolation distributions are seen in Figure 7.19.

Selecting a medium or a tight working point is equivalent to choosing the relevant right *pass* bin (top for medium, bottom for tight), and rejecting the electrons on the left *fail* bin. It can be seen that considerable amount of non-signal electrons are rejected in the low Δm case by

picking either a medium or tight working points, but a significant number of signal electrons are also lost. Therefore, using these selections is not very efficient and results in low signal acceptance. A decision is made to use a loose working point for the electrons, and instead rely on isolation to achieve higher purity. The effect of isolation on the purity of the electrons is therefore also examined. The jet-isolation is discussed in detail in Section 7.7.7, but for the sake of completeness, its effect on the purity of the electrons is also shown here. The custom jet-isolation is compared with the standard definition of lepton isolation, which does not take into account the possibility that two electrons can be produced close to each other (small ΔR), as is the case in the signal. The isolation distributions are shown in Figure 7.19.

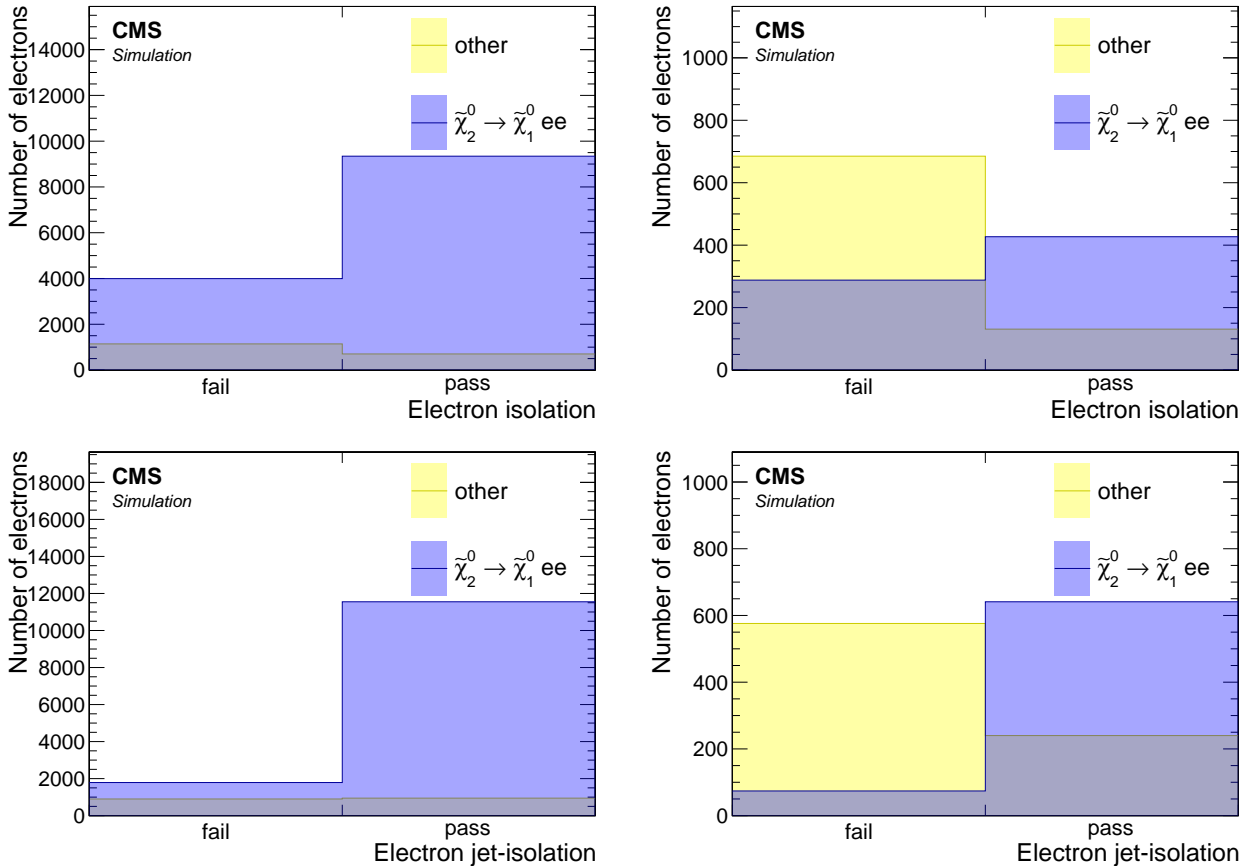


Figure 7.19: Standard isolation (top) and custom jet-isolation (bottom) distributions of reconstructed electrons with loose ID for $\Delta m = 5.63$ GeV (left) and $\Delta m = 1.92$ GeV (right). Cuts of $\Delta R(j_1, e) > 0.4$ and $p_T < 15$ GeV are applied.

It is observed that the standard lepton isolation is not efficient for both Δm cases, while the custom jet-isolation performs well in terms of signal electron efficiency and successfully rejects a considerable amount of non-signal electrons. This results in a purer sample of electrons, and thus the choice of custom jet-isolation is concluded to be favorable. The effect of this choice on the η distribution is also examined in Figure 7.20, concluding the selection of electrons.

Distributions in Figure 7.20 show that the custom jet-isolation has further purified the electron selection while retaining signal electrons, compared to distributions in Figure 7.17.

To summarize this section, the following is the full selection of the analysis electrons:

- $5 < p_T < 15$ GeV
- $|\eta| < 2.5$
- $\Delta R(j_1, e) > 0.4$

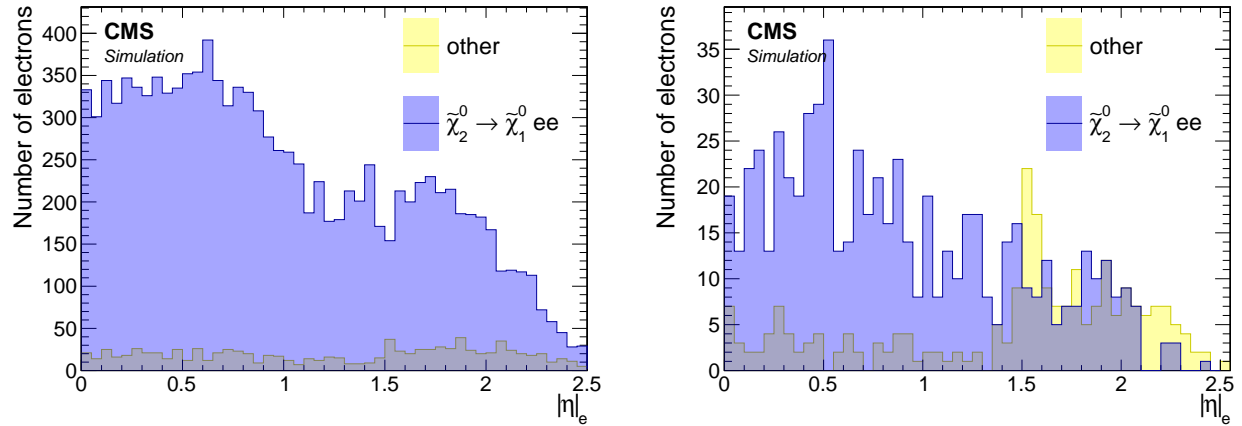


Figure 7.20: $|\eta|$ distribution of reconstructed electrons with loose ID passing jet-isolation for $\Delta m = 5.63 \text{ GeV}$ (left) and $\Delta m = 1.92 \text{ GeV}$ (right). Cuts of $\Delta R(j_1, e) > 0.4$ and $p_T < 15 \text{ GeV}$ are applied.

- loose ID working point
- pass jet-isolation

7.7.2 Muons

In contrast to electrons, the initial reconstruction p_T threshold for muons is not set to 5 GeV. Hence, the possibility of lowering the p_T threshold as much as possible is explored. This was motivated in section 7.5.4.1 where it was observed that the lower the Δm to be probed, the lower the p_T threshold has to be. Similarly to the electrons case, the initial working point choice for reconstructed muons is loose (see 6). A similar procedure to the electron case is followed. The spatial separation of muons from the leading jet in the event, $\Delta R(j_1, \mu)$, is the first distribution examined. As shown in Figure 7.7, the muon endcaps are capable of reconstructing muons with $p_T < 3$ GeV while the barrel cannot. Therefore, it makes sense to look at a split view of barrel and endcaps for the following distributions at 7.21.

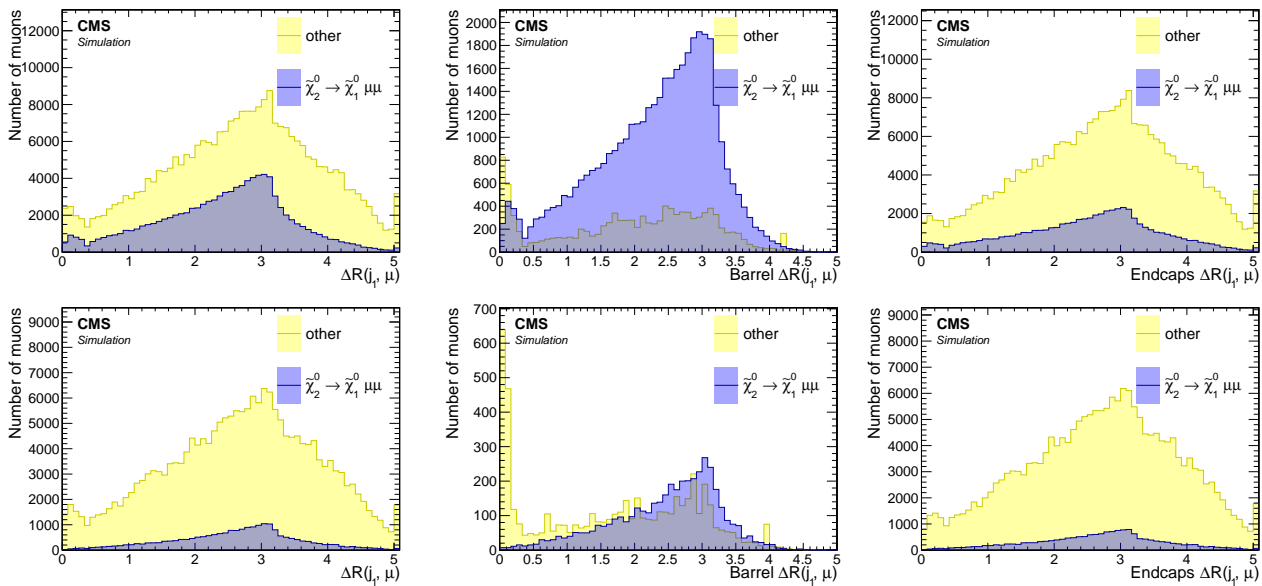


Figure 7.21: Spatial separation between reconstructed muons with loose ID and the leading jet $\Delta R(j_1, \mu)$ for $\Delta m = 5.63$ GeV (top) and $\Delta m = 1.92$ GeV (bottom) in the inclusive case (left), barrel (middle) and endcaps (right).

Since the muons in the endcaps have lower p_T than the muons in the barrel, which is only able to reconstruct muons with $p_T > 3$ GeV, the purity in the endcaps is much lower than the purity in the barrel. The selection being constructed here attempts to further purify the muons. Muons with $\Delta R(j_1, \mu) > 0.4$ are selected like in the electrons case, and this selection will apply for the rest of the section.

Next, the p_T distributions are examined. The previous cut of $\Delta R(j_1, \mu) > 0.4$ is applied. As seen in Section 7.5.4.1, the p_T distribution depends strongly on Δm , and the low Δm acceptance is favored to be more sensitive to it. The p_T distributions seen in Figure 7.22 suggest a cut identical to the electron case of $p_T < 15$ GeV. It is worth mentioning that the p_T of the muons are fed into the training of the Boosted Decision Tree (BDT) for further refinement, and therefore the exact value is being determined here quite loosely. The actual maximum value of the p_T of the muons will depend on the BDT cut being used to define the signal region.

The feature discussed earlier, whereby the endcaps are capable of reconstructing muons with lower p_T and therefore have worse purity than the barrel, is reiterated here. It is important to stress that the worse purity is due to a much higher efficiency, and as long as the muons can be purified further, it is not necessarily a bad thing. The bulk of the non-signal muons populate the region of $p_T < 2$ GeV, and the ratio of signal muons to non-signal muons is very low in that region. An additional cut of $p_T > 2$ GeV is therefore made. Another way of looking at the effect of this cut is by examining the $|\eta|$ distribution before and after the p_T cut, which can be

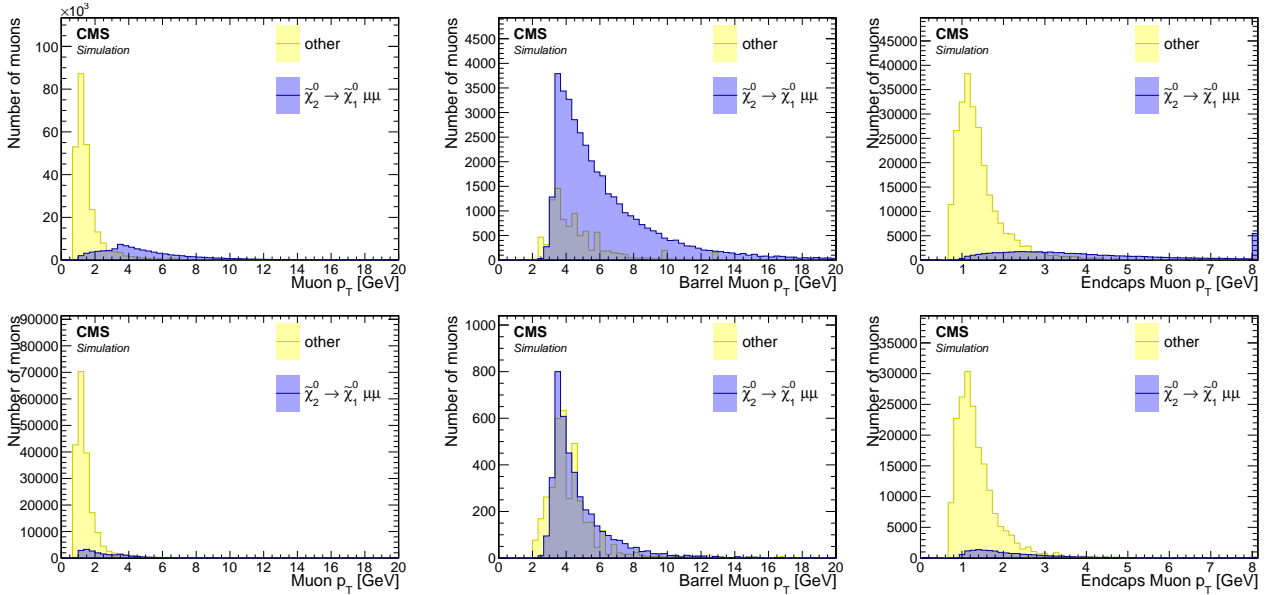


Figure 7.22: Reconstructed muons p_T distribution with loose ID for $\Delta m = 5.63 \text{ GeV}$ (top) and $\Delta m = 1.92 \text{ GeV}$ (bottom) in the inclusive case (left), barrel (middle) and endcaps (right). Cuts of $\Delta R(j_1, \mu) > 0.4$ and $p_T < 15 \text{ GeV}$ are applied.

seen in Figure 7.23.

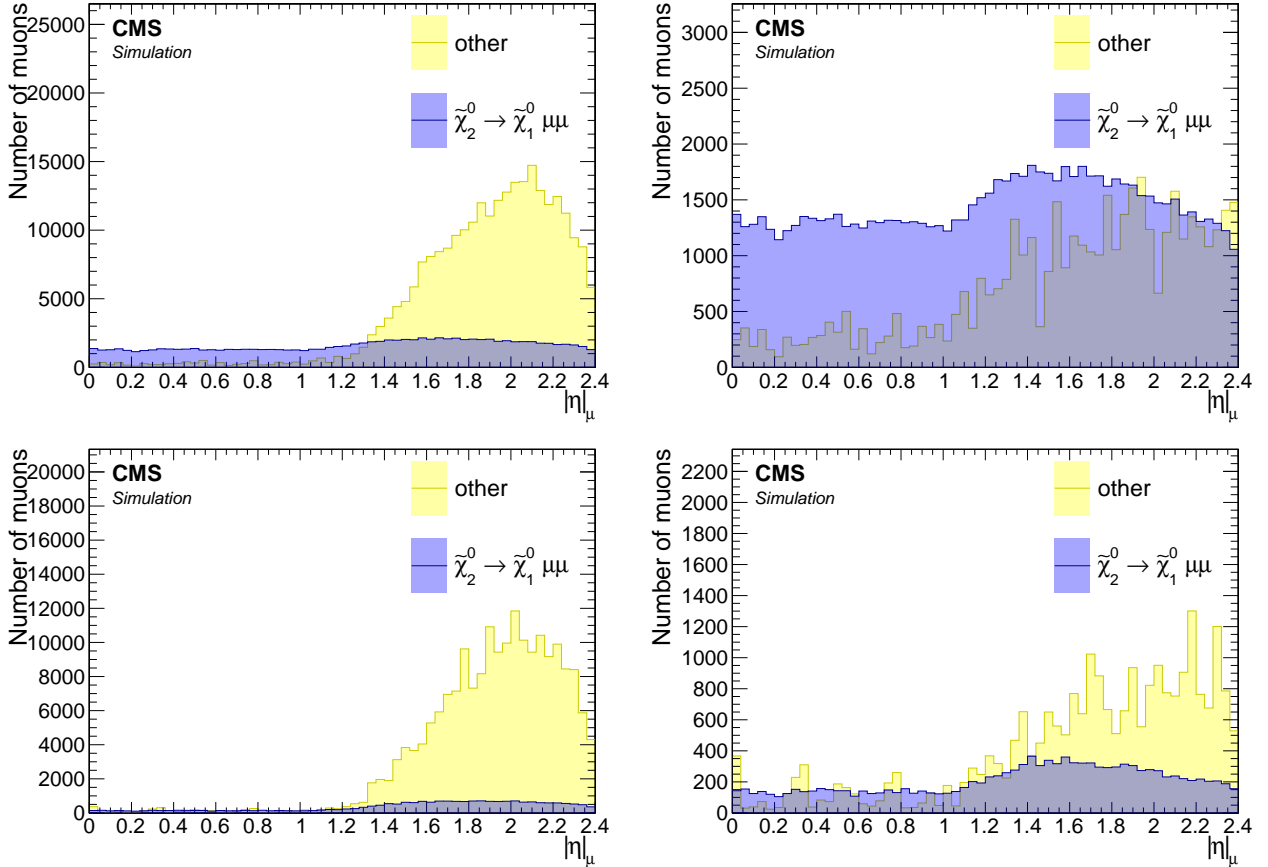


Figure 7.23: $|\eta|$ distribution of reconstructed muons with loose ID for $\Delta m = 5.63 \text{ GeV}$ (top) and $\Delta m = 1.92 \text{ GeV}$ (bottom) without (left) and with (right) $p_T > 2 \text{ GeV}$ cut. Cut of $\Delta R(j_1, \mu) > 0.4$ is also applied.

To see if requiring a tighter working point for the muon-identification is beneficial, it is

necessary to test the effects of requiring either a medium working point, or a tight one. Two bins labeled *fail* and *pass* are plotted, which correspond to whether the muon passes or fails the identification criteria of a medium or tight working points.

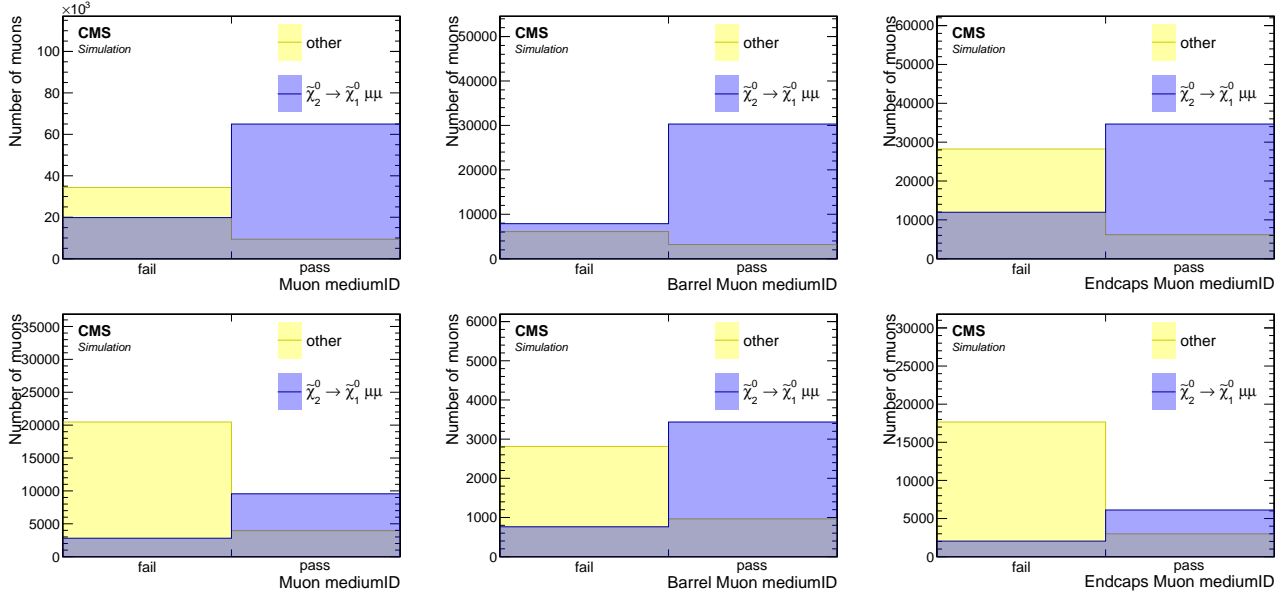


Figure 7.24: Medium ID working point distributions of reconstructed muons for $\Delta m = 5.63 \text{ GeV}$ (top) and $\Delta m = 1.92 \text{ GeV}$ (bottom) in the inclusive p_T case (left), barrel (middle) and endcaps (right). Cuts of $\Delta R(j_1, \mu) > 0.4$, $p_T > 2 \text{ GeV}$ and $p_T < 15 \text{ GeV}$ are applied.

Comparing the medium working point in Figure 7.24 to the tight working point in Figure 7.25, it is apparent that the medium working point is very beneficial in purifying the muons. However, when the tight working point is used, a significant number of wanted signal-muons are lost without a significant gain in purity. Therefore, the medium ID working point is chosen.

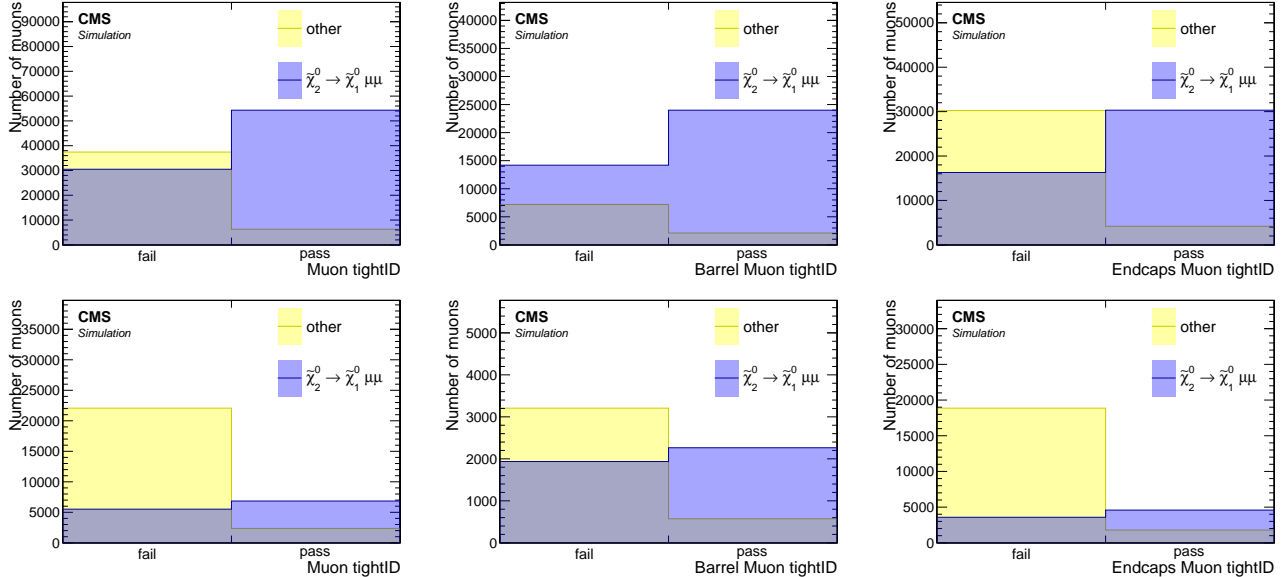


Figure 7.25: Tight ID working point distributions of reconstructed muons for $\Delta m = 5.63 \text{ GeV}$ (top) and $\Delta m = 1.92 \text{ GeV}$ (bottom) in the inclusive p_T case (left), barrel (middle) and endcaps (right). Cuts of $\Delta R(j_1, \mu) > 0.4$, $p_T > 2 \text{ GeV}$ and $p_T < 15 \text{ GeV}$ are applied.

The custom jet-isolation was designed to reject SM background while retaining signal, as

described in Section 7.7.7. For electrons, as shown in Figure 7.19, it effectively purified the selection and eliminated the need for a tighter identification working point. As for muons, although a medium working point is relied upon to perform this task, the effects of the isolation on signal muons are still of interest. Figure 7.26 shows that a small price is paid by requiring the isolation. However, as will be seen in Section 7.7.7, the sensitivity is increased by rejecting a lot of SM background in the process.

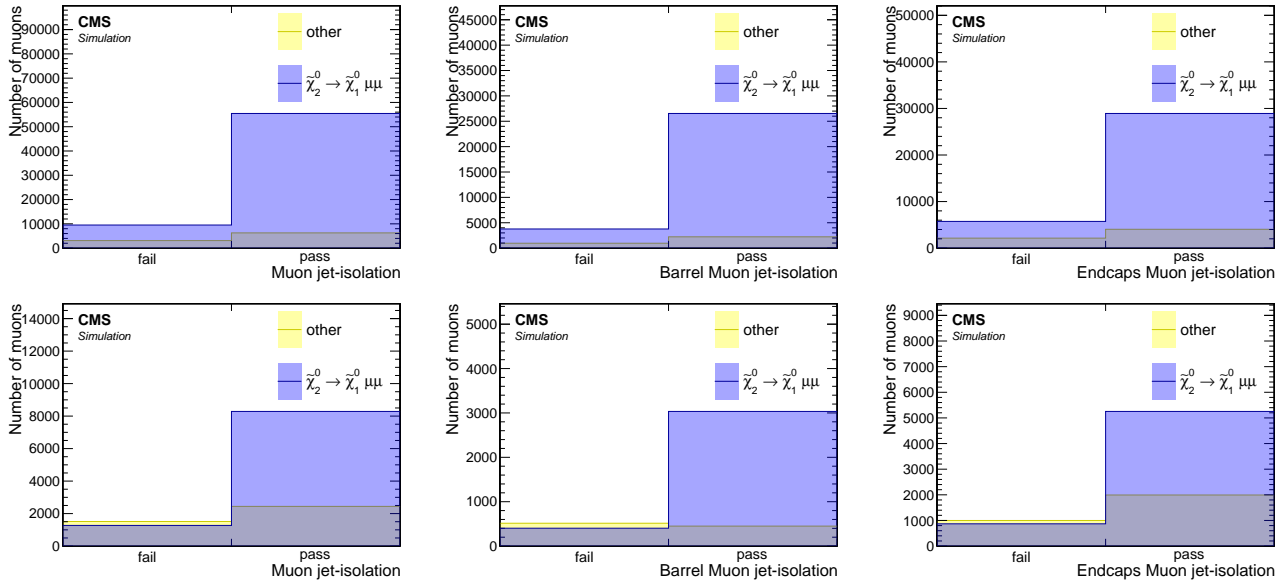


Figure 7.26: Jet-isolation distributions of reconstructed muons with medium ID for $\Delta m = 5.63 \text{ GeV}$ (top) and $\Delta m = 1.92 \text{ GeV}$ (bottom) in the inclusive p_T case (left), barrel (middle) and endcaps (right). Cuts of $\Delta R(\gamma_1, \mu) > 0.4$, $p_T > 2 \text{ GeV}$ and $p_T < 15 \text{ GeV}$ are applied.

To summarize this section, the following is the full selection of the analysis muons:

- $2 < p_T < 15 \text{ GeV}$
- $|\eta| < 2.4$
- $\Delta R(\gamma_1, \mu) > 0.4$
- medium ID working point
- pass jet-isolation

7.7.3 Scale factors

In Section 7.7.1 and Section 7.7.2, the selection applied to electrons and muons respectively was studied, and a choice was made regarding the identification working point. Simulation was exclusively used to draw conclusions about the identification efficiency of the leptons. However, relying solely on Monte Carlo (MC) simulation can produce significant systematic errors due to imperfections in modeling both the data and the detector response. Therefore, measuring the identification efficiency in data is necessary to correct any potentially false efficiency rates in the simulation. The term *efficiency* refers to the probability of reconstructing or identifying a lepton. For a lepton ℓ , the identification efficiency is defined as:

$$\varepsilon_{\ell}^{\text{ID}} = \frac{N_{\ell}(\text{ID})}{N_{\ell}(\text{produced})} \quad (7.1)$$

In MC simulation, the number of produced leptons is the same as the number of generated leptons. However, in data, the efficiency must be measured using a data-driven method. Once the efficiencies have been measured both in simulation and data, a correction factor called the Scale Factor (SF) can be applied to the simulation to correct any discrepancies that may arise. Scale factors are defined as the ratio between the efficiency in data and the efficiency in simulation:

$$\text{SF}_{\ell}^{\text{ID}} = \frac{\varepsilon_{\ell}^{\text{ID,Data}}}{\varepsilon_{\ell}^{\text{ID,MC}}}, \quad (7.2)$$

dropping the superscript ID, this becomes:

$$\text{SF}_{\ell} = \frac{\varepsilon_{\ell}^{\text{Data}}}{\varepsilon_{\ell}^{\text{MC}}}. \quad (7.3)$$

Once the relevant SF have been determined, they are applied to every lepton that passes the object selection in the event. The scale factors for loose-ID electrons in the relevant p_T range have been centrally measured by the corresponding working group and are applied to the selected electrons. As determined in Section 7.7.2, the analysis signal muon's lower p_T threshold is 2 GeV, which is low. Scale factors for medium ID leptons with $p_T \geq 2$ GeV were computed centrally by the Muon Physics Object Group (POG). However, the scale factors were computed by requiring $\Delta R > 0.5$ between the muons, as mentioned in [2, 3], and while they match the muons' p_T range and identification working point, $\Delta R < 0.5$ is one of the drivers of sensitivity, as seen in Section 7.5.4.3. Therefore, it is necessary to validate the scale factors in that region and show that the efficiencies have no ΔR dependence. To do so, the efficiencies in different ΔR regions are calculated.

In order to measure such efficiencies in data, one must identify desired leptons with low and easily reducible fakes. A widely used method to perform such a data-driven task is the Tag & Probe method. This involves examining a mass resonance such as Z, J/ ψ or Y to select particles of the desired type, and probing the efficiency of a particular selection criterion on those particles. The mass resonance then decays into two same-flavor opposite charged pairs of leptons, forming a peak on top of a background. To measure the efficiency of low p_T muons, dimuon events around the J/ ψ mass window are chosen. One muon is labeled as a ‘tag’ and the other as a ‘probe’. The tag muon is selected with a very tight selection resulting in high certainty that the object corresponds to a real produced muon. The probe is given a loose selection but constrained to be consistent with a product of a J/ ψ , almost certainly originating from a real muon as well. The background is easily removed by fitting the shape of the J/ ψ . The probe is then subjected to cuts or constraints, used to measure a particular efficiency. This

study aims to show that the efficiency to identify a muon with a medium ID working point from a track has no ΔR dependence. Therefore, the efficiency in question is defined as:

$$\varepsilon_\mu^{\text{ID}} = \frac{N_\mu^{\text{ID}}}{N_t}. \quad (7.4)$$

The denominator probe used in the study refers to a track that has passed a loose selection, while the numerator probe track is required to match a medium ID working point muon. To determine the number of objects passing a selection, a fit is performed on data and MC samples to measure the corresponding efficiencies.

This study was conducted for the year 2016. The 2016 samples listed in Section 7.6.1 are used for MC. To ensure the independence of the tagged muon from the triggered object, a single electron trigger is used for data. The corresponding data set is measured to be 36.02 fb^{-1} using the BRIL Work Suite [4]. The following trigger paths are utilized:

- `HLT_Ele27_WPTight_Gsf_v*`,
- `HLT_Ele27_eta2p1_WP Loose_Gsf_v*`,
- `HLT_Ele32_WPTight_Gsf_v*`,
- `HLT_Ele35_WPTight_Gsf_v*`.

An offline loose ID electron with $p_T > 27 \text{ GeV}$ is then selected. The requirements to select a tag & probe pair are defined in Table 7.7.3.

Table 7.3: Selection criteria for Tags and Probes

Tag	Probe
medium ID muon	isolated track
$p_T \geq 5 \text{ GeV}$	$2 \leq p_T \leq 20 \text{ GeV}$ ($p_T \geq 3 \text{ GeV}$ for barrel)
$ \eta < 2.4$	opposite-sign in invariant mass window $[2.5, 3.5] \text{ GeV}$

A fit is then performed in an invariant mass window around the J/ψ peak of $[2.5, 3.5] \text{ GeV}$. The signal fit uses a crystal ball function, and the continuum is fit with a 6th order polynomial. The fit is repeated twice, where the denominator is based on probe tracks, and the numerator uses medium ID muons that have been matched to those tracks. The ΔR range has been split into three, and the $|\eta|$ of the muons has been divided into barrel ($|\eta| < 1.2$) and endcaps ($1.2 < |\eta| < 2.4$). Simulation fits are shown in Figure 7.27 for the barrel, and Figure 7.28 for the endcaps. Data fits are shown in Figure 7.29 for the barrel, and in Figure 7.30 for the endcaps.

The efficiencies and corresponding scale factors can be seen in Figure 7.31. The scale factors are statistically consistent with unity and show no discernible ΔR dependence. A similar study was carried out with simulation and data for 2017 and 2018 in [5], and no ΔR dependence was observed either. As a result of these studies, the recommendation from the POG is to use the calculated scale factors provided by them with an additional systematic uncertainty of 1% for muons with $p_T < 20 \text{ GeV}$.

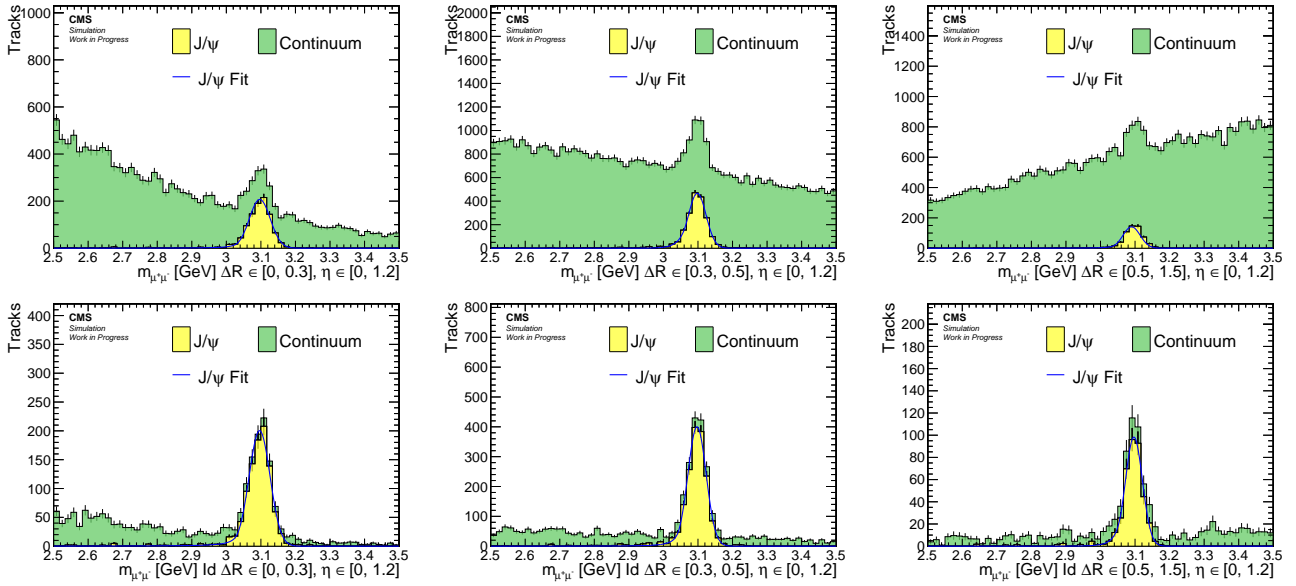


Figure 7.27: Simulation barrel muons fits for denominator (top) and numerator (bottom) for $0 < \Delta R < 0.3$ (left), $0.3 < \Delta R < 0.5$ (center), $0.5 < \Delta R < 1.5$ (right)

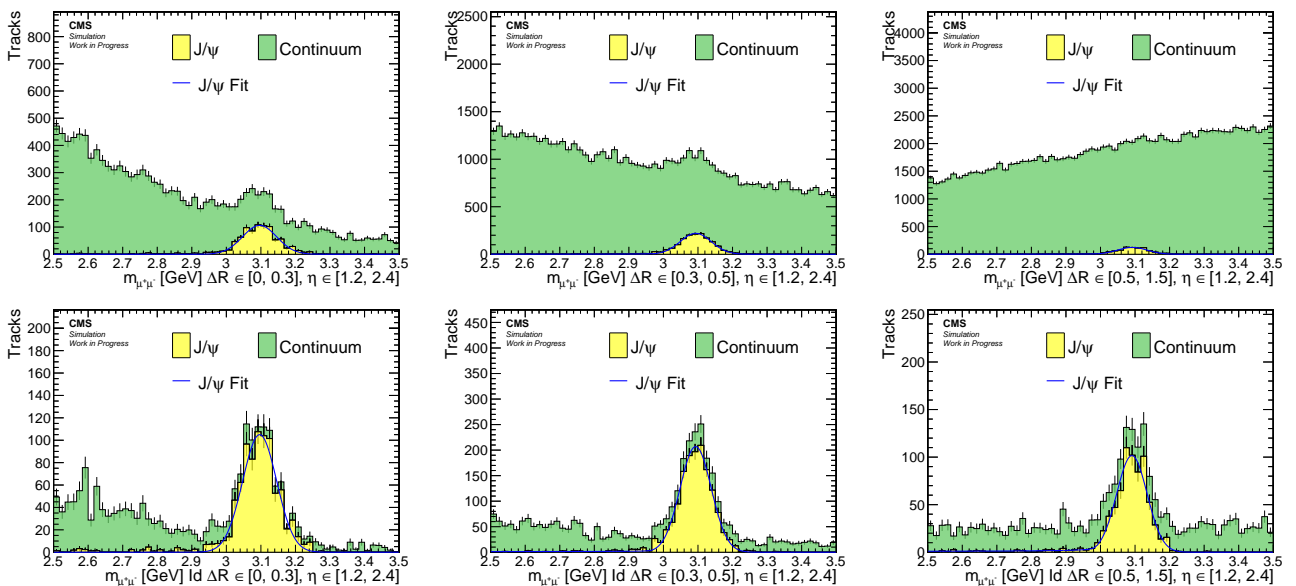


Figure 7.28: Simulation endcaps muons fits for denominator (top) and numerator (bottom) for $0 < \Delta R < 0.3$ (left), $0.3 < \Delta R < 0.5$ (center), $0.5 < \Delta R < 1.5$ (right)

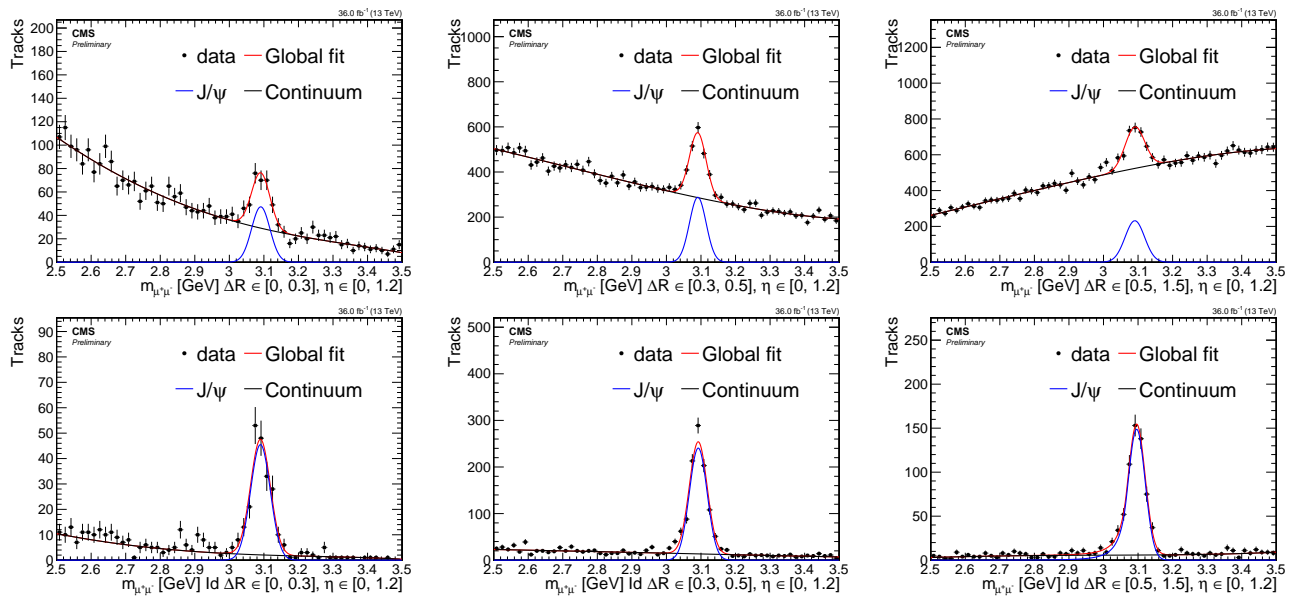


Figure 7.29: Data barrel muons fits for denominator (top) and numerator (bottom) for $0 < \Delta R < 0.3$ (left), $0.3 < \Delta R < 0.5$ (center), $0.5 < \Delta R < 1.5$ (right)

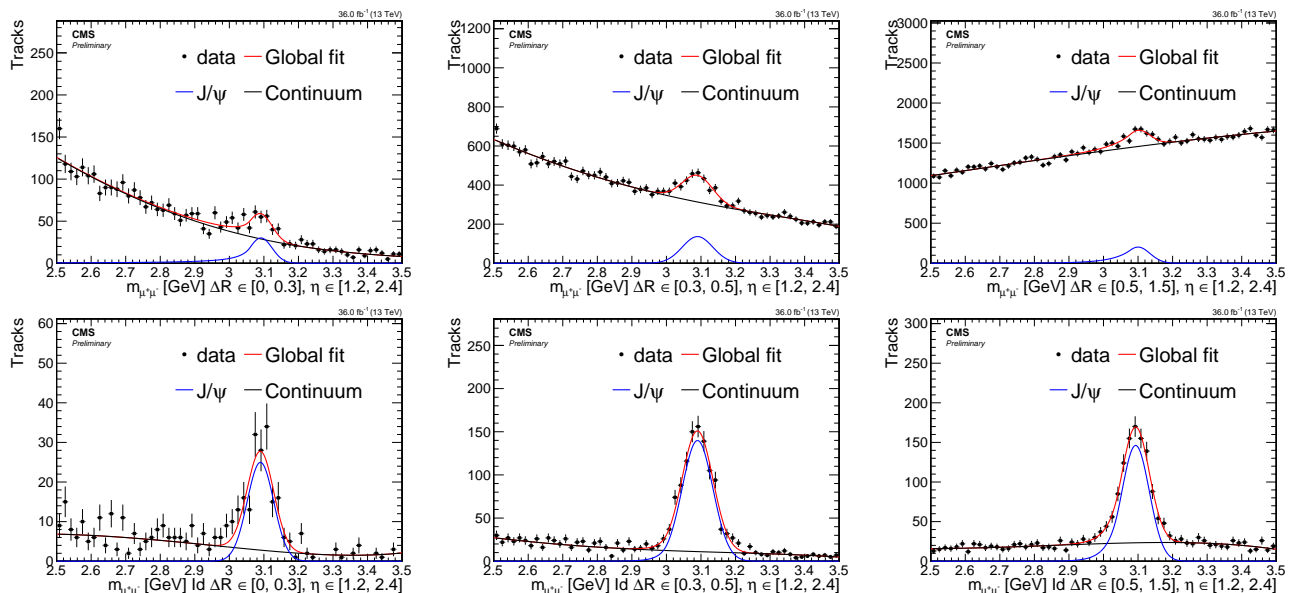


Figure 7.30: Data endcaps muons fits for denominator (top) and numerator (bottom) for $0 < \Delta R < 0.3$ (left), $0.3 < \Delta R < 0.5$ (center), $0.5 < \Delta R < 1.5$ (right)

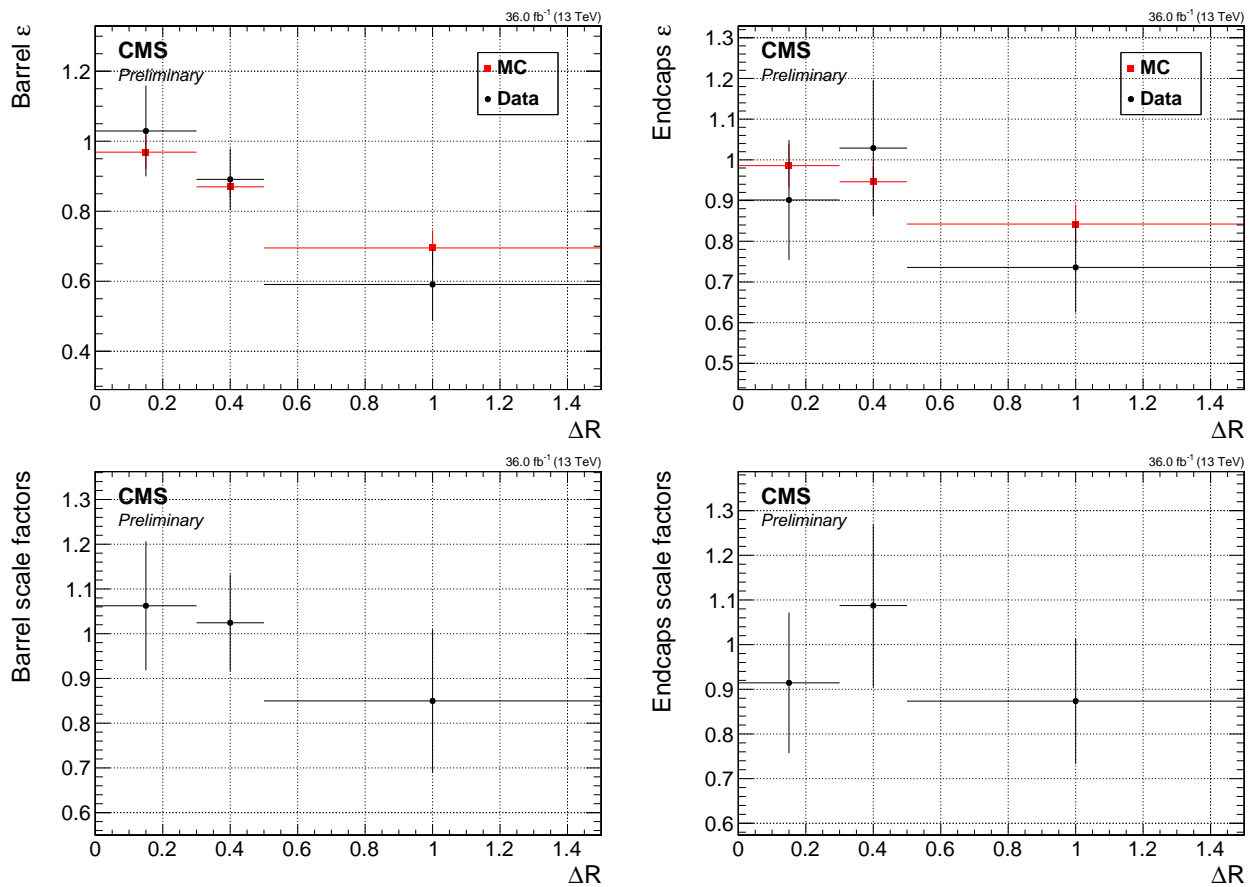


Figure 7.31: Efficiencies (top) and scale factors (bottom) for barrel muons (left) and endcaps muons (right).

7.7.4 Missing transverse energy

The importance of measuring the missing transverse momentum (or energy) in this analysis has been discussed in Section 7.5.1. It has been concluded that the missing transverse momentum is an essential ingredient in the analysis strategy. It is used to trigger events online and in the offline event level selection to boost sensitivity. Two standard measures of the momentum imbalance in the events are \vec{E}_T^{miss} (or \vec{p}_T^{miss} by a different symbol) and \vec{H}_T^{miss} . Although \vec{E}_T^{miss} and \vec{p}_T^{miss} have different symbols and are referred to by different names (missing transverse energy and missing transverse momentum respectively), they are defined in the same way and used interchangeably. Mathematically, \vec{E}_T^{miss} is defined as follows:

$$\vec{E}_T^{\text{miss}} = \vec{p}_T^{\text{miss}} = - \sum_i \vec{p}_T(i) \quad (7.5)$$

where the summation is done on all particle flow candidates. Therefore, the missing transverse energy serves as a measure of particles that evade detection, such as weakly interacting particles. Mismeasurements of visible particles and additional energy deposits from sources such as Pile-Up (PU), jet energy response and detector noise can affect this observable, so it undergoes further correction to mitigate these effects. The correction process considers jets with p_T greater than 10 GeV. Full details of the corrections can be found in [6].

An alternative measurement to the missing transverse momentum is \vec{H}_T^{miss} , which is sometimes referred to as *missing hardronic activity*. Instead of considering all particle flow candidates in the sum, this measurement only takes into account jets with p_T greater than 30 GeV and $|\eta| < 5$:

$$\vec{H}_T^{\text{miss}} = - \sum_i^{\text{jets}} \vec{p}_T(i) \quad (7.6)$$

The observable \vec{H}_T^{miss} is favored over \vec{E}_T^{miss} in this analysis, since the jet isolation, defined in Section 7.7.7, uses jets with p_T greater than 30 GeV, while a sideband is defined using the range of $p_T \in [15, 30]$ GeV of jets, which is then used for the data-driven background estimation method in Section 7.10.2.1. Both observables, \vec{E}_T^{miss} and \vec{H}_T^{miss} , have equivalent scalar quantities, E_T^{miss} and H_T^{miss} respectively, which can be obtained by taking the magnitude of their vectorial counterpart.

7.7.5 Jets

The reconstruction and identification of jets are described in Section 6.4. Jets used in the analysis are reconstructed by clustering the Particle Flow (PF) candidates using FASTJET and the anti- k_T algorithm [7] with a size parameter of 0.4. Tagging of b quark jets is performed using the multivariate technique DEEPCSV with a medium working point, also known as the Combined Secondary Vertex (CSV) algorithm. Jets are required to have a transverse momentum $p_T > 30$ GeV and $|\eta| < 2.4$.

7.7.6 Tracks and multivariate selection

The leptons $\ell^+ \ell^-$ produced in the decay $\tilde{\chi}_2^0 \rightarrow \tilde{\chi}_1^0 \ell^+ \ell^-$ tend to have mostly very low transverse momentum p_T . It has been shown in Section 6 that the identification and reconstruction of the muons worsen with lower p_T . Therefore, the aim of the exclusive track category is to attempt and recover lost leptons that were not reconstructed or identified. As seen in Section 6.1, the tracking efficiency at the p_T ranges used in this analysis is well above 99%, allowing the recovery of some of the tracks that correspond to the missing leptons by applying knowledge about the event kinematics specific to the signal. Thus, the exclusive track category does not enhance the lepton identification in the general case, but recovers missed tracks in this specific signal signature.

To identify which track corresponds to the miss-identified lepton in a given signal event, a Boosted Decision Tree (BDT) is trained. Four separate BDTs are trained, corresponding to the lepton flavor (muon or electron) and the phase of the tracker (phase 0 for 2016, and phase 1 for 2017-2018). All BDTs use a common structure of 200 trees with a maximum depth of 3, and are trained with AdaBoost and GiniIndex separation using the TMVA package [8]. Default values are used for all other parameters.

Tracks from our privately produced FASTSIM signal simulations listed in Section 7.6.2 are used for the training. The full range of simulated higgsino parameter μ (or the mass of $\tilde{\chi}_1^\pm$ in the case of phase 1) is considered, but only the range of Δm that this analysis targets. For phase 0, Δm^0 is chosen from the range $[0.3, 4.3]$ GeV and μ from $[100 - 130]$ GeV, while for phase 1, Δm^\pm is chosen from $[0.3 - 4.6]$ GeV and μ from $[100 - 500]$ GeV. Signal events are split into signal tracks and background tracks, with signal tracks originating from the decay $\tilde{\chi}_2^0 \rightarrow \tilde{\chi}_1^0 \ell^+ \ell^-$ and matching the missing generated lepton in the generator level particles collection, while background tracks do not match the wanted leptons. Therefore, the BDTs are useful for rejecting in-signal background of unwanted tracks. The samples for muons contain 9408 (10964) signal tracks and 99996 (151380) background tracks for phase 0 (phase 1). For electrons the samples contain 2364 (2288) signal tracks and 104065 (159713) background tracks for phase 0 (phase 1). The training samples are then tested against test samples of equal size. The distributions of the testing samples that overlay on the training samples can be seen in Figure 7.33.

A pre-selection is applied to all tracks in the collection obtained by the standard track reconstruction sequences. This pre-selection ensures that only properly-reconstructed, isolated, and prompt tracks are considered. The selected tracks must also have trajectories passing through the region near the primary vertex with the largest sum of charged-tracks, jets, and missing energy values (PV):

- $p_T > 1.9$ GeV
- $|\eta| < 2.4$
- track $\text{iso}_{\text{rel}} < 0.1$, using $\Delta R(\text{track}, \text{other tracks}) < 0.3$
- $d_{xy}(\text{track}, \text{PV}) < 0.02$ cm w.r.t the PV
- $d_z(\text{track}, \text{PV}) < 0.02$ cm w.r.t the PV
- no match to an electron or muon within a cone of size 0.01

For the training, a set of 10 variables listed in decreasing order of their ranking (in the muon case of phase 0) is used, as shown in Table 7.7.6.

Figure 7.32 shows the distribution of input variables, where signal tracks are shown in blue and background tracks in red.

Table 7.4: Track BDT input variables

Rank	Variable	Description
1	$\Delta R(t, \ell)$	t is the track and ℓ the lepton
2	$ \Delta\eta(t, \ell) $	
3	$p_T(\ell)$	
4	$ \Delta\phi(t, \vec{H}_T^{\text{miss}}) $	
5	$ \Delta\eta(t, j_1) $	j_1 is the leading jet
6	$ \Delta\phi(t, \ell) $	
7	$ \eta(t) $	
8	$ \eta(\ell) $	
9	$\Delta R(\ell, j_1)$	
10	$m_{t\ell}$	invariant mass

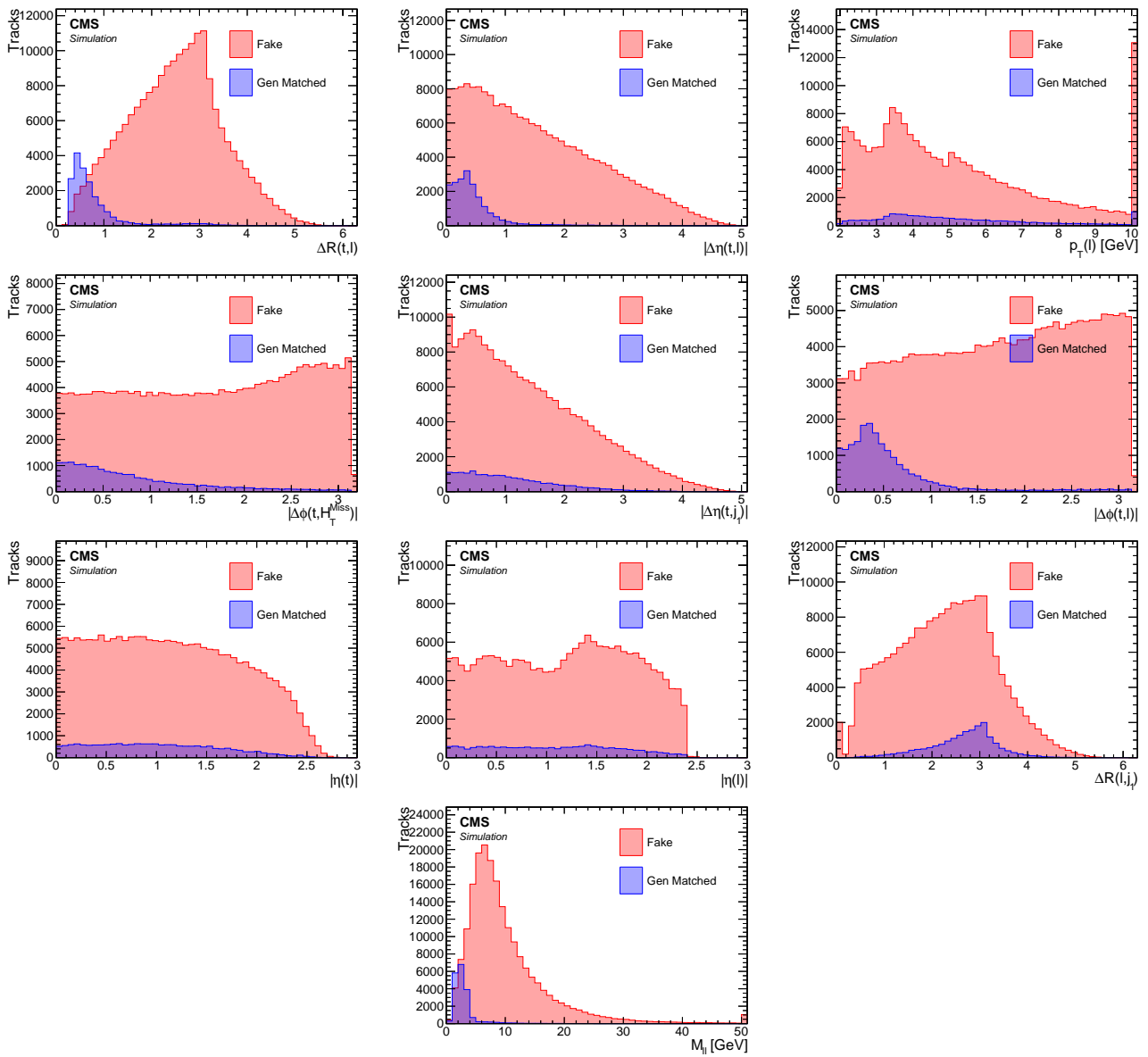


Figure 7.32: Distributions of the inputs for training for the track BDT in the Muon exclusive track category.

The output of the training for the 4 BDTs is displayed in Figure 7.33, where the testing distributions are superimposed on the training sample of the BDT. No obvious over-training

is observed. The ROC curves are then plotted in Figure 7.34, and the red point shows the efficiency of the signal and background tracks of the BDT cut, which is selected to be 0.0. A good separation between signal tracks and fake tracks is obtained, as evidenced by the relatively high signal efficiency of over 90% (86%) for muons (electrons) and background rejection of around 86% (76%) for muons (electrons).

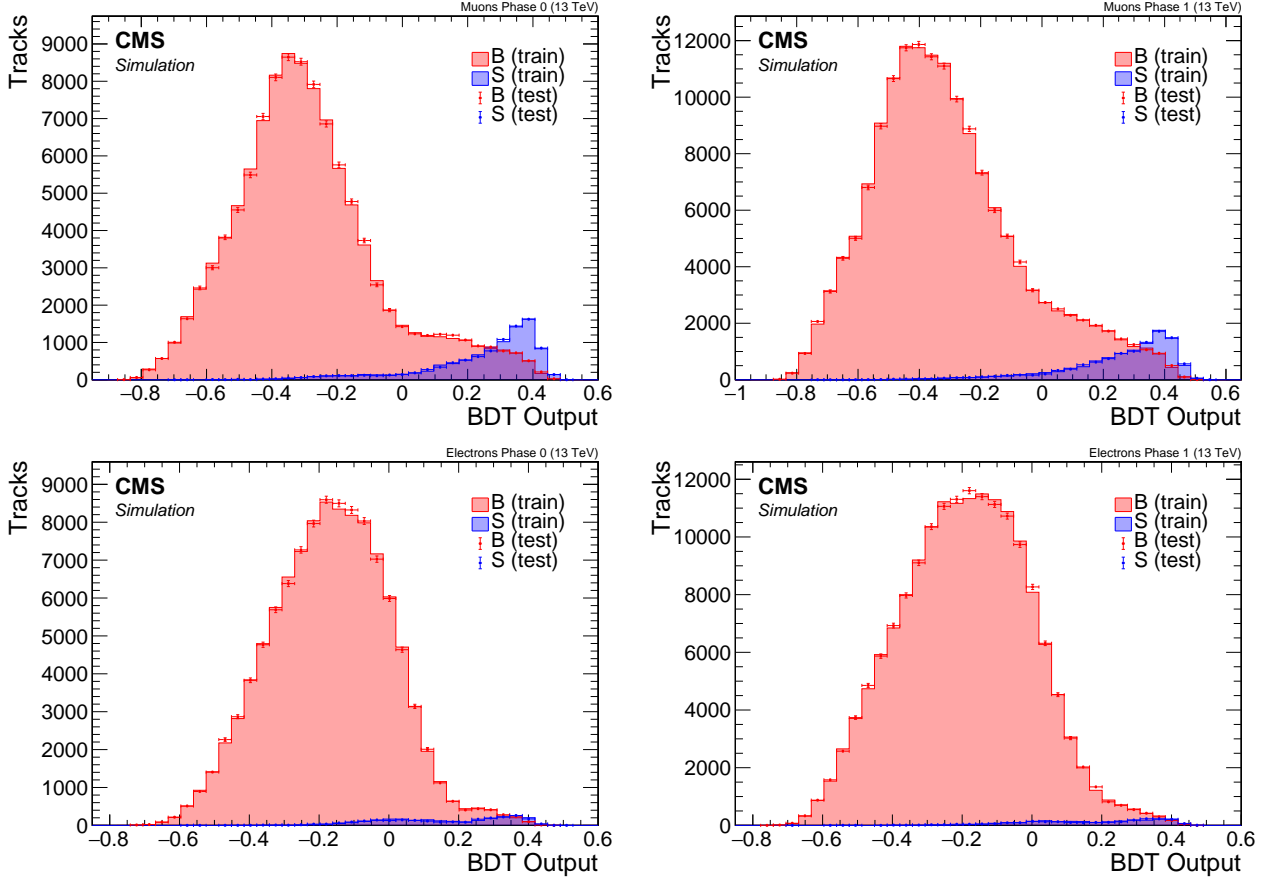


Figure 7.33: Track BDT output plots for Muons (top) and Electrons (bottom) in phase 0 (left) and phase 1 (right). Blue shows signal tracks, while Red are fake tracks. Test sample overlay on top of training sample.

After the training process, the track with the maximum BDT score is selected as the missing lepton in the event. Only events with a track with a score greater than 0.0, corresponding to the red dot in the ROC curves shown in Figure 7.34, are considered.

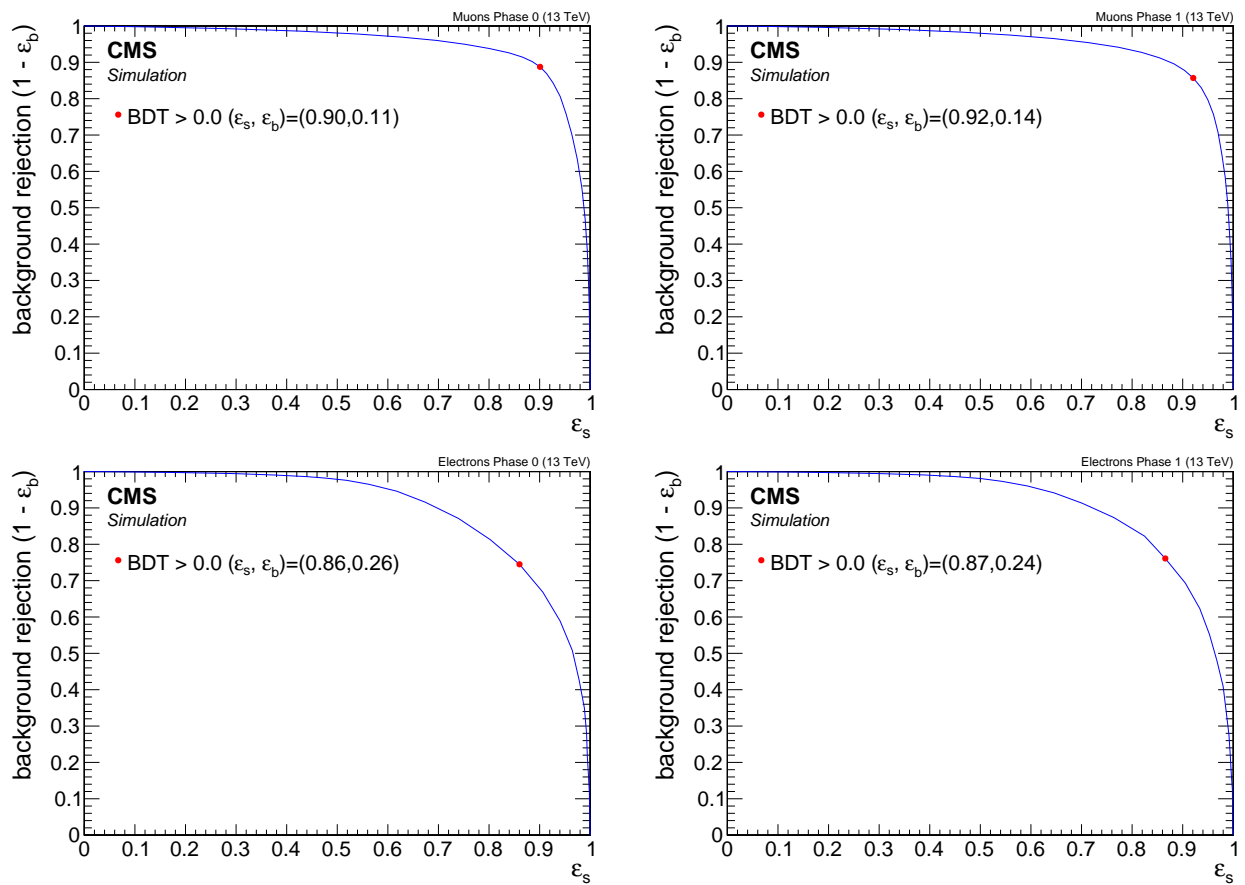


Figure 7.34: Track BDT ROC curves for Muons (top) and Electrons (bottom) in phase 0 (left) and phase 1 (right). Minimum working point showed as a red dot.

7.7.7 Isolation

The leptons produced from the neutralino decay $\tilde{\chi}_2^0 \rightarrow \tilde{\chi}_1^0 \ell^+ \ell^-$ are typically clean and isolated, with very little hadronic activity around them. This is because the only jets in the event come from initial state radiation, which provides a boost to the produced electroweakinos in the opposite direction. Therefore, the leptons originating from those electroweakinos will not exist in proximity to these jets. This signature can be exploited to discriminate between signal and background originating from standard model processes in association with jets. At CMS, various standard isolation criteria were developed and used. The three most widely used isolation criteria are track isolation [9], relative isolation (RelIso), which was first described in [10], and a modified version referred to as relative mini-isolation (miniRelIso), described in [11].

Track isolation is defined as the p_T sum of all tracks around a given track (or lepton) in a fixed cone size of 0.3:

$$\text{Track Isolation}_\ell = \frac{\sum_{\substack{\text{tracks from PV} \\ \text{in } \Delta R < 0.3}} p_T}{p_T(\ell)} \quad (7.7)$$

Since only tracks are summed, only charged particles are taken into account. Another widely used isolation is the relative isolation which uses a cone size of 0.4 and defined as:

$$\text{RelIso}_\ell = \frac{\sum_{\substack{\text{charged} \\ \text{hadrons} \\ \text{from PV}}} p_T + \max \left(0, \sum_{\substack{\text{neutral} \\ \text{hadrons}}} E_T + \sum_{\text{photons}} E_T - 0.5 \cdot \sum_{\substack{\text{charged} \\ \text{hadrons} \\ \text{from PU}}} p_T \right)}{p_T(\ell)} \quad (7.8)$$

The last term in the definition is a correction for PU effects. A lepton is considered to have passed isolation if its RelIso value is small. The third commonly used isolation criterion is the mini-relative isolation (miniRelIso), which is a modified version of relative isolation. In mini-isolation, the cone size is dependent on the p_T of the lepton, as follows:

$$R = \begin{cases} 0.2 & p_T(\ell) \leq 50 \text{ GeV} \\ \frac{10 \text{ GeV}}{p_T(\ell)} & p_T(\ell) \in (50 \text{ GeV}, 200 \text{ GeV}) \\ 0.05 & p_T(\ell) \geq 200 \text{ GeV} \end{cases} \quad (7.9)$$

The variable size cone allows for the recovery of efficiency when leptons are produced in the decay chain of a boosted object. In such cases, when the boost is large, the lepton is likely to overlap with a jet produced in the same decay chain, failing a standard isolation cut.

The drawback of standard isolation criteria is that if two leptons are in proximity to each other, as is often the case in the signal, they compromise each other's isolation. As shown in Section 7.5.4.3, access to low Δm model-points requires including the $\Delta R < 0.3$ phase-space region. Requiring any of the standard isolation criteria will thus result in rejecting valuable signal events. An alternative isolation criterion is proposed to help retain some of the desired phase-space while rejecting the majority of the standard model background. Another crucial use for an alternative isolation criterion is background estimation, as described in Section 7.10.2.1. The steps to construct the alternative *jet isolation* are described below. It is defined for each lepton flavor individually, since the produced leptons are of the same flavor. The steps are as follows (introducing parameters p and r):

1. Create a copy set of the jets collection

2. Create a *lepton-corrected* set of the jets by subtracting all leptons within the jet cone of 0.4
3. Clean the set of jets by keeping only jets with positive energy and p_T greater than threshold p
4. Lepton is said to pass *jet-isolation* if it does not lie within a cone of size r from a *lepton-corrected* jet
5. Lepton is said to fail *jet-isolation* for background estimation if it fails *jet-isolation*, and the original jet closest to it has $15 < p_T < 30 \text{ GeV}$ (see 7.10.2.1 for use of such lepton)

The main idea behind defining jet-isolation is to reject leptons with hadronic activity around them while not losing a lepton that is close to another lepton of the same flavor. The process described introduces two free parameters: the p_T threshold of the lepton-corrected jets that cause a lepton's isolation to fail (p), and the cone size (r), which determines how close a corrected jet is allowed to be to a lepton. To choose the thresholds for these parameters, a scan has been performed ranging $p \in [0, 20] \text{ GeV}$ and $r \in [0.4, 0.6]$. The scan is used to compare different criteria for the optimal values. Since the isolation is also used for background estimation, some of the criteria of interest stem from that method. The criteria of interest include signal efficiency (which should be high), background efficiency (which should be low), signal contamination in control-regions (ideally low), jetty-background transfer factor (ideally less than 1), and lastly, the significance, which is computed taking into account transfer factor error on the background (which should be maximized). To demonstrate the effect that this parameter space has on these criteria, a scan was done for the muons using 2016 MC and data.

Table 7.5: Signal Efficiency

		ΔR				
		0.4	0.45	0.5	0.55	0.6
p_T	0	0.38	0.37	0.36	0.35	0.35
	1	0.39	0.38	0.37	0.37	0.36
	5	0.65	0.64	0.63	0.62	0.60
	6	0.71	0.70	0.69	0.67	0.66
	7	0.77	0.76	0.74	0.73	0.72
	8	0.82	0.82	0.80	0.78	0.77
	9	0.87	0.86	0.85	0.84	0.82
	10	0.89	0.89	0.87	0.86	0.85
	10.5	0.90	0.90	0.89	0.88	0.87
	11	0.92	0.92	0.91	0.90	0.89
	11.5	0.93	0.92	0.91	0.91	0.90
	12	0.94	0.93	0.92	0.91	0.90
	12.5	0.94	0.94	0.93	0.92	0.91
	13	0.95	0.95	0.94	0.93	0.93
	15	0.98	0.98	0.97	0.97	0.97
	20	1.00	1.00	1.00	0.99	0.99

From the scan, it is evident that the transfer factor of the jetty background estimation method increases with larger p_T but decreases with larger ΔR . A transfer factor that is less than unity is preferred, and therefore, choices that do not meet this criteria are excluded. After taking into account all factors, the vaules $(p, r) = (10 \text{ GeV}, 0.6)$ are selected for muons and $(p, r) = (10 \text{ GeV}, 0.5)$ for electrons.

Table 7.6: Background Efficiency

	ΔR				
	0.4	0.45	0.5	0.55	0.6
p_T	0	0.08	0.07	0.06	0.06
	1	0.08	0.07	0.06	0.06
	5	0.12	0.12	0.10	0.09
	6	0.15	0.14	0.12	0.11
	7	0.18	0.16	0.15	0.14
	8	0.20	0.18	0.17	0.17
	9	0.25	0.23	0.19	0.18
	10	0.26	0.25	0.22	0.19
	10.5	0.27	0.24	0.23	0.20
	11	0.29	0.26	0.24	0.22
	11.5	0.28	0.27	0.24	0.23
	12	0.29	0.27	0.26	0.24
	12.5	0.31	0.28	0.26	0.26
	13	0.33	0.29	0.27	0.27
	15	0.36	0.33	0.30	0.29
	20	0.45	0.41	0.39	0.36

Table 7.7: Transfer Factor

	ΔR				
	0.4	0.45	0.5	0.55	0.6
p_T	0	0.19	0.16	0.13	0.13
	1	0.18	0.16	0.14	0.13
	5	0.31	0.30	0.26	0.23
	6	0.43	0.36	0.32	0.30
	7	0.55	0.48	0.44	0.40
	8	0.68	0.58	0.52	0.52
	9	0.83	0.78	0.65	0.58
	10	0.99	0.93	0.76	0.67
	10.5	1.07	0.95	0.85	0.74
	11	1.19	1.10	0.93	0.85
	11.5	1.24	1.19	0.96	0.91
	12	1.34	1.29	1.09	0.99
	12.5	1.55	1.35	1.21	1.10
	13	1.70	1.46	1.27	1.23
	15	2.39	2.17	1.80	1.63
	20	6.12	5.86	4.82	4.13

Table 7.8: Significance $s/\sqrt{b + \epsilon_b^2}$

p_T	ΔR				
	0.4	0.45	0.5	0.55	0.6
0	4.29	6.08	6.13	5.89	5.46
1	4.92	5.18	6.34	5.33	5.84
5	6.44	5.27	6.20	8.63	5.98
6	4.72	5.06	6.22	6.99	7.92
7	4.83	6.55	5.09	5.63	6.28
8	3.80	5.48	4.60	5.24	4.61
9	3.60	4.43	5.66	6.25	4.60
10	3.37	4.08	5.57	4.78	6.23
10.5	3.72	4.03	4.90	4.48	4.17
11	3.05	3.51	4.37	4.98	5.41
11.5	3.21	3.21	3.84	3.54	4.65
12	3.48	3.51	3.80	3.30	3.54
12.5	2.79	3.19	2.82	3.36	4.60
13	3.16	2.68	3.59	6.60	3.50
15	4.46	3.19	3.06	3.64	3.85
20	7.21	1.46	1.60	8.10	2.09

7.8 Trigger

7.9 Event selection

In the following section we detail the event level selection applied in this analysis. We have seen in 7.4 that we refer to three categories in this analysis: dimuon category, and exclusive track category for each lepton flavor. We summarise the preselection in 7.9.1, then the selection that defines each category in 7.9.2, and finally the multivariate selection for each category in 7.9.3.

7.9.1 Baseline selection

We have reviewed some of the base selection that is common to all categories in 7.5.3. We reiterate reasons for these selections here in addition to other event level selections.

- $H_T^{\text{miss}} \geq 220 \text{ GeV}$ and $E_T^{\text{miss}} \geq 140 \text{ GeV}$ cuts intend to boost sensitivity by rejecting SM background, as well as to operate in the acceptance regime of the MET trigger, as described in 7.8. It is especially efficient in rejecting QCD background, since it does not produce real E_T^{miss} . Any E_T^{miss} apparent in QCD is due to jet energy miss measurements. The reason we are cutting harder on H_T^{miss} rather than E_T^{miss} is that H_T^{miss} sums jets with $p_T > 30 \text{ GeV}$ and is blind to objects with $p_T < 30 \text{ GeV}$. Since we rely in our background estimation on jets with p_T in the range of $[15, 30] \text{ GeV}$, H_T^{miss} is more appropriate than E_T^{miss} since it does not introduce a bias in the data-driven background estimation methods. The two observables are highly correlated though, and describe similar physics.
- $N_{\text{jets}}(p_T \geq 30 \text{ GeV} \text{ and } |\eta| < 2.4) \geq 1$. We are requiring at least one jet in the event, since such an ISR jet gives a boost to the produced neutralino, thus increasing the missing transverse energy and with it the sensitivity.
- $N_{\text{b-jets}}(p_T \geq 30 \text{ GeV} \text{ and } |\eta| < 2.4) = 0$. We are vetoing any b-tagged jet. Our signal does not contain real b-tagged jets. This veto is efficient in rejecting background from $t\bar{t}$, in which the b quarks arise from a t quark decay.
- $\min \Delta\phi(H_T^{\text{miss}}, \text{jets}) > 0.4$. Since we are requiring an ISR jet in the event, we expect the H_T^{miss} to point in the opposite direction of the jet, or at least in an angle close to π . Events with multiple jets in the SM background such as arising from QCD will not exhibit such a feature. Therefore this cut reduces QCD background.
- veto events with isolated loose-ID lepton having $p_T \geq 30 \text{ GeV}$. Lepton can be either muon or electron. Our signal does not have high- p_T leptons, as we have seen in 7.5.
- $0.4 < m_{\ell\ell} < 12 \text{ GeV}$. Our signal resides in an invariant mass window with an edge at the mass difference between $\tilde{\chi}_2^0$ and $\tilde{\chi}_1^0$. This is a relatively loose cut that is expected to further be tightened by the boosted decision tree.

We have already seen the object level selection in 7.7. For the sake of completeness we reiterate them here. The electrons in the analysis require to pass the following selection (see also 7.7.1):

- $5 \leq p_T \leq 15 \text{ GeV}$
- $|\eta| < 2.5$
- pass jet isolation

- loose ID

The muons in the analysis require to pass the following selection (see also 7.7.2):

- $2 \leq p_T \leq 15 \text{ GeV}$
- $|\eta| < 2.4$
- pass jet isolation
- medium ID

7.9.2 Category selection

The analysis has two main categories: dilepton and exclusive track category. The dilepton category has two leptons, while the exclusive track category has a single lepton and a track that has not been identified as a lepton. The dilepton category includes only one flavor, namely muons, while the exclusive track category has both electrons and muons flavored leptons. Selection for the dilepton category is listed in 7.9.2.1 and for the exclusive track category in 7.9.2.2.

7.9.2.1 Dilepton selection

In the dilepton category we have two reconstructed and identified muons. The following lists the selections:

- $N_\mu = 2$ opposite charge passing the muons selection.
- $p_T(\mu_2) \leq 3.5 \text{ GeV}$ or $\Delta R(\mu_1, \mu_2) < 0.3$. This requirement makes this analysis orthogonal to the SOS analysis [1].
- event level BDT cut of $\text{BDT} > 0$. This is the main method of selecting signal events while rejecting the SM background. See 7.9.3 for details.
- $\Delta R(\mu_{1,2}, \text{leading jet}) > 0.4$. The leptons should not be inside the ISR jet.
- ω, ρ^0 and J/ψ invariant mass vetoes. $m_{\ell\ell} \notin [0.75, 0.81] \text{ GeV}$, $m_{\ell\ell} \notin [3, 3.2] \text{ GeV}$.

7.9.2.2 Exclusive track selection

In the exclusive track category we have one reconstructed and identified lepton (either an electron or a muon) and an exclusive track, i.e., a track that does not match an identified lepton. The track in the event that is picked to act as the misidentified lepton is the one with the maximum score of the track BDT 7.7.6. The following lists the selections:

- $N_\ell = 1$ lepton passing the muons selection.
- track picking BDT cut of $\text{BDT} > 0$. See 7.7.6.
- event level BDT cut of $\text{BDT} > 0$. This is the main method of selecting signal events while rejecting the SM background. See 7.9.3 for details.
- $\Delta R(\ell, \text{leading jet}) > 0.4$. The lepton should not be inside the ISR jet.

7.9.3 Boosted decision trees

In order to reject Standard Model (SM) background, pick signal events and define Signal Regions (SRs), in this analysis we employ multivariate method of type Boosted Decision Tree (BDT). For the dimuon category we train one BDT. For the exclusive track category we train a BDT for each lepton flavor and also for the two phases of the tracker detector, i.e., phase 0 and phase 1. That makes five BDTs overall.

All BDTs use the same structure of 120 trees with a maximum depth of 3, with the TMVA package [8]. The BDT training is performed with AdaBoost and GiniIndex separation. We are taking all other values as the defaults set by the TMVA package.

For the training we take tracks from a pool of our privately produced FASTSIM signal simulations which were listed in 7.6.2 for the signal, and the standard model background simulation listen in 7.6.1 for the background. For the exclusive track category, since we train for the different phases of the tracker detector, we use 2016 simulations of the signal and standard model background to represent phase 0, and the 2017 ones to represent phase 1. For the dimuon category we use only 2017 simulations to represent both phases with an added systematic uncertainty that results from this choice.

For the pool of our privately produced FASTSIM signal simulations, we are selecting the full range of simulated higgsino parameter μ (or the mass of $\tilde{\chi}_1^\pm$ in case of phase 1), but only the range of Δm we want to be most sensitive to. In phase 0, we select $\Delta m^0 \in [0.3, 4.3] \text{ GeV}$ and $\mu \in [100 - 130] \text{ GeV}$. In phase 1 we select $\Delta m^\pm \in [0.3 - 4.6] \text{ GeV}$ and $\mu \in [100 - 500] \text{ GeV}$. The baseline selection listen in 7.9.1 has been applied. A subset of the selections listed in 7.9.2.1 and 7.9.2.2 is used for the training:

- $N_\mu = 2(1)$ opposite charge passing the muons selection for the dimuon category (for the exclusive track category).
- $\Delta R(\ell, \text{leading jet}) > 0.4$.
- track picking BDT cut of BDT > 0 for the exclusive track category.

The training has been done without using MC weights, since we found that it gives the result with the least amount of over training that arise due to high weighted MC events. The training results in satisfactory performance since the kinematics of the low- p_T leptons is expected to look similar in all SM background processes. In the following sections, this fact needs to be taken into account when we look at the training input variables distributions. These distributions are plotted as they are seen by the training algorithm, i.e., without MC weights and with signal events taken from a pool of different parameter values as described above. Therefore, the ROC curves cannot be understood as a simple signal efficiency versus background rejection. Every BDT output working point results in different signal efficiency depending on the signal parameters values. As we will see later on, we do not use one BDT value with a simple cut and count, but rather we are binning the SRs in BDT output values. We therefore choose to plot the ROC curve with a default cut of 0.0 for the sake completeness. To fully estimate the power of the training, we need to look at the significance when each signal point has been properly weighted together with the SM background processes.

7.9.3.1 Dimuon category

The training samples for the dimuons category contain 4350 signal events and 21842 background events. The training samples are then tested against the test samples of equal size. The distributions of the testing samples overlay on the training samples, as well as the ROC curve, are seen in 7.35. No significant over training is observed.

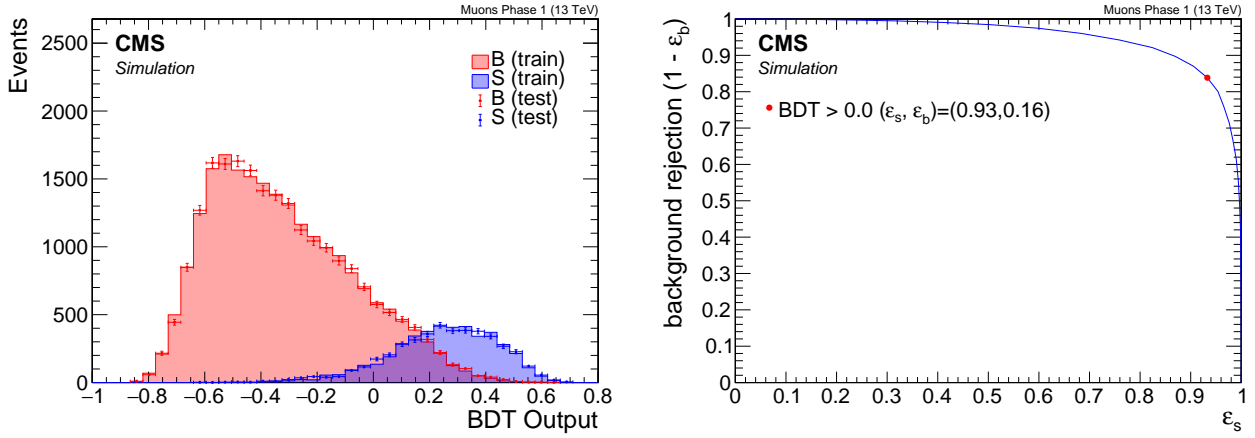


Figure 7.35: Dimuon BDT output (left) and ROC curve (right).

The training uses 18 different variable listed in 7.9.3.1 in decreasing order of importance ranking.

Table 7.9: Dimuon BDT input variables

Rank	Variable	Description
1	$m_{\ell\ell}$	invariant mass
2	$p_T(\ell_1)$	leading lepton p_T
3	H_T^{miss}	
4	H_T	
5	$\Delta R(\ell\ell)$	
6	$\min \Delta\phi(H_T^{\text{miss}}, \text{jets})$	
7	$p_T(\vec{\ell}_1 + \vec{\ell}_2)$	dilepton p_T
8	$p_T(\text{leading jet})$	
9	$p_T(\ell_2)$	subleading lepton p_T
10	$\eta(\ell_1)$	leading lepton η
11	$m_T(\ell_1)$	leading lepton transverse mass
12	$ \Delta\phi(\ell_2, \vec{H}_T^{\text{miss}}) $	
13	$ \Delta\phi(\ell_1, \vec{H}_T^{\text{miss}}) $	
14	$ \Delta\phi(\ell\ell) $	
15	N_{jets}	Number of jets
16	$\eta(\text{leading jet})$	
17	$ \Delta\eta(\ell\ell) $	
18	$m_{\tau\tau}$	collinear approximation of $m_{\tau\tau}$

Distributions of the input variables to the BDT training can be seen in 7.36. As mentioned before, the signal is taken from a pool of a range of model points, and events are not weighted to any luminosity or cross section in order to avoid over training.

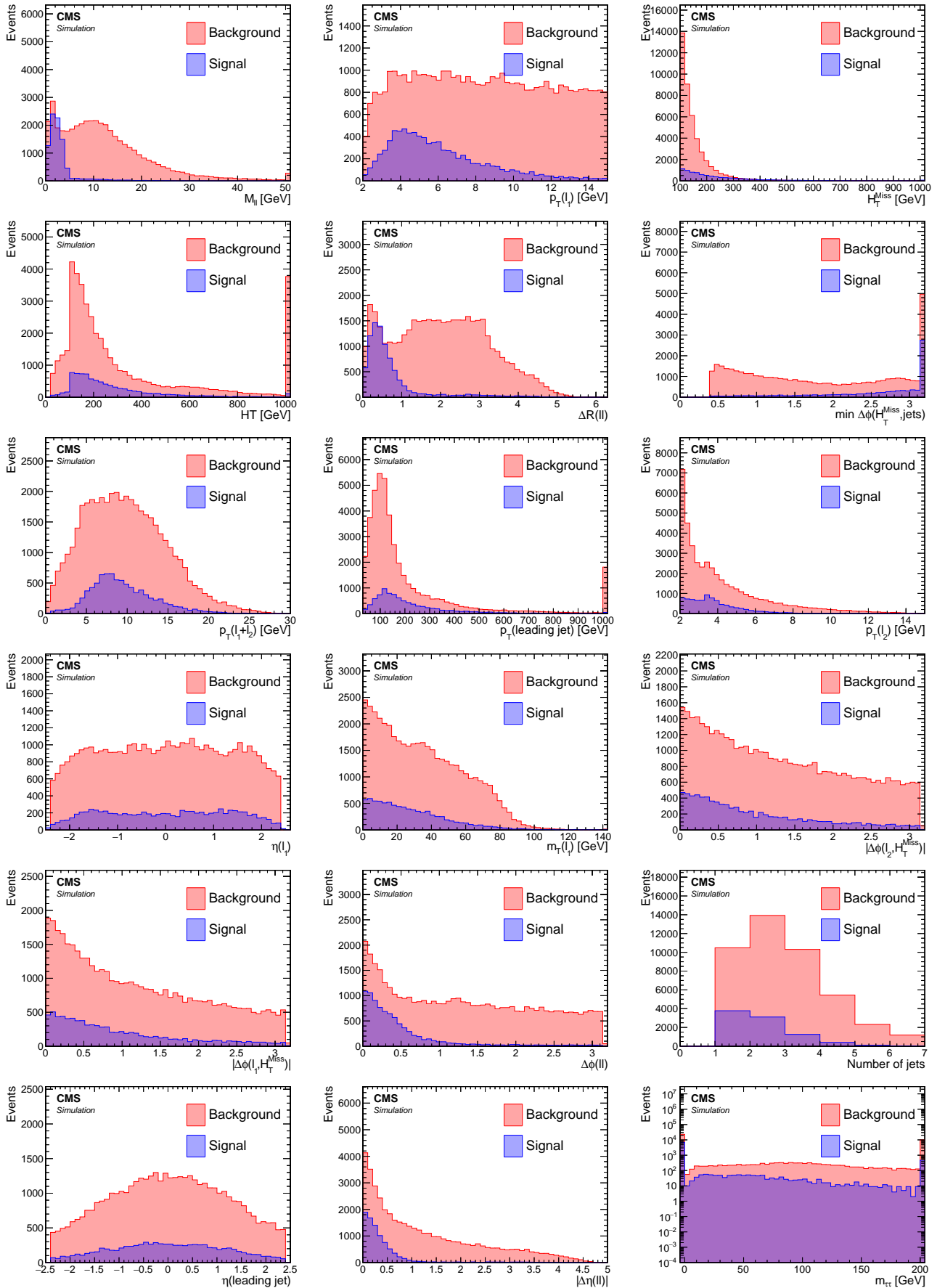


Figure 7.36: Dimuon BDT training input variables. Ordered by importance ranking.

7.9.3.2 Exclusive track category

The training samples in phase 0 for the exclusive category contain 7863 (1750) signal events and 55765 (29135) background events for muons (electrons) flavor. For phase 1, the exclusive category contain 5266 (1332) signal events and 51308 (31149) background events for muons (electrons) flavor. The training samples are then tested against the test samples of equal size. The distributions of the testing samples overlay on the training samples are seen in 7.37. No significant over training is observed. The ROC curves are seen in 7.38.

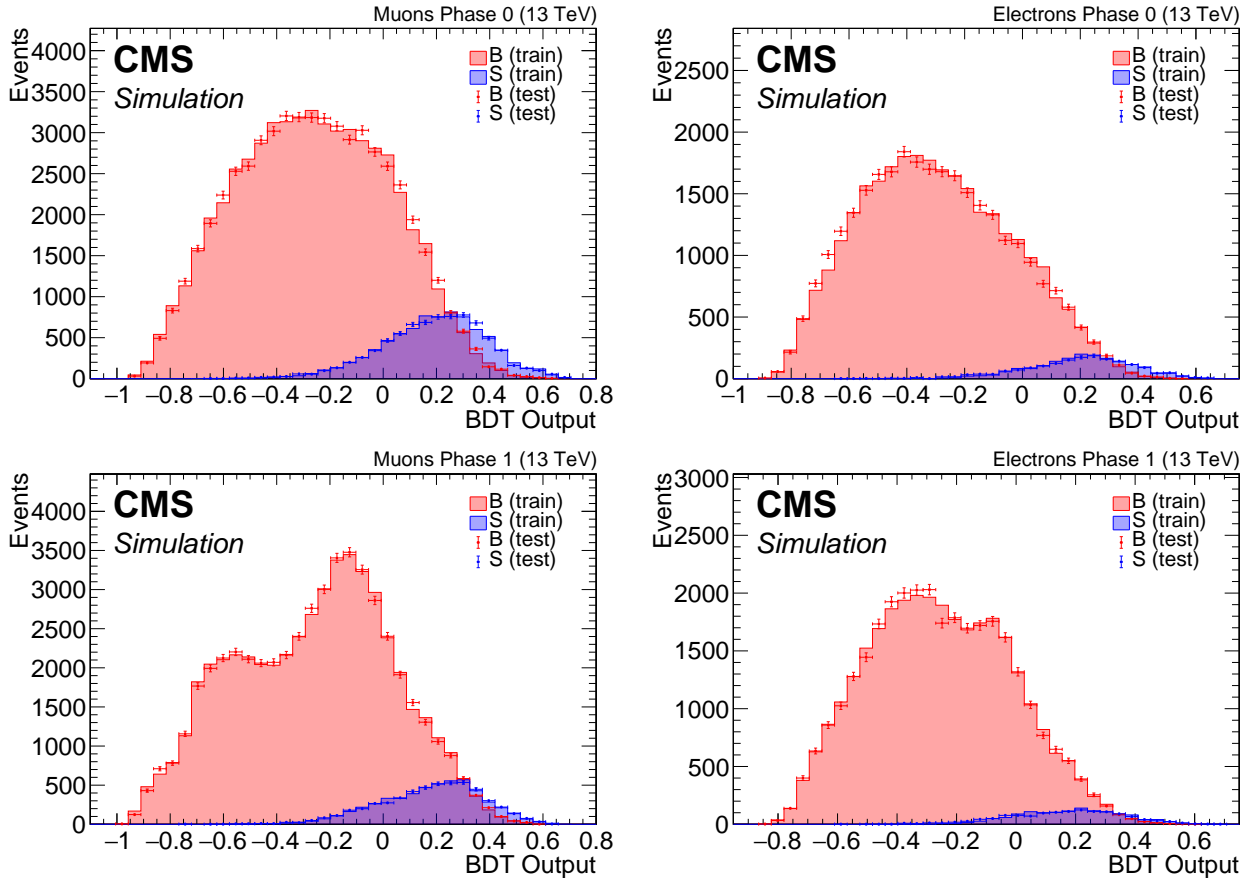


Figure 7.37: Exclusive track category BDT output in phase 0 (top) and phase 1 (bottom) for muons (left) and electrons (right)

The training uses 18 different variables listed in Table 7.9.3.2 in decreasing order of importance ranking. Since the ranking is slightly different in the four trainings, we choose here to list the order in the case of the muons of phase 1. We denote the fully identified lepton as ℓ and the non-identified lepton track as t .

Distributions of the input variables to the BDT training can be seen in 7.39. As mentioned before, the signal is taken from a pool of a range of model points, and events are not weighted to any luminosity or cross section in order to avoid over training. In the following sections we will look at fully weighted distributions in order to asses the performance of the training for different model points and to understand the different components of the standard model background and how to estimate it properly.

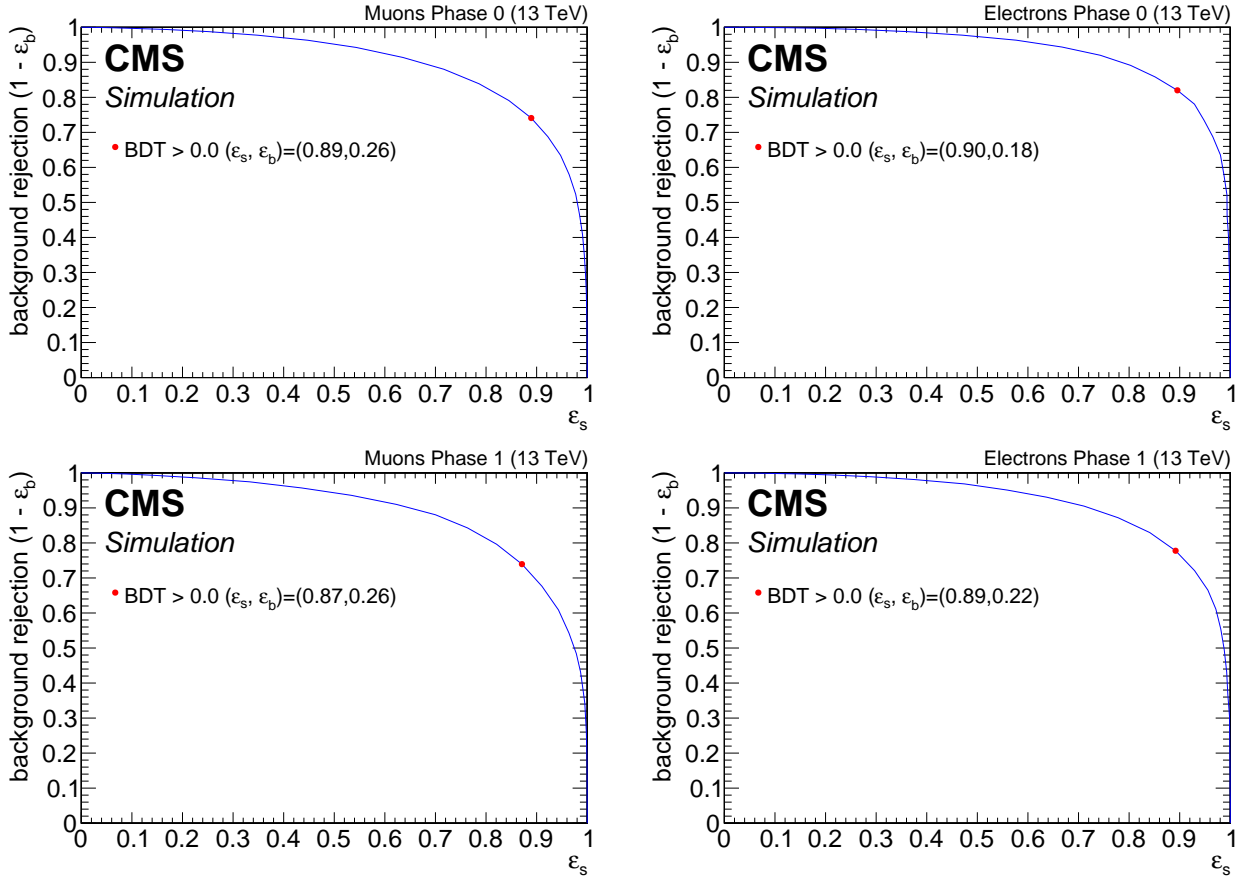


Figure 7.38: Exclusive track category ROC curves in phase 0 (top) and phase 1 (bottom) for muons (left) and electrons (right)

Table 7.10: Exclusive track BDT input variables

Rank	Variable	Description
1	$p_T(\ell)$	lepton p_T
2	H_T^{miss}	
3	H_T^{miss}	
4	$\min \Delta\phi(H_T^{\text{miss}}, \text{jets})$	
5	$p_T(\text{leading jet})$	
6	N_{jets}	Number of jets
7	track BDT output	
8	$\eta(t)$	
9	$p_T(t)$	track p_T
10	$\eta(\text{leading jet})$	
11	$m_{\ell\ell}$	invariant mass
12	$\eta(\ell)$	
13	$m_T(\ell)$	lepton transverse mass
14	$\Delta R(\ell, t)$	
15	$\phi(\ell)$	
16	$\phi(t)$	
17	$ \Delta\phi(\ell, t) $	
18	$ \Delta\eta(\ell, t) $	

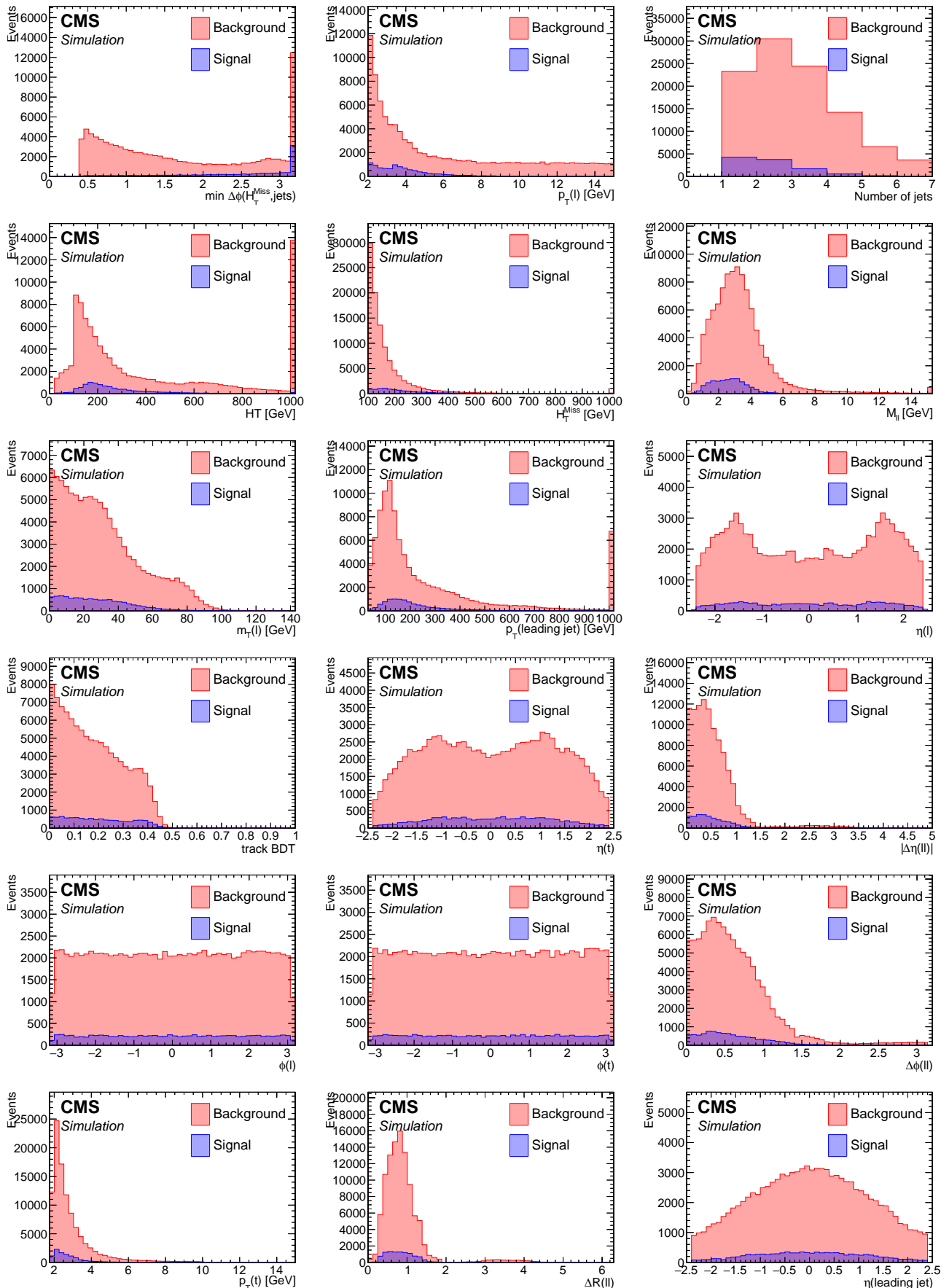


Figure 7.39: Exclusive track BDT training input variables. Ordered by importance ranking.

7.10 Characterization and estimation of the Standard Model backgrounds

In order to have a solid analysis strategy, the Standard Model (SM) background has to be thoroughly studied and estimated. It is important to fully understand the characteristics and composition of the SM background both in order to maximally reject it in the Signal Regions (SRs), as well as constructing a good method for estimating it. The characterization of the SM backgrounds is examined in 7.10.1, and estimation of the backgrounds is explored in 7.10.2.

7.10.1 Characterization of the Standard Model backgrounds

Signal Regions (SRs) are defined by a set of cuts or selections on observables composed of detector readings. Equivalently, multivariate techniques can be used in order to cut on a single aggregated output observable devised from a set of input variables, as was done in this analysis. No matter how a SR is defined, usually not only signal processes will be measured, but also processes that are not the intentions of the analysis. These processes are referred to as background to the analysis. Background processes can arise due to truly similar final state physics, or due to detector effects and mismeasurements. In an analysis such as the current one, an example for background in the dimuon category which arises from truly similar physics is Drell-Yan. In a Drell-Yan process, opposite-charge same-flavor dilepton pair are produced from an off shell Z^* or γ^* . An example of a background process that is due to mismeasurement is the production of a W in association with jets, which decays leptonically, and another lepton is due to either mismeasurement, i.e., a fake lepton, or as part of a hadronization procedure. A full list of the SM processes that are taken into account in this analysis with descriptions is given below. The processes are ordered according to their contribution in the SRs of the dimuon category.

- **W in association with jets.** In this SM process, we have a production of a W boson alongside jets, decaying leptonically into a lepton and a neutrino. It can be written schematically as $W + \text{jets} \rightarrow \ell\nu$. There are several reasons why this process is a background to this analysis. Since there's a neutrino produced in this process, it contributes to some real missing transverse momentum being produced. The presence of jets means that it is highly likely to pass the selection of at least one jet in the event. Energy mismeasurement of the jets can also contribute to the presence of fake missing transverse momentum, i.e., E_T^{miss} due to mismeasurements rather than real physics. Lastly, the very loose transverse momentum p_T range of the analysis muons means that it is also highly likely to pick an additional lepton in the event. In the exclusive track category, the extra track is mostly a fake lepton, i.e., a track that was misidentified by the BDT selection as the second lepton. In the dimuon category it is either a fake misidentified lepton, or a low- p_T lepton originating from a decay chain in a hadronization process.
- **Z in association with jets.** In this SM process, we have a production of a Z boson alongside jets, decaying into two neutrinos. It can be written schematically as $Z + \text{jets} \rightarrow \nu\bar{\nu}$. The two neutrinos in this process contribute to true missing transverse momentum in the event. The two leptons will then come from either a decay of a meson produced in the hadronization procedure, or from unrelated decays. Another highly likely scenario is for one of the leptons to be fake, just like in the $W + \text{jets} \rightarrow \ell\nu$ case.
- **Drell-Yan process.** It takes place when a quark of one proton and an antiquark of another proton annihilate, creating a virtual photon or Z^* boson which then decays into a pair of oppositely-charged leptons. When two electrons are produced via $Z \rightarrow e^+e^-$ or two

muons via $Z \rightarrow \mu^+ \mu^-$, true missing transverse momentum is not part of the production. Therefore, a relatively high E_T^{miss} cut such as in this analysis is successful in suppressing these types of backgrounds. However, in the production of two taus via $Z/\gamma^* \rightarrow \tau^-\tau^+$, each tau can then decay into a muon alongside two neutrinos, i.e., $\tau \rightarrow \mu \bar{\nu}_\mu \nu_\tau$, producing real missing transverse momentum in the event alongside two real leptons, which become a background to this analysis.

- **Ditop in association with jets.** When two top quarks are produced, $t\bar{t}$, most of the time they will decay into a W and a b quark. That happens close to 100% of the time. Therefore, $t\bar{t}$ becomes a background when each top quark decays into a b quark and a leptonically decaying W boson. The W produces neutrinos in the decay alongside the leptons, contributing real missing transverse momentum. Vetoing b-tagged jets, as listed in 7.9.1, is successful in suppressing most of this background, but not all.
- **Numerous bosons production.** In the plots of the following section, we differentiate between diboson production, VV, and higher order production such as three bosons, which are referred to collectively as *rare*. The ways in which they can be selected in the SRs are similar to the single boson case, only that the higher multiplicity cases have much lower production cross sections, and therefore are almost negligible in this analysis.
- **QCD production.** Quantum Chromodynamics (QCD) comprises events arising from the production and radiation of quarks and gluons followed by their hadronization and showering into highly columnar sprays of particles known as jets. QCD events contain no real E_T^{miss} . Any E_T^{miss} present in a QCD event is due to mismeasurements. The relatively high E_T^{miss} cut in this analysis in combination with requiring $\min \Delta\phi(H_T^{\text{miss}}, \text{jets}) > 0.4$, reduce almost all QCD background, and is therefore a very negligible background in this analysis. That is the reason why it can be safely disregarded in most contexts and safely assumed that any remaining events will be successfully be estimated using the jetty-background data-driven background estimation method in 7.10.2.1.
- **Resonances.** Resonances are compound particles, namely, mesons or baryons, which can later decay into leptons. The highest contribution in this category comes from the J/ψ , since it has a mass of 3.1 GeV with a relatively high cross section. In order to reduce this background, ω , ρ^0 and J/ψ invariant mass vetoes are applied in the range of $m_{\ell\ell} \in [0.75, 0.81] \text{ GeV}$, $m_{\ell\ell} \in [3, 3.2] \text{ GeV}$.

The optimal way to gather an understanding of the proportion each background process has in the Signal Regions (SRs), is to look at correctly weighted MC simulation, where each process is weighted to its corresponding production cross section, and the overall background is weighted to match the era luminosity. It is useful to look at the final SRs defined and discussed in Section 7.12, but also at some of the important inputs to the BDT which were discussed in 7.9.3. In the following sections, it is useful to note that the SRs are all the bins with a BDT value greater than zero. Each of the following sections presents the figures relevant to the relevant analysis category, beginning with the BDT output distributions and SRs bins, following by important inputs to that BDT. Although input distributions have been seen already in section 7.9.3, here the background processes and individual signal models are properly weighted. The data-taking year of 2017 was chosen as a representative here.

7.10.1.1 Dimuon category

The dimuon 2017 simulation BDT output, weighted to 2017 luminosity, both in log and linear scales, can be seen in Figure 7.40. The SRs are the six bins with BDT output greater than zero in increasing sensitivity. As can be seen in the figure, the largest backgrounds are $t\bar{t}$, $Z + \text{jets} \rightarrow \nu\nu$ and $W + \text{jets} \rightarrow \ell\nu$. There is also a small presence of Drell-Yan processes, that are mainly due to $Z/\gamma^* \rightarrow \tau^-\tau^+$. The top ten input observables to the BDT, ranked by importance for the training, can be seen in Figure 7.42.

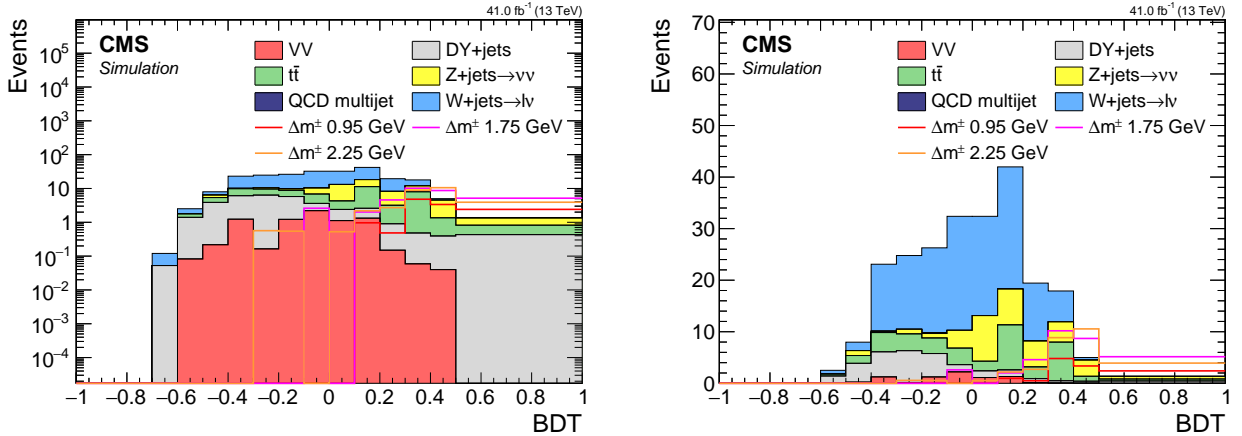


Figure 7.40: Dimuon 2017 simulation BDT output in log scale (left) and linear scale (right).

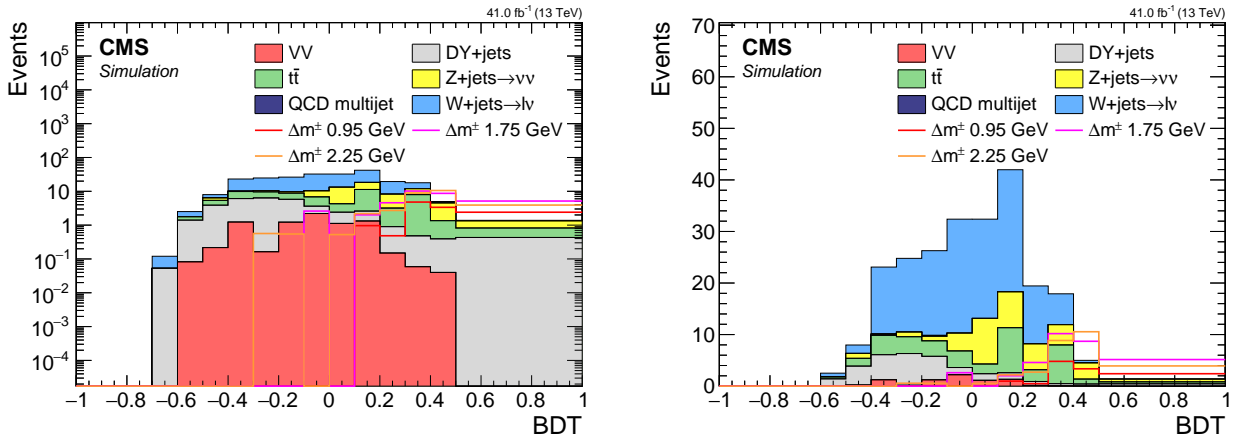


Figure 7.41: Dimuon 2017 simulation BDT output in log scale (left) and linear scale (right). Composition split into...

Fixme Note: Add jetty/tautau simulation plot

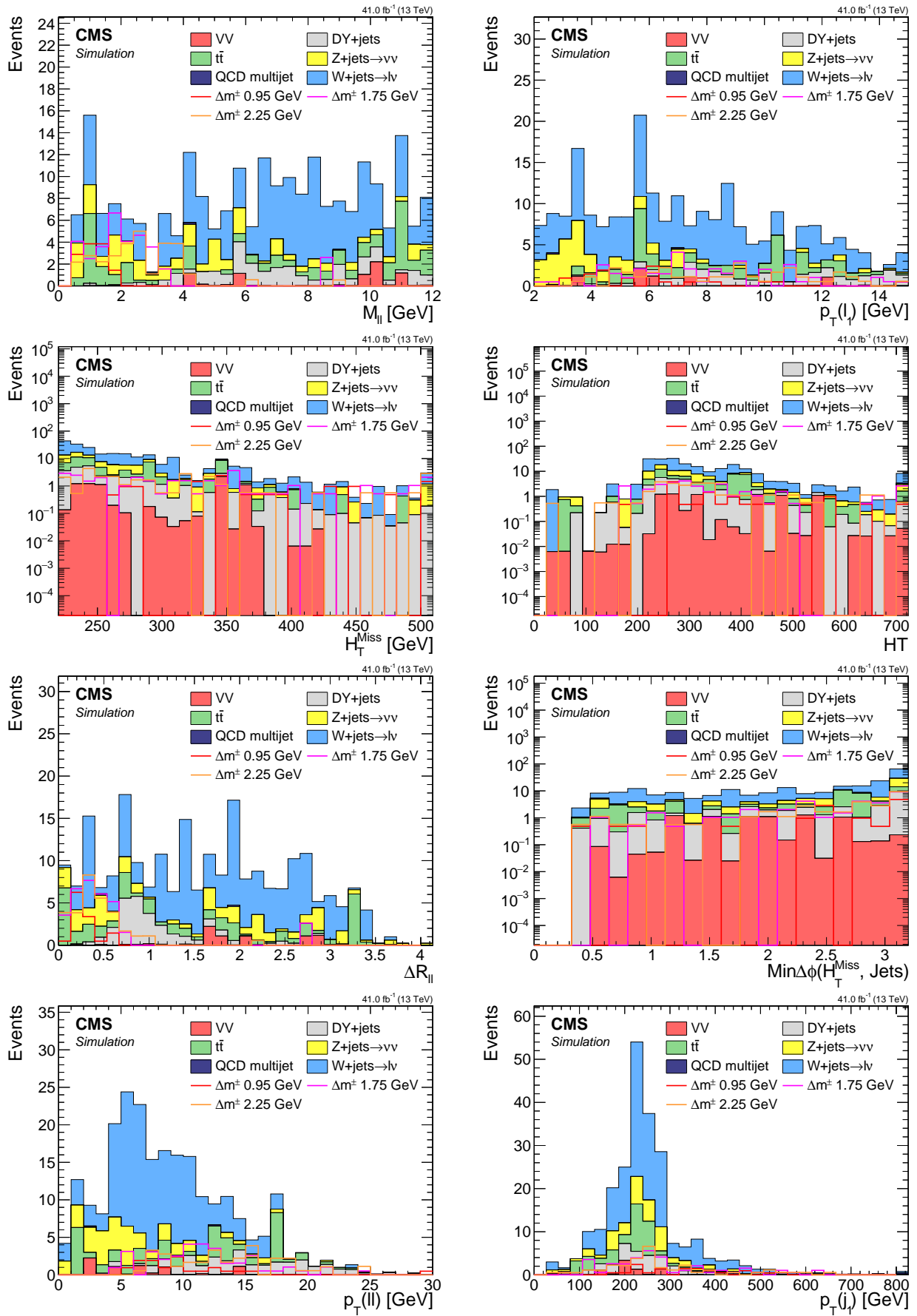


Figure 7.42: Dimuon 2017 simulation BDT inputs for the top 10 ranked observables.

7.10.1.2 Exclusive track category

As described before, there are four BDTs in the exclusive track category, for each of the two lepton flavors there are two track phases.

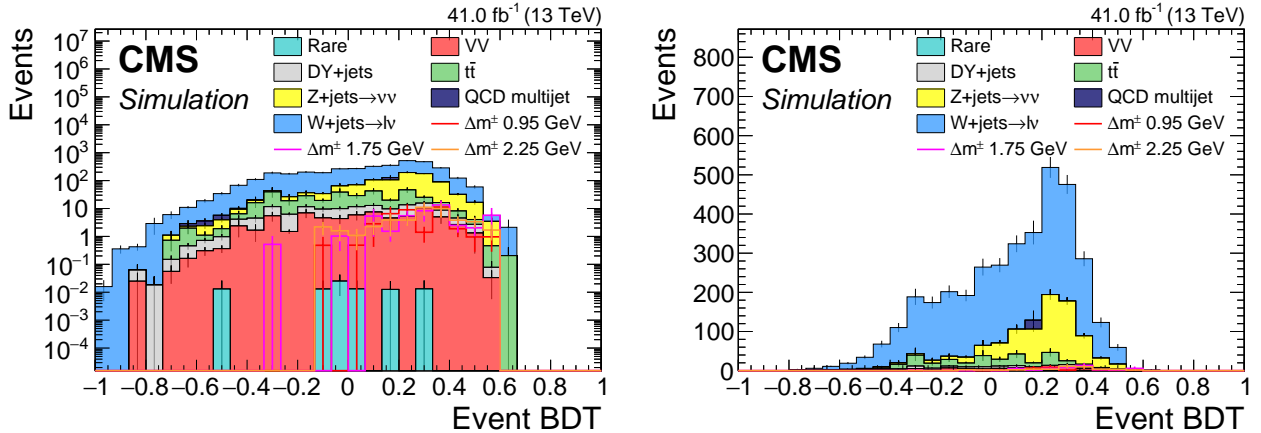


Figure 7.43: Exclusive track plus muon category 2017 simulation BDT output in log scale (left) and linear scale (right).

The muon flavor in phase 1 is chosen to represent background composition in the exclusive track category in order to avoid repetition, and can be seen in Figure 7.43. Figure 7.44 shows the top eight input observables to the BDT, ranked by importance for the training. It is weighted to 2017 luminosity and uses 2017 simulation. A few signal points are also plotted in order to point to the signal-like regions of phase space.

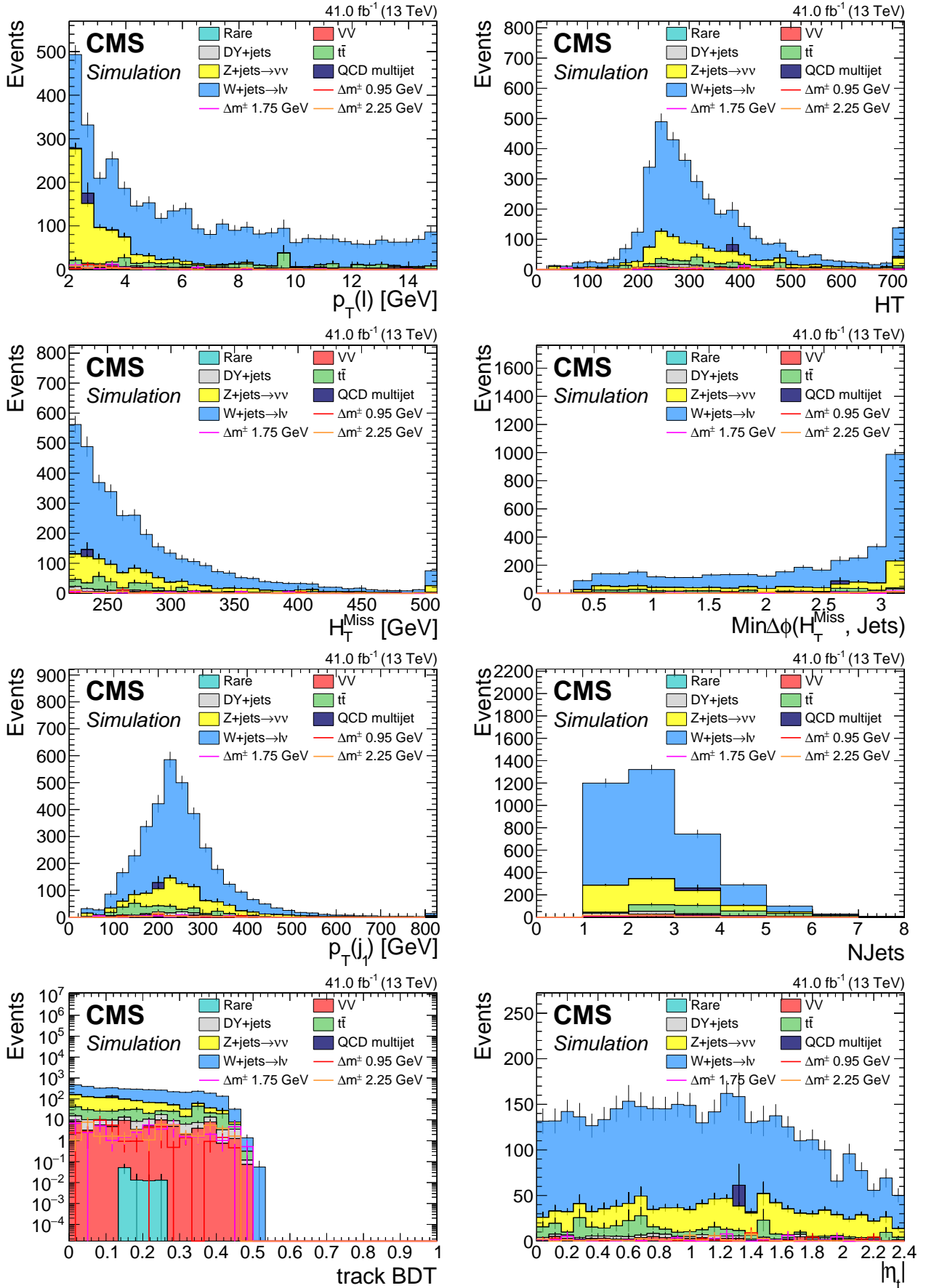


Figure 7.44: Exclusive track plus muon 2017 simulation BDT inputs for the top 8 ranked observables.

7.10.2 Estimation of the Standard Model backgrounds

In analyses such as the one described in this thesis, in which new physics, or physics beyond the Standard Model is searched for, one needs to predict event counts for the signal and for the Standard Model background. These counts are denoted s for the signal events count and b for the background events count. From these counts and their uncertainties, a *significance* is computed. The question that arises is how to predict such counts. A widely used method is Monte Carlo (MC) simulation, sometimes simply referred to as *simulation*. Prediction using simulation is pretty straight forward. First, many events are simulated using the SM technique, taking into account the detector's geometry (by such algorithms such as FASTSIM or FULL-SIM). They are then weighted to account for production cross sections and luminosity. Further correction factors and weights can apply to account for measurements errors, discrepancies between data and simulation, non-ideal algorithms, misidentifications, normalization corrections computed from data in a dedicated Control Region (CR), and so forth. The nominal prediction for the events count becomes then the fully-weighted simulation count in the relevant Signal Region (SR) with an uncertainty that is taken by the statistical error on the simulation count in that bin, with an optional systematic uncertainty that has been determined by other means. The signal count s has been determined in this way using FASTSIM. As is described in the following, only a small fraction of the background count b has been estimated using simulation. The majority of the background processes have been estimated using *data-driven methods*.

Using simulation to estimate the Standard Model background has limitations and disadvantages. These are specific to each analysis, in which the background processes composition change. The main limitation of simulation is that it is imperfect. Simulation never precisely simulates real data, and that is due to several factors. Theoretical uncertainties, such as uncertainties on cross sections or branching fractions, can lead to wrong production rate or normalization. That's why simulation is often reweighted using a normalization factor derived in a dedicated CR. Another challenging limitation of simulation is misrepresentation of the detector's delicate geometry and response, as well as real time data-taking challenges and faults which need to be taken into account in order for the simulation to accurately represent the events that would have been recorded by the detector. Some objects and phase-spaces are more prone to discrepancies than others.

In this analysis, a great deal of the challenge arises from the very *soft* nature of the leptons, i.e., their low transverse momentum p_T , as well as their low invariant mass of the order of a few GeV. Sources of backgrounds of such events in the standard model include low- p_T resonances that are produced in hadronization processes, and events where one of the leptons (or exclusive track) is misidentified as one of the signal leptons. These leptons or tracks are often in some vicinity of jets in the event. In this analysis, there are two strategies to estimating this sort of background depending on the whether we have two identified leptons, such as in the dimuon category, or one, such as in the exclusive track category. The dimuon *jetty background* estimation is described in Section 7.10.2.1, while the exclusive track background estimation is described in 7.10.2.3. Lastly, as described earlier, small part of the background is not produced nearby jets at all, namely $Z/\gamma^* \rightarrow \tau^- \tau^+$. That background estimation method is described in Section 7.10.2.2.

7.10.2.1 Non-isolated jetty background estimation

In the description of the object selection in Section 7.7, it has been demonstrated that the leptons in the signal are isolated. The isolation criterion that is used in this analysis has been described in 7.7.7, and is referred to as *jet-isolation*. It has been mentioned there that the customized isolation is also key part in the background estimation, and that is now described in this section. This background estimation method is relevant to the dimuon category. It is a *data-driven* background estimation method, meaning that we use data, rather than simulation, to estimate this background. The name *non-isolated jetty background* refer to background in which one or both of the leptons generally are produced in association with jets, and typically are close to one. Most of such leptons are rejected by the jet-isolation criteria, but some do manage to pass the isolation if they happen to have been produced far enough from a jet.

Our signal regions are defined in detail in Section 7.12, but here it is enough to note they are bins in the BDT output with a score greater than zero. The strategy of this method is to find a Control Region (CR) that produces a BDT output distribution that is shape-consistent with the original BDT distribution. That is achievable when a CR can be identified such that it has almost the same features as the main region, ideally only with rate difference. Then, to get normalization correctly, one would define a normalization control region to correct for the different production rate.

Interim note on terminology should be made for clarity. The SRs are defined by taking BDT output greater than zero, and therefore, by definition, the region with less than zero becomes a CR. Furthermore, a new region using isolation is being introduced in this section. Since the orthogonal region only varies from the main region by isolation, it is referred to as the *isolation sideband*. The main region that was used to define the SRs using the BDT output is referred to as the *main band*. The SRs are then regions in the *main band* with BDT output greater than zero. The events in the *isolation sideband* are used to predict the jetty-background in the *main band*. The *normalization region* is taken to be in the CR with $\text{BDT} < 0$, and can also be referred to as *BDT sideband* or more elaborately as *BDT normalization sideband*. Of course though, a *sideband* is still a kind of a CR.

Since the goal of this estimation method is to estimate the jetty-background, an isolation sideband is defined by requiring either one or two of the leptons to fail the jet-isolation criterion. That has also been defined in step 5 in Section 7.7.7. That means, that the lepton is distanced less than 0.6 in ΔR from a lepton-corrected jet. The jet that caused the lepton to fail the jet-isolation is required to have an original transverse momentum, i.e., transverse momentum before the subtractions, satisfying $15 < p_T < 30 \text{ GeV}$. The reason why the p_T is limited to this region is because 15 GeV is the upper bound on the leptons, and 30 GeV is the lower bound on the objects being summed in the calculation of H_T^{miss} and the number of jets in the event. If the upper bound of 30 GeV had not have been set, a bias in the isolation sideband would have been introduced, because requiring a lepton to fail jet-isolation, would also potentially mean requiring an extra jet with $p_T > 30 \text{ GeV}$, a requirement that didn't exist in the main band. The distributions of number of jets, as well as of H_T^{miss} , are blind to jet with $15 < p_T < 30 \text{ GeV}$, which makes it safe to potentially have extra jets in that region. The BDT training will be blind to those jets, and the BDT shape in the sideband should not be affected by those, thus achieving the goal of having consistent shapes between the main band and the sideband.

The main assumption that goes into using the isolation sideband is that in the background, the leptons are not isolated, but created in association with jets. Most will be produced inside jets, with a smoothly falling distribution outwards from a jet. By setting a cone of size 0.6 around jets and picking leptons inside those cones, events are picked up which have similar behavior to events where the leptons are outside of those cones. The rate of production of leptons inside jets will be much higher than those outside of the jets, but since their behavior

is similar kinematically, by fixing the normalization, their distributions will agree with the ones in the main band. The normalization factor is calculated by taking the ratio between the main band and the isolation sideband in the CR of $\text{BDT} < 0$. The event count in the sideband is multiplied by the normalization factor to comprise the prediction. The prediction in the SR then becomes:

$$N_{\text{predicted}}^{\text{SR}} = \frac{N_{\text{main band}}^{\text{CR}}}{N_{\text{sideband}}^{\text{CR}}} \cdot N_{\text{sideband}}^{\text{SR}}. \quad (7.10)$$

The assumption that the isolation sideband, i.e., events with at least one of the leptons failing the jet isolation criterion, correctly predicts the shape of the main band in the signal region, is tested by performing a shape comparison in simulation. Such shape comparison, or *closure test*, is performed by plotting the main band and the jet isolation sideband simultaneously, and checking that they statistically agree in terms of shape. A normalization factor is computed in order to correctly normalize the isolation sideband. In the current section, treatment of phase 1 (2017-2018), which in simulation is represented by 2017 MC is presented. Special care has been taken in the case of phase 0 (2016 data taking year) in Section 7.13.

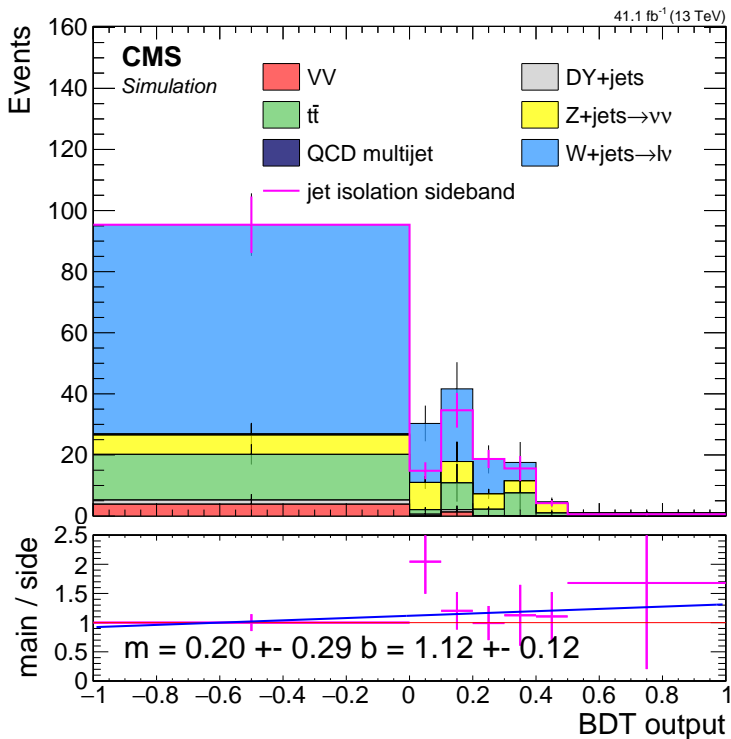


Figure 7.45: Dimuon 2017 jetty background closure plot. The stack represents simulation in the main isolation band after $Z/\gamma^* \rightarrow \tau^-\tau^+$ has been removed, while the pink line represents simulation in the isolation sideband. The isolation sideband is normalized to match the isolation in the CR of $\text{BDT} < 0$. The ratio panel shows the ratio between the isolation main band and sideband. A line fit of the ratio is performed and the parameters of the slope m and intercept point b with their respective errors are stamped.

The jetty background closure plot is shown in Figure 7.45. The closure plot tests the assumption that the background in the isolation main band can be predicted by the isolation sideband. Therefore, after proper normalization that is achieved by dividing the event count in the main band with the event count in the sideband, which in this case is 0.59, a flat ratio distribution is to be expected in the SRs. One can observe that indeed such a flat ratio distribution has been achieved by noting that most bins are statistically consistent with unity.

To check for any trend, a line fit has been performed for the ratio panel. Taking into account the errors, up to 1σ , the slope m is consistent with 0 and the interception b is consistent with 1, making the line consistent with a flat line intercepting 1. It is to be concluded therefore, that the closure plot confirms the shape assumption, and no trend that needs to be taken into account is to be seen. Full list of transfer factors with the associated uncertainties are found in Section 7.13.1, while special treatment of the 2016 case can be seen in Section 7.13.2.

7.10.2.2 Ditau Drell-Yann background estimation

It has been seen in Section 7.10.1.1 that the majority of the standard model background is composed of processes that produce leptons in association with jets, and therefore can be estimated with the jetty-background data-driven estimation method described in Section 7.10.2.1. However, as can be seen in Figure 7.41, a small amount of background arising from $Z/\gamma^* \rightarrow \tau^-\tau^+$ is also present, and since the leptons due to the leptonic decay $\tau \rightarrow \mu\bar{\nu}_\mu\nu_\tau$ are isolated, it requires an alternative background estimation method.

The $Z/\gamma^* \rightarrow \tau^-\tau^+$ background in this category is estimated using MC simulation. The event counts is being weighted according to a data correction normalization factor calculated in a dedicated CR. In order to do so, a CR rich and relatively pure in $Z/\gamma^* \rightarrow \tau^-\tau^+$ background must be found. In order to achieve this task, the observable $m_{\tau\tau}$ must be introduced. The background in question is due to a Drell-Yann process where a Z is decaying into two tau leptons, which in turn decay into muons via $\tau \rightarrow \mu\bar{\nu}_\mu\nu_\tau$. If the taus could be reconstructed, they could be used to calculate the invariant mass of the ditau event, $m_{\tau\tau}$, which is expected to peak at around the Z mass. The Z resonance could then be used as the desired CR rich in ditau background. However, leptonic taus are not directly reconstructed at CMS, which makes it necessary to find an alternative approach for calculating said invariant mass.

A widely used method for the reconstruction of the invariant mass $m_{\tau\tau}$ is the so-called *collinear approximation*. First described in [12], it has been used widely in ATLAS [13] and CMS [14]. In the collinear approximation, one assumes that the tau pair produced from Z/γ^* are highly energetic, so that their leptonic decays are collinear and the source of missing transverse momentum is due to the neutrinos only. If both the τ -leptons are sufficiently boosted, the neutrinos from each τ decay are collinear with the visible lepton momentum. One can then use the visible daughter-lepton momentum together with \vec{p}_T^{miss} to reconstruct the τ -lepton pair and calculate the would-be $m_{\tau\tau}$ invariant mass. Depending slightly on the mathematical details of the approximation, one can arrive at a strictly positive distribution for $m_{\tau\tau}$, as was done for example in [15], or one that also has negative values, as was done in [16, 17]. Since the negative values arising from the second variation of the approximation are due to events where \vec{p}_T^{miss} points away from one of the leptons, and therefore not arising from underlying boosted ditau events, it is useful to reject negative values in order to purify the CR by rejecting those events. The collinear approximation does not work when the taus are back-to-back. However, since in this analysis an ISR jet is required together with a high threshold of missing transverse momentum, it is expected to work well on the remaining boosted events. The signal, as well as other standard model processes are expected to have a flat distribution in $m_{\tau\tau}$, while events arising due to $Z/\gamma^* \rightarrow \tau^-\tau^+$ are expected to peak around the Z boson mass.

To put the assumptions into practice, an explicit definition of $m_{\tau\tau}$ is now laid out. The definition of the invariant mass is:

$$m_{\tau\tau}^2 = (p_{\tau_1} + p_{\tau_2})^2 \quad (7.11)$$

Assuming that the τ -pair is boosted, and the fully-leptonic decaying products is fully collinear to the τ -leptons, it follows that the transverse momentum of each neutrinos-pair is

proportional to the corresponding i τ_i 's transverse momentum by a scale-factor ξ_i by

$$\vec{p}_T^{\nu_i} = \xi_i \vec{p}_T^{\tau_i} \quad (7.12)$$

Since by assumption, all of the missing transverse momentum is due to the neutrinos, it follows that:

$$\vec{p}_T^{\text{miss}} = \xi_1 \vec{p}_T^{\tau_1} + \xi_2 \vec{p}_T^{\tau_2} \quad (7.13)$$

One solves the above two equations 7.13 for the two parameters ξ_1 and ξ_2 for each event. The solution becomes:

$$\begin{aligned} \xi_1 &= \frac{\vec{p}_{T_x}^{\text{miss}} \cdot \vec{p}_y^{\ell_2} - \vec{p}_{T_y}^{\text{miss}} \cdot \vec{p}_x^{\ell_2}}{\vec{p}_x^{\ell_1} \cdot \vec{p}_y^{\ell_2} - \vec{p}_x^{\ell_2} \cdot \vec{p}_y^{\ell_1}}, \\ \xi_2 &= \frac{\vec{p}_{T_y}^{\text{miss}} \cdot \vec{p}_x^{\ell_1} - \vec{p}_{T_x}^{\text{miss}} \cdot \vec{p}_y^{\ell_1}}{\vec{p}_x^{\ell_1} \cdot \vec{p}_y^{\ell_2} - \vec{p}_x^{\ell_2} \cdot \vec{p}_y^{\ell_1}}. \end{aligned} \quad (7.14)$$

Equation 7.11 is expended with the assumption that the τ 's are boosted and that the four-momenta of the taus is $p_{\tau_i} = (1 + \xi_i) p_{\ell_i}$:

$$\begin{aligned} m_{\tau\tau}^2 &= (p_{\tau_1} + p_{\tau_2})^2 \\ &= ((1 + \xi_1)p_{\ell_1} + (1 + \xi_2)p_{\ell_2})^2 \\ &= 2m_\tau^2 + 2(1 + \xi_1)(1 + \xi_2)p_{\ell_1} \cdot p_{\ell_2} \\ &\approx 2(1 + \xi_1)(1 + \xi_2)p_{\ell_1} \cdot p_{\ell_2}. \end{aligned} \quad (7.15)$$

This can be negative if $\xi_i < -1$. This can happen if the missing transverse momentum vector nearly opposite to a lepton's \vec{p}_T and also $p_T^{\text{miss}} > p_T^\ell$. This can easily happen in other background processes, such as WW+jets, when a neutrino and a lepton (possibly coming from different decay legs) are nearly back-to-back. Therefore, the final definition of $m_{\tau\tau}$ is

$$m_{\tau\tau} = \text{sign}(m_{\tau\tau}^2) \sqrt{|m_{\tau\tau}^2|}. \quad (7.16)$$

The CR to be used for the normalization should potentially have low signal contamination. It can be seen in Figure 7.40 that the region of $\text{BDT} < 0$ has hardly any signal contamination, and therefore is used for building the $\tau\tau$ CR. Figure 7.46 shows distributions of the $m_{\tau\tau}$ for the $\tau\tau$ simulation in red, and the rest of the standard model backgrounds in the stack. The two tracker phases are seen side by side. There is a clear peak in the $\tau\tau$ background at around the Z boson's mass. A window around the Z boson's mass is chosen of [40, 130] GeV in order to achieve high purity of 73% in both phases. The contamination in data is removed by first predicting the jetty background count using the data-driven method described in Section 7.10.2.1, and subtracting those counts from the data counts in the $\tau\tau$ dedicated CR. Then, a data divided by simulation normalization factor is computed in said $m_{\tau\tau}$ window to get 1.2 ± 0.46 (0.29 ± 0.26) which has relative error of 38% (90%) for phase 0 (phase 1).

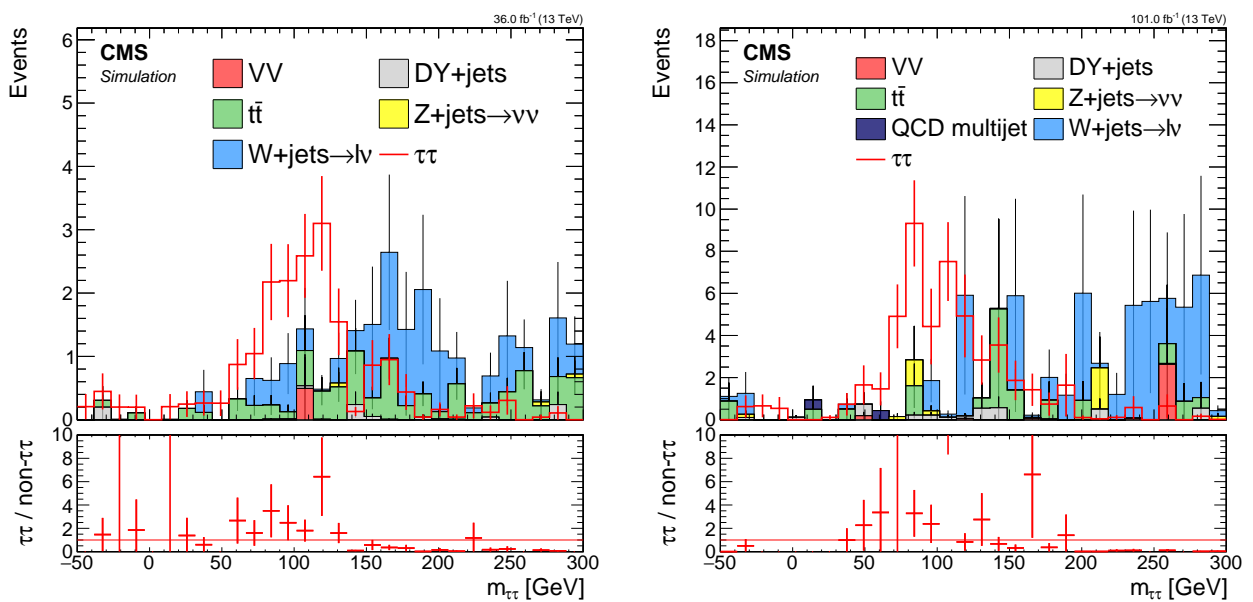


Figure 7.46: Dijet invariant mass $m_{\tau\tau}$ distributions for phase 0 2016 simulation (left) and phase 1 2017 simulation weighted to luminosity of 2017-2018 data taking period (right). The red line corresponds to $\tau\tau$ simulation, and the stack represents the rest of the standard model background simulation. No overflow bins are plotted in order to clearly show the resonance peak.

7.10.2.3 Exclusive track background estimation

The exclusive track category is consisted of four different BDTs, one for each lepton flavor and for each of those one for each phase. However, the background estimation method is the same for all of them, and it is a data-driven one.

The exclusive track category required one fully identified lepton according to the selection listed in Sections 7.7.1 and 7.7.2, and one track by a procedure described fully in Section 7.7.6. The track that is selected to be paired with the single identified lepton is selected as the track in the event with the highest BDT score among all tracks using a BDT that was trained on signal events in order to reject in-signal background and potentially pick up the track that corresponds to the non-identified second lepton in the signal event. In the background, the same selection procedure applies. However, unlike in the signal, it cannot be expected that the pairing of the selected track has a special relationship to the identified lepton other than passing some selections on the phase space. The chance of selecting a track in the background, that in combination with the identified lepton form an opposite-sign same-flavor pair that is a result of a resonance decay, is vanishingly small. It is highly likely that the track corresponds either to a lepton produced independently of the identified lepton in the event, or that it doesn't correspond to a lepton at all. Such a track is referred to as a *fake* track, and almost all tracks in the event are fakes.

To devise a successful data-driven background estimation for the exclusive track category we take advantage of the fact that the tracks in the background are independent of the identified lepton in the event. The selection process considered only tracks with opposite charge to the identified lepton, but if the track is independent of the lepton, events with a track of the same charge will be picked at the same rate as opposite charge ones. Not only is it expected to be selected at the same rate, but the shape of the BDT output will also be blind to this choice, making it an excellent proxy to the opposite charge background.

A CR is defined by selecting same-charge lepton-track pair rather than opposite-charge as in the SR. It is expected that the same charge CR is consistent also by the normalization to the SR since it is expected that these events are selected at the same rate of each other. Despite of this, the normalization is fixed by calculating a normalization factor as the ratio between the opposite-charge to same-charge event count in a dedicated normalization sideband CR satisfying $\text{BDT} < 0$, and applying it to the same-charge event count in the SRs satisfying $\text{BDT} > 0$. In order to test the independence assumption and to demonstrate the correct shape and normalization prediction, a closure test is performed in simulation. Figure 7.47 demonstrates closure tests for muons and electrons for both tracker phases. The stack represents standard model background for opposite-charge analysis selection lepton-track pair (oc), while the orange line represents same-charge lepton-track pair (sc). Both are weighted to represent each phase's luminosity. In the ratio panel, which shows the ratio between opposite-charge to same-charge backgrounds for each bin, a shape agreement is demonstrated which supports the assumptions made above.

After establishing that the method can be used to correctly predict the background, a data-driven normalization factor, which is computed as the ratio between opposite-charge to same-charge data event count in the CR of $\text{BDT} < 0$. The final prediction in the SRs then becomes the same-charge data event count in the SR multiplied by the normalization factor. The computed normalization factor for phase 0 (2016) is 1.12 ± 0.044 (1.037 ± 0.05) for muons (electrons), and for phase 1 (2017-2018) is 1.066 ± 0.024 (1.049 ± 0.03) for muons (electrons). The relative errors on the normalization factors are between 2% to 5%.

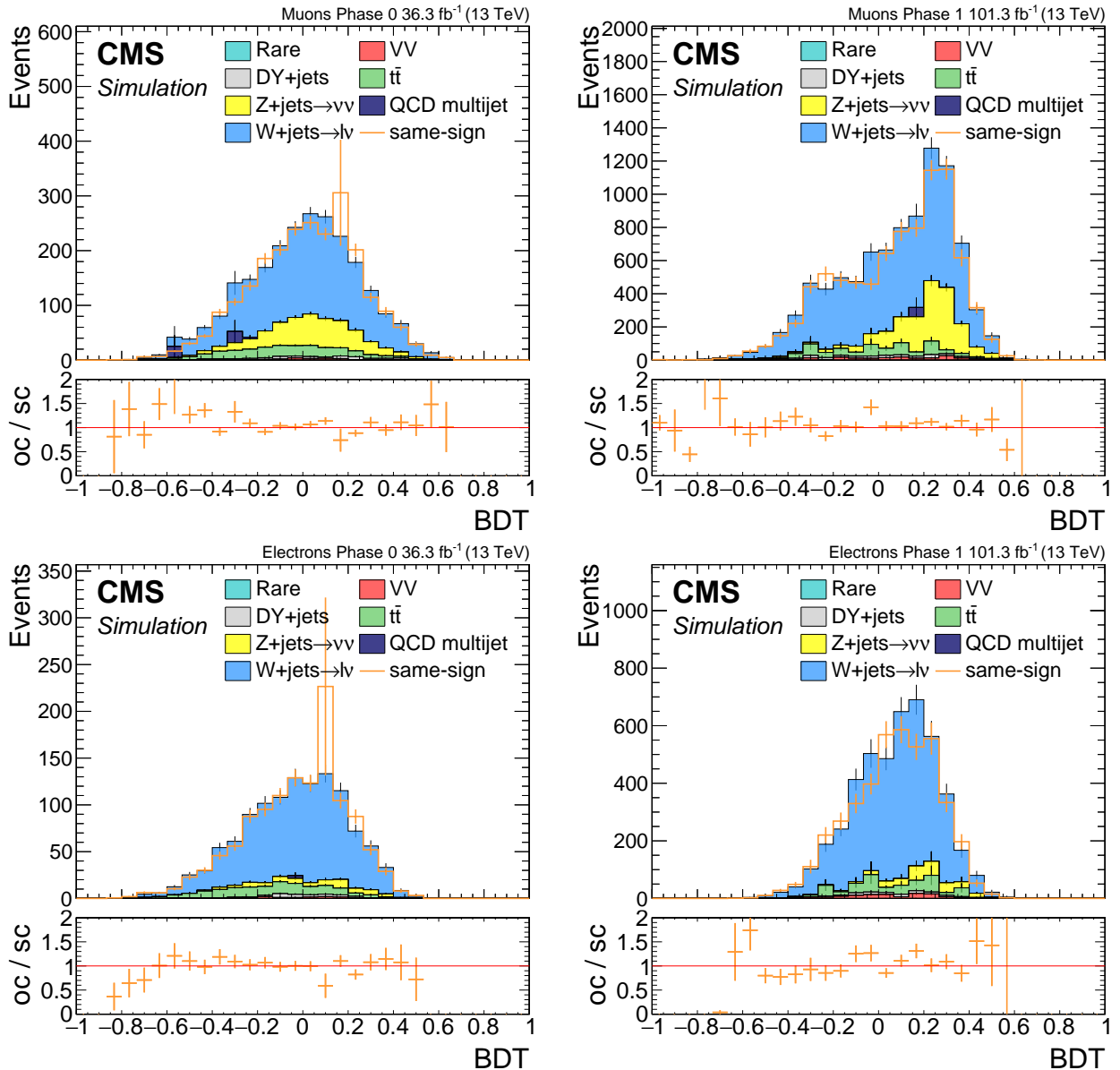


Figure 7.47: Exclusive track category closure tests for muons (top) and electrons (bottom) for phase 0 (left) and phase 1 (right). The stack represents standard model background for opposite-charge analysis selection lepton-track pair (oc), while the orange line represents same-charge lepton-track pair (sc). Both are weighted to represent each phase's luminosity. The ratio panel shows the ratio between opposite-charge to same-charge backgrounds for each bin.

7.11 Data control region plots

Monte Carlo simulation is being used in this analysis both in order to train the BDTs, and in order to gain understanding on the standard model processes composition of the background. It is useful therefore to look at data compared to simulation plots in order to verify that the simulation does not diverge from the data in a significant way. However, in order not to unblind the data in sensitive regions, the comparison plots are done in a CR. A straightforward CR is the same as the normalization region for the background estimation methods of $\text{BDT} < 0$. The most sensitive category is chosen for this study, namely, the dimuon category. The tracker phase 1 data taking period is shown in this section, since it is comprised of higher luminosity and is expected to suffer from some data taking quality issues which are further addressed in Section 7.14. The simulation has been normalized for phase 1 luminosity and the comparison plots can be seen in Figure 7.48. Good agreement between data and simulation can be observed in the ratio panel.

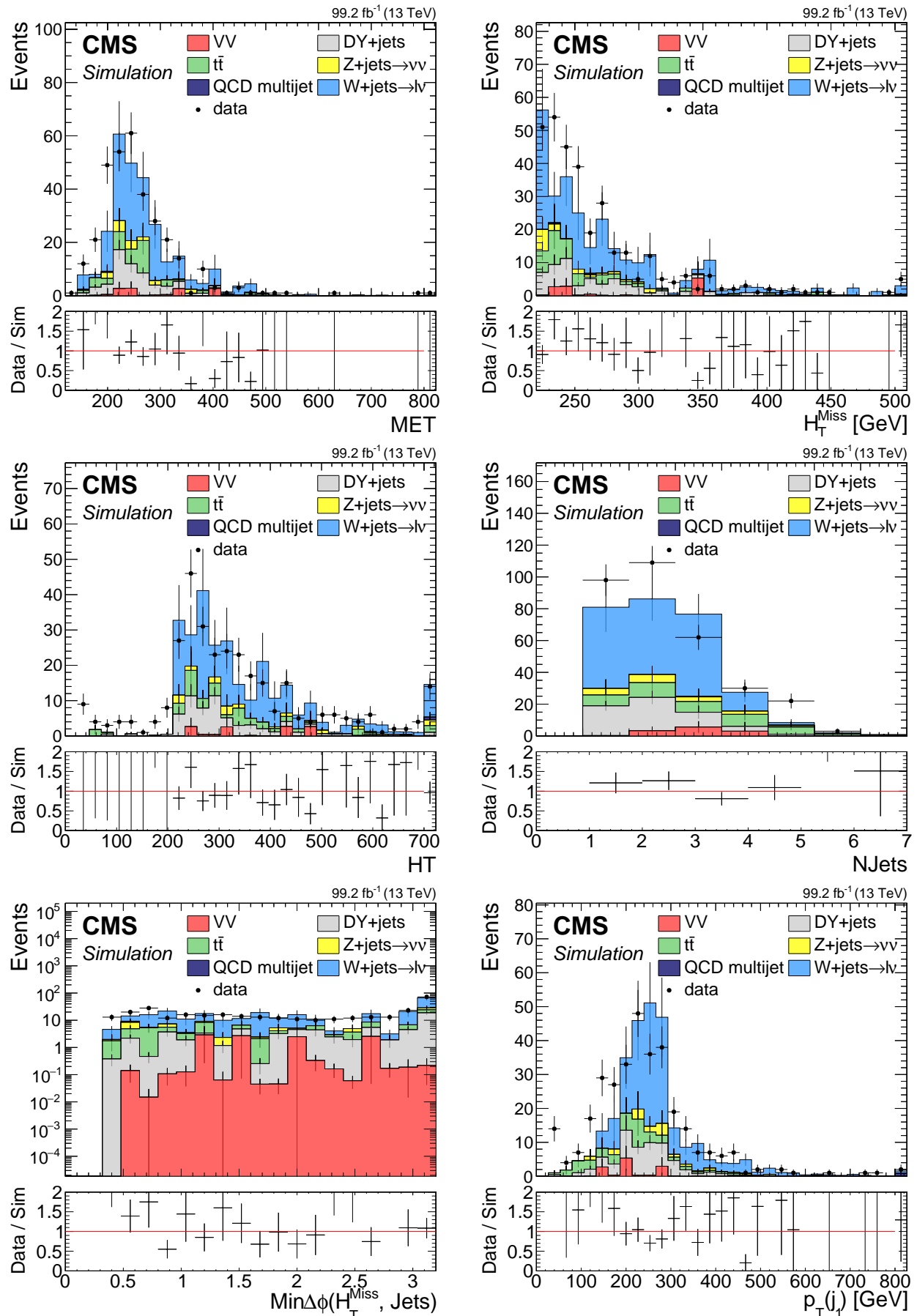
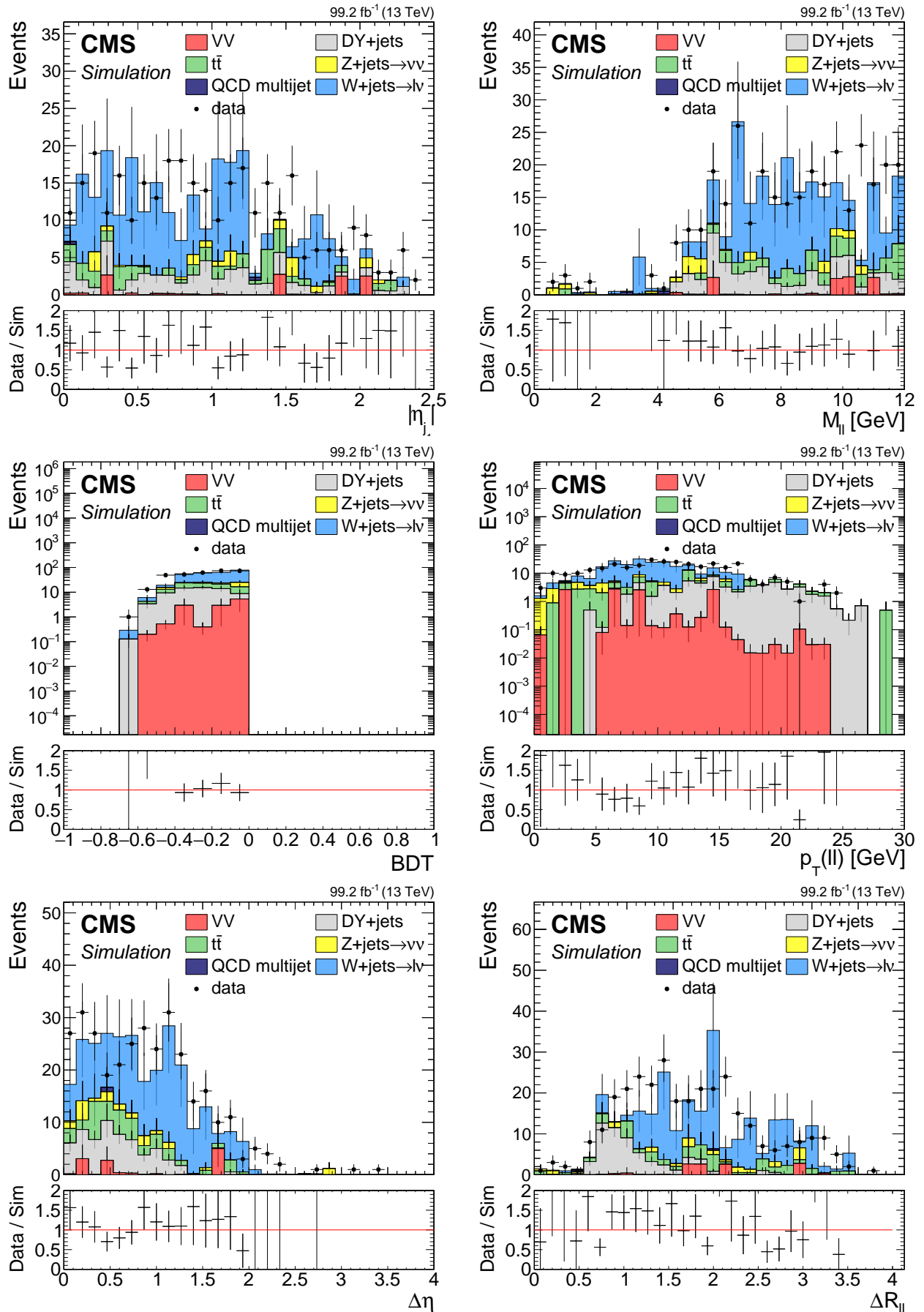


Figure 7.48: Data control region plots for dimuon category in phase 1.



7.12 Signal regions definition and optimization

The signal regions in this analysis are bins in the BDT output distributions having BDT output values greater than zero. This type of search is sometimes referred to as a *shape analysis*. The significance is computed in each bin of the BDT output, and then the different values are combined statistically to produce a single significance value. One must, therefore, decide on the binning of the BDT output distribution. Since the most important merit in a beyond the standard model search such as this one is the significance, it is desired to find a binning that maximizes the significance, or at least close to the supremum.

Because of the nature of how BDTs are trained, as the BDT value increases, so does the signal counts, whether the background counts decrease. This means that the most significant bin will be closer to the right end of the distribution. The problem of finding an ideal binning is not so straight forward as one might think, since the distributions are not smooth, but are made of statistical events with potentially very low statistics. The first step in defining the SRs is defining the right most deviation that becomes the left edge of the most sensitive bin stretching all way up to the maximum BDT output value of 1. The way it is performed is by first defining a step size ε . Then, a series of computations is performed, whereby in each step i , a significance is computed for a bin of size $i \cdot \varepsilon$, i.e., in the interval $[1 - i \cdot \varepsilon, 1]$. One can then pick the left bin by taking the maximum of the series of values resulting in the previous step.

There are few points that need to be addressed. The first is what measure to choose for estimating the significance. Since the final significance, combination, and exclusion limit is calculated using via the Higgs combination tool [18], here an estimate for the purposes of optimization is used which is reviewed in [19, 20], which is referred to as the Z-value. The Z-value is a communication of the p -value by means of specifying the corresponding number of standard deviations in a one-tailed test of a Gaussian (normal) variate:

$$Z = \Phi^{-1}(1 - p) = -\Phi^{-1}(p). \quad (7.17)$$

Given the number of signal events count \hat{s} , background events count \hat{b} and its corresponding error $\delta\hat{b}$, an estimator for the significance is given by

$$Z = \frac{\hat{s}}{\sqrt{\hat{b} + \hat{b}^2}}. \quad (7.18)$$

The background event count is estimated using the data-driven methods described in 7.10.2. They all involve counting events in a sideband and multiplying them by a transfer factor computed in a control region:

$$\hat{b} = N_{\text{sideband}}^{\text{SR}} \cdot \text{TF} \quad (7.19)$$

where the transfer factor TF is given by

$$\text{TF} = \frac{N_{\text{main band}}^{\text{CR}}}{N_{\text{sideband}}^{\text{CR}}} \quad (7.20)$$

The error propagation formula yields

$$\left(\frac{\delta\hat{b}}{\hat{b}} \right)^2 = \left(\frac{\delta N_{\text{sideband}}^{\text{SR}}}{N_{\text{sideband}}^{\text{SR}}} \right)^2 + \left(\frac{\delta \text{TF}}{\text{TF}} \right)^2, \quad (7.21)$$

which results in

$$\delta\hat{b}^2 = \hat{b}^2 \left[\left(\frac{\delta N_{\text{sideband}}^{\text{SR}}}{N_{\text{sideband}}^{\text{SR}}} \right)^2 + \left(\frac{\delta \text{TF}}{\text{TF}} \right)^2 \right]. \quad (7.22)$$

The second point that needs to be addressed is which signal point or points are chosen to be optimised. Since each model point has yields a different signal event count \hat{s} , they will also produce different significance values. The final values chosen maximize a range of signal points on the edge of the exclusion limit.

The third and last point to address is what step size ε to choose. If a step size too small is picked, as the BDT values are being scanned downwards from 1, there will be steps where no events are encountered either in the signal or the background due to the low statistics nature of the problem. Therefore, each signal event added will create a step upwards in the significance, while each background event will reduce it. This procedure will produce a very fine-tuned value which is not believed to be maximizing the significance, but rather it will produce wildly different results given a different set of events (from a different simulation set for example). To avoid overtraining, a step size of $\varepsilon = 0.5$ was chosen since its behavior is regular in the sense that every step adds both signal and background events, while also maintaining granularity.

Lastly, after the most significant bin has been fixed, the remaining BDT range from 0 to the left edge of the significant bin is divided equally in order to pick up any sensitivity that might remain in those bins. For the dimuon category, the bin width is chosen as 0.1, while for the exclusive track categories, it is 0.05. The final signal regions are as follows:

Table 7.11: Signal Regions

Category	Flavor	Phase	SR	Signal Regions
Dilepton	Muons	all	6	[0, 0.1, 0.2, 0.3, 0.4, 0.5, 1]
Exclusive Track	Muons	0	13	[0, 0.05, 0.1, 0.15, 0.2, ⋯, 0.5, 0.55, 0.6, 1]
Exclusive Track	Muons	1	12	[0, 0.05, 0.1, 0.15, 0.2, ⋯, 0.5, 0.55, 1]
Exclusive Track	Electrons	all	11	[0, 0.05, 0.1, 0.15, 0.2, ⋯, 0.5, 1]

7.13 Systematic uncertainties

In an experimental analysis, most or not all of the measured and predicted observables have uncertainties associated with them. Uncertainties can be experimental in nature, such as an uncertainty on the reconstruction efficiency of the muons in the detector, or theoretical, such as an uncertainty on a cross section. As a general rule, an uncertainty that scales with the number of events is referred to as statistical, while one that cannot be reduced by increasing the statistics is referred to as a systematic uncertainty. It could well be that a statistical uncertainty in one study, becomes a systematic in another.

As mentioned, there are uncertainties associated with theoretical calculations, with simulation mismodeling (both for FASTSIM and FULLSIM), and the list is long. This analysis follows all the recommendations that are listed by the CMS SUSY Physics Analysis Group (PAG) [21]. The list includes for example the muon scale factors that have been studied in Section 7.7.3. In this section, only the systematic uncertainties that are unique to this analysis are introduced, apart from the muon scale factors that have been described in detail in Section 7.7.3. The systematic uncertainties in this analysis are due to the background estimation methods used.

7.13.1 Data driven transfer factors

Data driven background estimations are used both in the dimuon category to estimate the jetty non-isolated background, as well as for the exclusive track background. They involve computing a transfer factor in a dedicated CR of $BDT < 0$ and applying it in the SRs. The transfer factors are computed as the ratio between the data counts in the main band and the sideband. In the dimuon category the sideband is the isolation sideband as has been described in Section 7.10.2.1 and for the exclusive track category, the sideband is the same-charge sideband as has been described in Section 7.10.2.3. These transfer factors have an uncertainty associated with them due to the statistics in the CR. Table 7.13.1 lists all transfer factors and their associated uncertainties.

Table 7.12: Transfer factors and their associated uncertainties

Method	Flavor	Phase	Transfer Factor	Uncertainty	Relative Error
Jetty	Muons	0	0.548	0.078	14.2%
Jetty	Muons	1	0.533	0.039	7.3%
$\tau\tau$	Muons	0	0.518	0.411	79%
$\tau\tau$	Muons	1	0.283	0.26	91.8%
Exclusive Track	Muons	0	1.12	0.044	3.9%
Exclusive Track	Muons	1	1.066	0.024	2.2%
Exclusive Track	Electrons	0	1.037	0.05	4.8%
Exclusive Track	Electrons	1	1.049	0.03	2.8%

7.13.2 Data driven shape uncertainties

In the section about the background estimation methods, it is explained that the data driven methods rely on an assumption that the shape of the background in a sideband is the same as in the main band, and therefore require only a normalization factor in order to correctly predict background. The exclusive track category closure plots in Figure 7.47 show no trend, and neither does the phase 1 closure plot of the jetty background in Figure 7.45. This is also supported by the line fit that was performed in the ratio panel, which is statistically consistent with a flat line intersecting 1.

In the dimuon category, only one BDT is trained using 2017 simulation, but evaluated for phase 0 (2016) as well. That introduces a slight trend when a line is fit in the ratio panel of the closure plot in Figure 7.49. The line fit is then used to introduce weights which are applied in an event-by-event manner which have the value of the line for the specific BDT value of the event. One the right side of Figure 7.49, one can see the closure plot after said weights have been applied, and be convinced that it has successfully eliminated the trend.

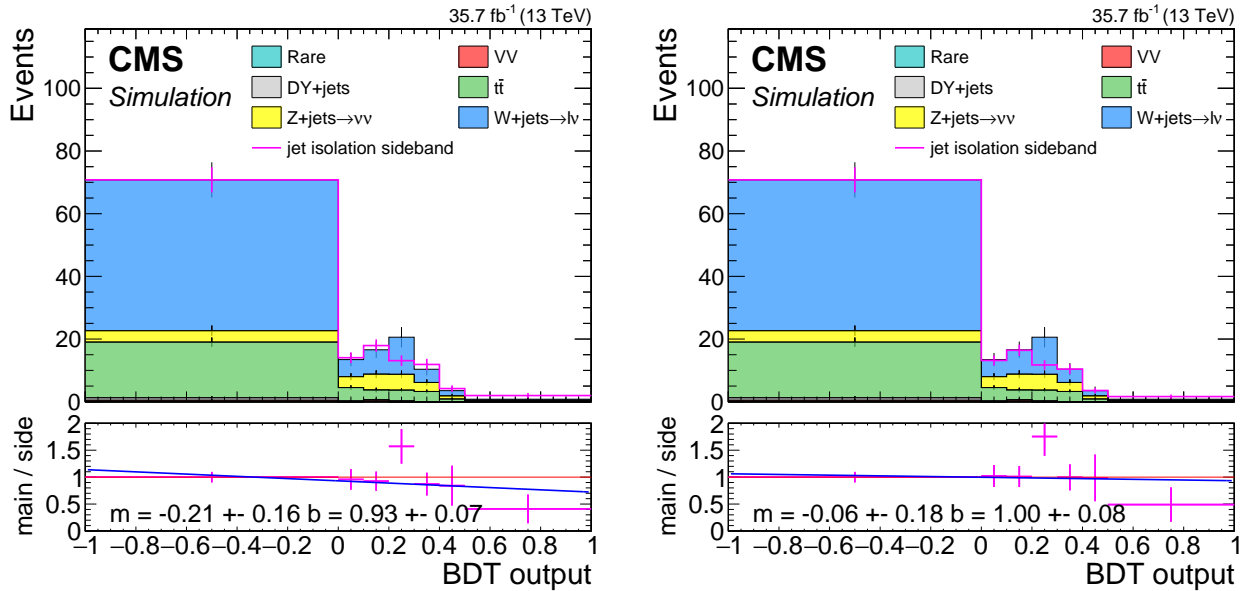


Figure 7.49: Dimuon 2016 jetty background closure plot with (right) and without (left) fit line weights. The stack represents simulation in the main isolation band after $Z/\gamma^* \rightarrow \tau^-\tau^+$ has been removed, while the pink line represents simulation in the isolation sideband. The isolation sideband is normalized to match the isolation in the CR of $\text{BDT} < 0$. The ratio panel shows the ratio between the isolatoin main band and sideband. A line fit of the ratio is performed and the parameters of the slope m and interception point b with their respective errors are stamped. In the plot on the right, the line fit weights obtained from the fit on the left plot have been applied.

On top of the transfer factor uncertainties listen in Table 7.13.1, shape uncertainties taken from the lines fits are also taken into account. For phase 1, since the closure plot line fit did not show any trend, the nominal values are taken without applying the line weights. For 2016, the nominal values are taken after the line weights were applied, i.e., from the right plot in Figure 7.49. The alternative prediction which is fed into the combine tool as the shape systematic uncertainty, is for 2017 the histogram with the line weights applied, and for 2016, since the weights were already applied as the nominal value, the weights of the fit line with the slop varied by 1σ is applied ($m = -0.21 - 0.16 = -0.37$).

7.13.3 Simulated background uncertainties

The last background estimation method to consider is the $\tau\tau$ background estimation, which uses simulation normalized to data in a CR, as explained in Section 7.10.2.2. For background methods that use simulation rather than data, normally a list of uncertainties associated with simulation uncertainties have to be applied. However, as could be seen in Figure 7.50, this background is non-existent in the most sensitive bin, and is very small in the rest of the bins. Therefore, the already very large uncertainties on this background (79%-92%) is dominant enough so that all other uncertainties can be safely neglected.

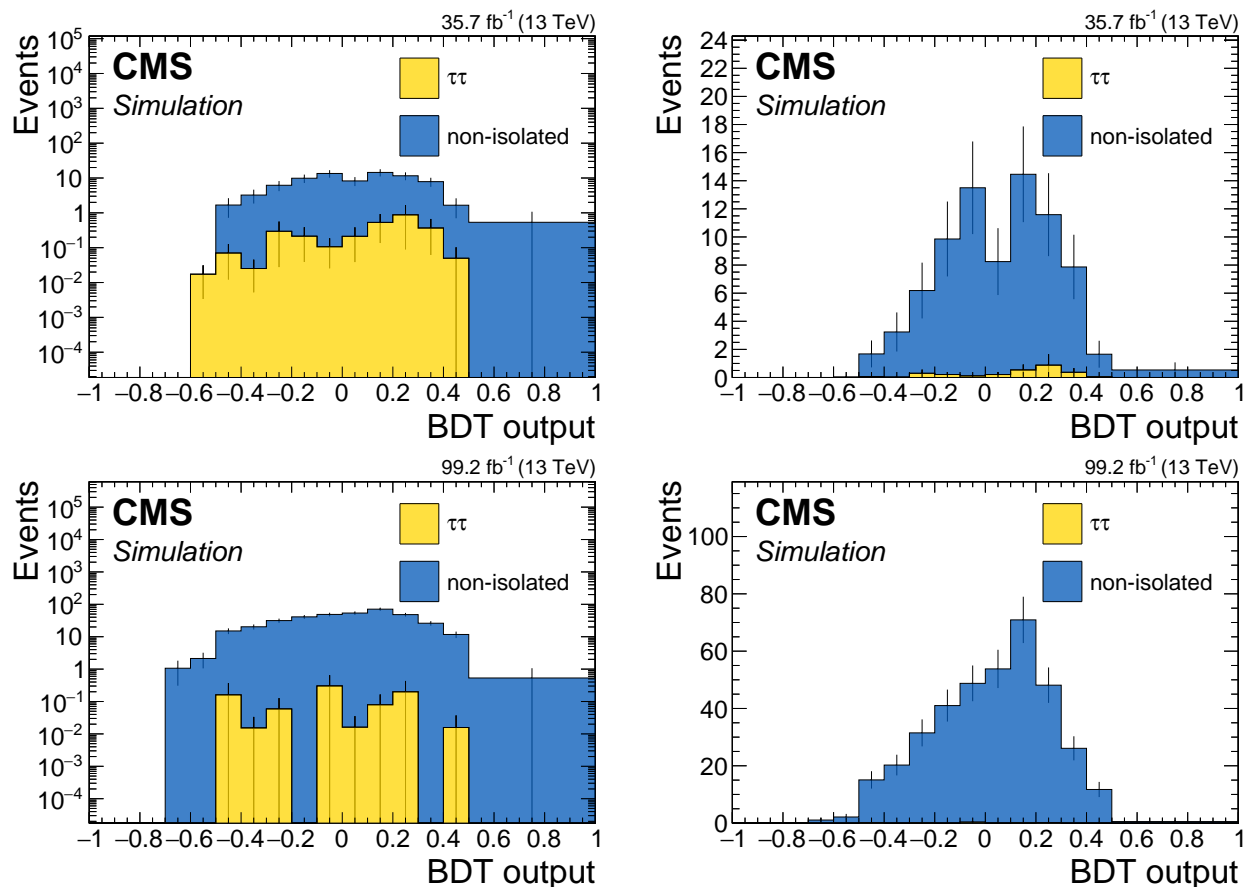


Figure 7.50: Dimuon full background prediction for phase 0 (top) and phase 1 (bottom) both in log scale (left) and linear scale (right). Blue represents the data-driven jetty non-isolated background, while yellow is the $\tau\tau$ background.

7.14 Data quality aspects and background validation

During the run 2 data taking period of CMS, there have been a few detector issues that require some special care. Following the central recommendations, three issues are handled here, namely, L1 prefire rate in 2016 and 2017, ECAL Endcap (EE) noise in 2017, and the HE minus side (HEM) failure in 2018. In the process of dealing with these issues, the jetty background data-driven method is also validated in data.

7.14.1 L1 prefire issue in 2016 and 2017 data

The L1 prefire issue in the 2016 and 2017 happened due to an ECAL timing error which is propagated to the L1 trigger primitives. This issue occurred because the trigger system used data from the previous bunch crossing, rather than the current one, to determine whether an event should be triggered. Events with significant ECAL energy in the region $2.5 < |\eta| < 3$ are effected in 2016 and 2017 data. This can lead to inefficiency and is studied for signal Monte Carlo samples, as it can potentially lower the signal event count. Prefiring weights were added to signal and checked against the unweighted events, and no significant effect is observed. Data is also checked with and without the prefiring weights for the most effected period of 2017 by looking at closure plots in a same-charge CR. This serves both as validating that the prefire issue does not effect this analysis, and acts as a data validation for the jetty background. Plots can be seen in Section 7.14.4.

7.14.2 EE noise in 2017 data

In 2017 data, an observed excess of the fake p_T^{miss} compared to simulation caused by increased noise in low p_T jets. Additional noise in the ECAL endcaps in data could be identified as cause of this effect. In order to deal with this issue, the recommendation is to recalculate p_T^{miss} excluding jets in the affected phase space. This is done centrally in the process of creating the samples used in this analysis.

7.14.3 HEM failure in 2018 data

Following the power interruptions generated by false fire alarms on Saturday June 30th, negative endcap Hadron Calorimeter (HCAL) sectors HEM15 and HEM16 could no longer be operated until the end of 2018 run. The effected $\eta - \phi$ region is $-3.0 < \eta < -1.3$ and $-1.57 < \phi < -0.87$. The first regular physics run affected is 319077. Data and simulation vetoes for objects in the affected region are applied. Same-sign validation plots are made pre-HEM and post-HEM in order to see their effects. The well behaved validation plots suggest that this analysis is not badly effected by this issue.

7.14.4 Same sign validation plots

Figure 7.51 shows data validation plot for same-charge control region. They serve both as background method validation, and to check the data taking issues mentioned above. The plots are divided to different data taking periods in order to check the effects of the the data taking issues. The same sign control region has been selected, since it can validate the assumption that the isolation sideband properly predict the shape of the main band and can therefore be used as the estimation method. Overall, good shape agreement is demonstrated between the main band and the isolation sideband.

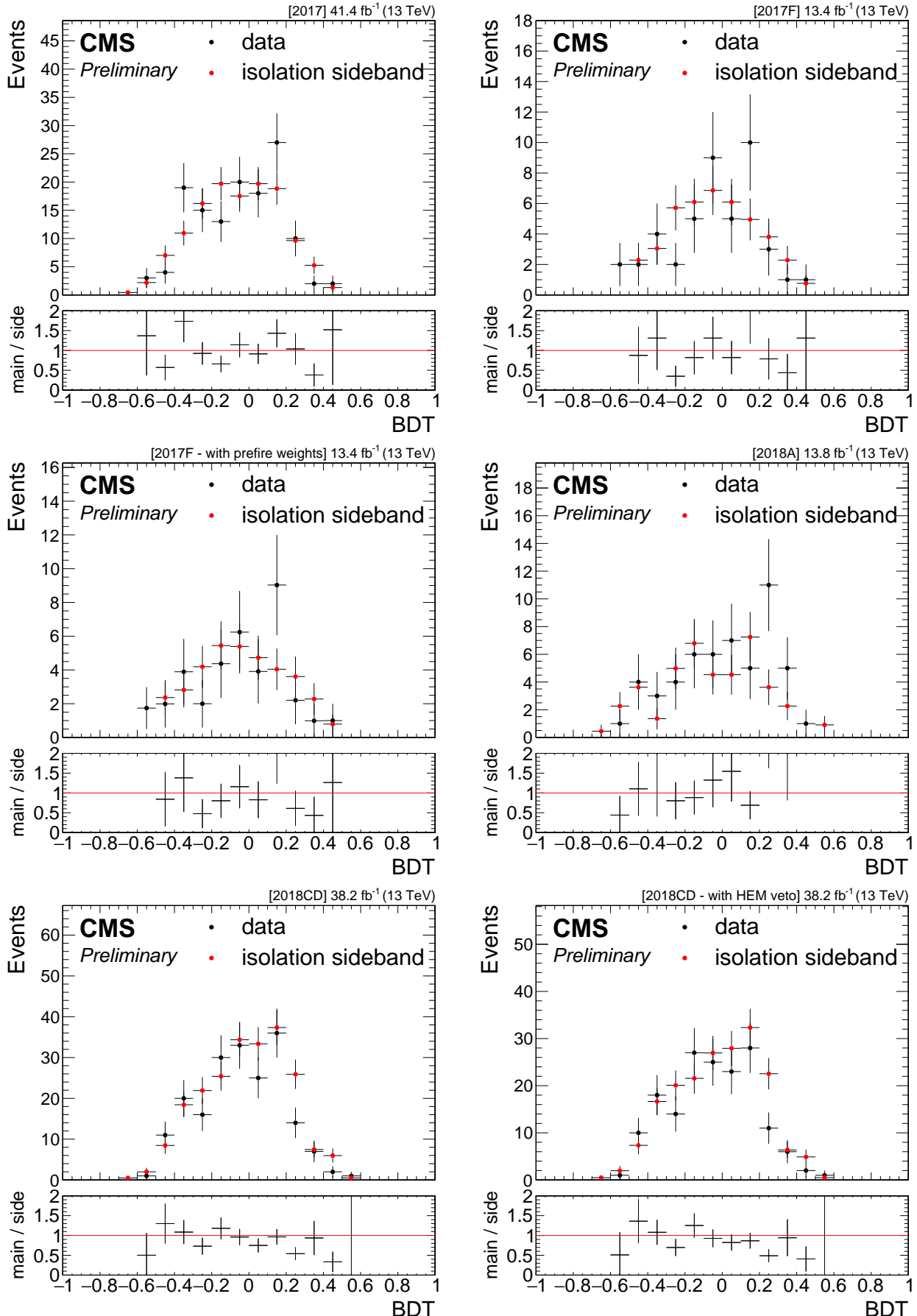


Figure 7.51: Data same sign control validation plots. Black dots show same sign data in the main band, while red dots show same sign data in the isolation side band, normalized in the $\text{BDT} < 0$ region. Ratio panel shows the ratio between them. Going line by line from left to right, the corresponding plots are shown: 2017 data taking period, 2017F data taking period, 2017F data taking period with prefire weights, 2018A data taking period (pre HEM), 2018CD data taking period (post HEM), 2018CD data taking period with HEM veto (post HEM).

7.15 Results and interpretation

Chapter 8

Summary

Chapter 9

Latex stuff

9.1 Some examples

9.1.1 Multiline comment

This is a line in introduction.

9.1.2 Fixme note

This is the introduction to the thesis. **FiXme Note:** This is a fixme note **FiXme Note:** what **FiXme Note:** WHAT THE HELL AFTER

9.1.3 Tables

h - here t - top b - bottom p - special page ! - even if not pretty

Table 9.1: Table captions are above the table whereas figure captions are below.

Parameter	Value 1	Value 2
s	10.0	20.0
t	20.0	30.0
u	30.0	40.0

9.1.4 Cross References

9.1.4 87 section 9.1.4

9.1.5 Particles

Hello World $\tilde{\chi}_1^0 \pi \eta_c$ GeV E_T^{miss} hey GeV E_T^{miss} π new one $\tilde{\chi}_1^0 \tilde{\chi}_1^0$

9.1.6 Citing

[1] SOS analysis

9.1.7 Glossary

Using glossary for computer plural form computers upper case first Computer upper case first plural Computers. To use for symbol π

9.1.8 Acronyms

First use of acronym SOS and second SOS. You can reset this and do again Soft-Opposite-Sign (SOS) and second time again SOS. Long version Soft-Opposite-Sign. Full version Soft-Opposite-Sign (SOS). Short version SOS.

9.1.9 fractions

Here's a fraction with a slash:

$$\text{Track Isolation}_\ell = \sum_{\substack{\text{tracks from PV} \\ \text{in } \Delta R < 0.3}} p_T / p_T(\ell) \quad (9.1)$$

List of Corrections

Note: fill in signal model stuff	13
Note: make sure we define the different deltaM somewhere	13
Note: Add jetty/tautau simulation plot	62
Note: This is a fixme note	87
Note: what	87
Note: WHAT THE HELL	87

Glossary

computer is a programmable machine that receives input, stores and manipulates data, and provides output in a useful format. 85

Δm mass difference between electroweakinos. If not explicitly said otherwise, it is the mass difference between $\tilde{\chi}_2^0$ and $\tilde{\chi}_1^0$, i.e., $\Delta m = \Delta m^0 = m_{\tilde{\chi}_2^0} - m_{\tilde{\chi}_1^0}$. 27, 31

Δm^0 mass difference between the neutral electroweakinos $\tilde{\chi}_2^0$ and $\tilde{\chi}_1^0$, i.e., $\Delta m^0 = m_{\tilde{\chi}_2^0} - m_{\tilde{\chi}_1^0}$. 26

ΔR separation. 19, 23, 24

η pseudorapidity. 23

E_T^{miss} add description. 15, 16

H_T^{miss} add description. 15, 16, 50

$m_{\ell\ell}$ invariant mass. 19–21

neutralino add description. 15, 16

ϕ azimuthal angle measured in radians. 23

π ratio of circumference of circle to its diameter. 85

p_T transverse momentum. 15, 18, 19, 23, 27, 31

Acronyms

ATLAS A Toroidal LHC Apparatus. 68

BDT Boosted Decision Tree. 31, 41, 43, 51–53, 55, 58–60, 62, 66, 71, 73, 76, 79

CERN European Organization for Nuclear Research. 9

CMS Compact Muon Solenoid. 9, 45, 68, 78, 81

CR Control Region. 65–69, 71, 73, 78, 79, 81

CSV Combined Secondary Vertex. 40

DM Dark Matter. 15

ECAL Electromagnetic Calorimeter. 27, 81

ISR Initial State Radiation. 15, 16, 26, 27, 50, 51, 68

LHC Large Hadron Collider. 9

LSP Lightest SUSY Particle. 15

MC Monte Carlo. 35, 36, 46, 52, 59, 65, 67, 68

PAG Physics Analysis Group. 78

PF Particle Flow. 40

POG Physics Object Group. 35, 36

PU Pile-Up. 40, 45

QCD Quantum Chromodynamics. 15, 16, 50, 59

SF Scale Factor. 35

SM Standard Model. 15, 16, 23, 24, 33, 50–52, 58, 65

SOS Soft-Opposite-Sign. 21–24, 51, 86

SR Signal Region. 52, 58–60, 65–67, 71, 76, 78

SUSY Supersymmetry. 15, 78

WIMP Weakly Interacting Massive Particle. 15

Bibliography

- [1] CMS Collaboration, A. Tumasyan *et al.*, “Search for supersymmetry in final states with two or three soft leptons and missing transverse momentum in proton-proton collisions at $\sqrt{s} = 13$ TeV,” *JHEP* **04** (2022) 091, arXiv:2111.06296 [hep-ex].
- [2] https://gitlab.cern.ch/cms-muonPOG/MuonReferenceEfficiencies/-/tree/master/EfficienciesStudies/2016_legacy_rereco/Jpsi.
- [3] <https://indico.cern.ch/event/791428/contributions/3287172/attachments/1781977/2899551/2016LegacyReReco2.pdf>.
- [4] BRIL Group, “Bril work suite.”
<http://cms-service-lumi.web.cern.ch/cms-service-lumi/brilwsdoc.html>, 2017.
- [5] https://lguzzi.web.cern.ch/lguzzi/Tau3Mu/muonPOG_mediumID_dR.pdf.
- [6] T. C. collaboration, “Performance of the CMS missing transverse momentum reconstruction in pp data at $\sqrt{s} = 8$ tev,” *Journal of Instrumentation* **10** no. 02, (Feb, 2015) P02006–P02006. <https://doi.org/10.1088%2F1748-0221%2F10%2F02%2Fp02006>.
- [7] M. Cacciari, G. P. Salam, and G. Soyez, “The anti-kt jet clustering algorithm,” *Journal of High Energy Physics* **2008** no. 04, (Apr, 2008) 063–063.
<https://doi.org/10.1088%2F1126-6708%2F2008%2F04%2F063>.
- [8] A. Hoecker, P. Speckmayer, J. Stelzer, J. Therhaag, E. von Toerne, H. Voss, M. Backes, T. Carli, O. Cohen, A. Christov, D. Dannheim, K. Danielowski, S. Henrot-Versille, M. Jachowski, K. Kraszewski, A. Krasznahorkay, M. Kruk, Y. Mahalalel, R. Ospanov, X. Prudent, A. Robert, D. Schouten, F. Tegenfeldt, A. Voigt, K. Voss, M. Wolter, and A. Zemla, “Tmva - toolkit for multivariate data analysis,” 2007.
<https://arxiv.org/abs/physics/0703039>.
- [9] <https://twiki.cern.ch/twiki/bin/view/CMS/SWGuideMuonIdRun2>.
- [10] S. Chatrchyan, , V. Khachatryan, and A. M. et. al, “Search for new physics with same-sign isolated dilepton events with jets and missing transverse energy at the LHC,” *Journal of High Energy Physics* **2011** no. 6, (Jun, 2011) .
<https://doi.org/10.1007%2Fjhep06%282011%29077>.
- [11] K. Rehermann and B. Tweedie, “Efficient identification of boosted semileptonic top quarks at the LHC,” *Journal of High Energy Physics* **2011** no. 3, (Mar, 2011) .
<https://doi.org/10.1007%2Fjhep03%282011%29059>.
- [12] R. Ellis, I. Hinchliffe, M. Soldate, and J. Van Der Bij, “Higgs decay to $\tau^+ \tau^-$ -a possible signature of intermediate mass higgs bosons at high energy hadron colliders,” *Nuclear Physics B* **297** no. 2, (1988) 221–243.
<https://www.sciencedirect.com/science/article/pii/0550321388900193>.

- [13] **ATLAS** Collaboration, G. Aad *et al.*, “Expected Performance of the ATLAS Experiment - Detector, Trigger and Physics,” arXiv:0901.0512 [hep-ex].
- [14] **CMS** Collaboration, G. L. Bayatian *et al.*, “CMS technical design report, volume II: Physics performance,” *J. Phys. G* **34** no. 6, (2007) 995–1579.
- [15] Z. Han, G. D. Kribs, A. Martin, and A. Menon, “Hunting quasidegenerate higgsinos,” *Physical Review D* **89** no. 7, (Apr, 2014) .
<https://doi.org/10.1103%2Fphysrevd.89.075007>.
- [16] H. Baer, A. Mustafayev, and X. Tata, “Monojet plus soft dilepton signal from light higgsino pair production at LHC14,” *Physical Review D* **90** no. 11, (Dec, 2014) .
<https://doi.org/10.1103%2Fphysrevd.90.115007>.
- [17] A. Barr and J. Scoville, “A boost for the EW SUSY hunt: monojet-like search for compressed sleptons at LHC14 with 100 fb-1,” *Journal of High Energy Physics* **2015** no. 4, (Apr, 2015) . <https://doi.org/10.1007%2Fjhep04%282015%29147>.
- [18] <https://cms-analysis.github.io/HiggsAnalysis-CombinedLimit/>.
- [19] L. Demortier, “P values and nuisance parameters,” in *Statistical issues for LHC physics. Proceedings, Workshop, PHYSTAT-LHC, Geneva, Switzerland, June 27-29, 2007*, p. 23. 2008. <http://cds.cern.ch/record/1099967/files/p23.pdf>.
- [20] R. D. Cousins, J. T. Linnemann, and J. Tucker, “Evaluation of three methods for calculating statistical significance when incorporating a systematic uncertainty into a test of the background-only hypothesis for a Poisson process,” *Nucl. Instrum. Meth. A* **595** (2008) 480, arXiv:physics/0702156 [physics.data-an].
- [21] <https://twiki.cern.ch/twiki/bin/view/CMS/SUSRecommendationsRun2LegacyTable>.

List of Figures

7.1	Signal Models Feynman Diagrams	13
7.2	Signal E_T^{miss} and H_T^{miss} distributions	16
7.3	Signal number of jets and leading jet p_T distributions	17
7.4	Signal number of b -tagged jets distributions	17
7.5	Signal $\min \Delta\phi(E_T^{\text{miss}}, \text{jets})$ and $\min \Delta\phi(H_T^{\text{miss}}, \text{jets})$ distributions	18
7.6	Signal p_T distributions	19
7.7	Signal p_T distributions split into barrel and endcaps	20
7.8	Signal $ \eta $ distributions	21
7.9	Signal generator level $m_{\ell\ell}$ distributions	22
7.10	Signal $m_{\mu\mu}$ vs. p_T	23
7.11	Signal reconstructed $m_{\mu\mu}$	24
7.12	Signal generator level ΔR distributions	24
7.13	Signal $\Delta R(\mu\mu)$ vs. p_T	25
7.14	Signal reconstructed $\Delta R(\mu\mu)$	25
7.15	Spatial separation between reconstructed electrons and the leading jet $\Delta R(j_1, e)$	28
7.16	p_T distribution of reconstructed electrons with loose ID	29
7.17	$ \eta $ distribution of reconstructed electrons with loose ID	29
7.18	medium and tight ID working points distribution of reconstructed electrons	30
7.19	standard isolation and jet-isolation distribution of reconstructed electrons	31
7.20	$ \eta $ distribution of reconstructed electrons with loose ID passing jet-isolation	32
7.21	Spatial separation between reconstructed muons and the leading jet $\Delta R(j_1, \mu)$	33
7.22	Reconstructed muons p_T	34
7.23	$ \eta $ distribution of reconstructed muons with loose ID before and after $p_T > 2 \text{ GeV}$ cut	34
7.24	medium ID working point distribution of reconstructed muons	35
7.25	tight ID working point distribution of reconstructed muons	35
7.26	jet-isolation distribution of reconstructed muons	36
7.27	Simluation barrel muons fits	39
7.28	Simluation endcaps muons fits	39
7.29	Data barrel muons fits	40
7.30	Data endcaps muons fits	40
7.31	Efficiencies and scale factors	41
7.32	Muon track BDT training inputs	44
7.33	Track BDT output plots	45
7.34	Track BDT ROC curves	46
7.35	Dimuon BDT output and ROC curve	55
7.36	dimuon training input distribution	56
7.37	Exclusive track category BDT outputs	57
7.38	Exclusive track category ROC curve	58
7.39	exclusive track training input distribution	59

7.40 Dimuon simulation BDT output	62
7.41 Dimuon simulation BDT output jetty tautau	62
7.42 Dimuon simulation BDT inputs	63
7.43 Exclusive track plus muon 2017 simulation BDT output	64
7.44 Exclusive track plus muon simulation BDT inputs	65
7.45 Dimuon 2017 jetty background closure plot	68
7.46 Ditau invariant mass distibutions	71
7.47 Exclusive track category closure tests	73
7.48 Data control region plots for dimuon category in phase 1	75
7.49 Dimuon 2016 jetty background closure plots with and without fit line weights . .	80
7.50 Dimuon full background prediction for both phases	81
7.51 Data same sign control validation plots	83

List of Tables

7.1	Base selection applied to all analysis categories	17
7.2	Generator level efficiency on muons selections	23
7.3	Selection criteria for Tags and Probes	38
7.4	Track BDT input variables	44
7.5	Signal Efficiency	48
7.6	Background Efficiency	49
7.7	Transfer Factor	49
7.8	Significance $s/\sqrt{b + \epsilon_b^2}$	50
7.9	Dimuon BDT input variables	55
7.10	Exclusive track BDT input variables	58
7.11	Signal Regions	78
7.12	Transfer factors and their associated uncertainties	79
9.1	Table captions are above the table whereas figure captions are below.	87